UNIVERSITY OF CALIFORNIA,

IRVINE

Grain boundary structure and interfacial complexions for the creation of tough, stable nanostructured metals

DISSERTATION

Submitted in Partial Satisfaction of the Requirements

for the Degree of

DOCTOR OF PHILOSOPHY

in Materials Science and Engineering

by

Amirhossein Khalajhedayati

Dissertation Committee:

Professor Timothy J. Rupert, Chair

Professor James Earthman

Professor Daniel Mumm

2015

Dedication

I dedicate my thesis to my parents who have supported me throughout my education and to whom I owe all my success.

I also dedicate this thesis to my beautiful and lovely wife, Raha. Words cannot describe how grateful I am to have her in my life, and because of her, I had the best PhD experience any person could wish for.

Table of Contents

List of Figures

Acknowledgments

First and foremost, I would like to express my most sincere gratitude to my advisor Prof. Timothy J. Rupert for his continuous support throughout my PhD studies. Before I joined Tim's research group, I could have only dreamt about being the scholar I am today. His enthusiasm and dedication to science have always motivated my research work. I cannot thank Tim enough for all the guidance and advice over the past four years and certainly could not have imagined a better mentor for my PhD program.

Additionally, I would like to thank the members of my thesis committee, Prof. James Earthman, and Prof. Daniel Mumm for their insightful comments and encouragement.

I would also like to thank the director of Lexi at UC Irvine, Dr. Jian-Guo Zheng who provided me an opportunity to join his team.

Lastly, I would like to thank my fellow colleagues in Rupert Group, Jason Panzarino, David Bober, Simon Pun, Zhiliang Pan, and Joseph Ludy. Above all the scientific discussions and collaborations, they have created a fun and friendly environment to work and conduct research.

Curriculum Vitae

Amirhossein Khalajhedayati

6322 Adobe Cir • Irvine, CA 92617 • akhalajh@uci.edu • (925) 457-3299

Education

PhD Candidate in Materials Science and Engineering, GPA 4.0 Jun 2015
University of California, Irvine *Irvine, CA*
Thesis: The effect of grain boundary structure on failure of nanostructured materials

M.S. in Materials Engineering, GPA 3.71 Aug 2010
San Jose State University *San Jose, CA*
Thesis: Aluminum Induced Crystallization of amorphous silicon for solar cell fabrication

B.S. in Materials Science Engineering, Top 1% in the country Sep 2007
Sharif University of Technology *Tehran, Iran*
Simulation of chemical vapor deposition (CVD) of titanium dioxide nanoparticles from metalorganics

Research Experience

PhD Researcher Aug 2010 - Jun 2015
University of California, Irvine Irvine, CA

- Developed novel nanostructured materials with superior strength and ductility using electrodeposition and high energy alloying
- Analyzed failure and fracture of various material systems including nanostructured materials through in-situ and ex-situ micro-mechanical testing
- Mastered processing techniques and sample preparation methods such as Focused Ion Beam (FIB), Wet Chemistry, Heat Treatment, and Ultra-high Vacuum Thin Film Deposition
- Acquired extensive experience performing advanced characterization methods using High Resolution Transmission Electron Microscope (HRTEM), Scanning Transmission Electron Microscopy (STEM), Scanning Electron Microscopy (SEM), EDS, X-ray Diffraction (XRD), Nanoindentation, and AFM

Research Assistant Jan 2008 - Aug 2010
San Jose State University Research Foundation San Jose, CA

- Synthesized thin films for solar cells using PVD methods (RF/DC Sputtering, Thermal Evaporation), Lithography, Etching, and Diffusion
- Mastered material characterization techniques: XRD, SEM, EDS, EBSD, and Optical Profilometer
- Utilized design of experiment, nucleation and growth thermodynamics, diffusion in binary systems, and corrosion analysis toward the project goal

Professional Experience

Laboratory Assistant Nov 2012 - Jun 2015

Laboratory for Electron and X-ray Instrumentation Irvine, CA

- Provided basic and advanced training for student and industry users for the following instruments: SEM, TEM, FIB, XRD, Sputter Coating, and Plasma Cleaner
- Maintained and helped with the troubleshooting of SEM/FIB/TEM/XRD instruments
- Delivered consultation and solution development for industrial and academic projects

Process Engineer Jun 2006 - Dec 2007

Poolad Consulting Engineers *Tehran, Iran*

- Conducted feasibility study of mineral processing plants with 1 million ton per year production capacity
- Prepared tender document and constructed engineering reports and industrial contracts

Leadership and Teaching Experience

- Mentored high school, undergraduate, and graduate students in research methods — 2010 - 2014
- ASM International Orange Coast Chapter: Executive member — Since Oct 2012
- Chemical Engineering and Materials Science Graduate Student Association: Outreach coordinator and event organizer — 2010 - 2013
- Intel International Science and Engineering Fair (ISEF): Organized San Jose State team for the event — 2010
- Lectured "Introduction to Materials Engineering" course for undergraduates in engineering — Fall 2008 - Spring 2010

Awards

- Winner of Science as Art competition at MRS conference in Boston, MA — Fall 2014
- Awarded UC Irvine Engineering Graduate Student Fellowship — Fall 2010

Selected Presentations

- The Material Research Society Fall Meeting & Exhibit, Boston, MA — Dec 2014
- The 143rd TMS Annual Meeting and Exhibition, San Diego, CA — Mar 2014
- Southern California Society for Microscopy & Microanalysis, Los Angeles, CA — Mar 2013

Publications

1. "Manipulating the interfacial structure of nanomaterials" Khalajhedayati A, Pan Z, Rupert TJ (Submitted).
2. "High-temperature stability and grain boundary complexion formation in a nanocrystalline Cu-Zr alloy" Khalajhedayati A, Rupert TJ (Submitted).
3. "Grain boundary character distributions in nanocrystalline metals produced by different processing routes" Bober DB**,** Khalajhedayati A, Kumar M, Rupert TJ (Submitted).
4. "Mechanical characterization of electro-mechanically spun carbon micro/nano-fibers" Canton G, Khalajhedayati A, Umbert Ceresuela P, Rupert TJ, Madou M (Submitted)
5. "Disruption of Thermally-Stable Nanoscale Grain Structures by Strain Localization" Khalajhedayati A, Rupert, TJ Scientific Reports (2015) 5:10663.
6. "Emergence of localized plasticity and failure through shear banding during microcompression of a nanocrystalline alloy" Khalajhedayati A, Rupert TJ, Acta Materialia, (2014) 65:326.
7. "SU8 Derived Glassy Carbon for Lithium Ion Batteries" Sharma S, Khalajhedayati A, Rupert TJ, Madou MJ. Electrochemical Society (ECS) Transactions, (2014).

Computer Skills

- Matlab (advanced), Visual Basic (intermediate)
- Open source Image analysis: ImageJ (advanced), GIMP: Photoshop alternative (intermediate)
- Microsoft Excel (advanced), Word (advanced), Power Point (advanced), Web design (intermediate)

Abstract of the dissertation

Grain boundary structure and interfacial complexions for the creation of tough, stable nanocrystalline metals

by

Amirhossein Khalajhedayati

Doctor of Philosophy in Materials Science and Engineering

University of California, Irvine, 2015

Professor Timothy J. Rupert, Chair

Nanocrystalline metals have been the focus of current literature due to their interesting mechanical properties. This is a result of having nanometer sized grains and high volume fraction of grain boundaries. While these materials have high strength, the large number of boundaries is also responsible for the limited ductility and thermal instability often observed for nanocrystalline systems. Despite the current efforts in the literature, these challenges still prevent widespread use of nanocrystalline metals in real engineering applications. In this thesis, we study these problems by focusing on tailoring the grain boundary structure and chemistry and propose a methodology that can be used to mitigate those challenges. First, we study the plastic flow and failure as a function of grain boundary volume fraction (i.e., grain size) using microcompression in a nanocrystalline Ni-W. Since grain boundary physics are extremely important here, we also study how the relaxation of nonequilibrium grain boundaries affects failure. We show that nanocrystalline metals with larger grain boundary volume fractions and relaxed boundary structures are stronger, but also more likely to fail prematurely through catastrophic shear banding. We also show that shear banding can create a dynamic microstructure leading to grain coarsening. A major take-away from this work is that disordered grain boundaries can actually be beneficial. Therefore, in the next study we introduce amorphous complexions, highly disordered grain boundaries, through grain boundary doping as an all-in-one solution to design against failure and thermal instability. We use nanocrystalline Cu with the addition of Zr as our model system to explore complexion engineering in these materials. High resolution transmission electron microscopy in conjunction with energy dispersive x-ray spectroscopy demonstrates segregation of Zr to the boundaries of Cu-Zr alloys created with mechanical alloying. This provided evidence for the formation of amorphous grain boundaries complexions under certain conditions. Microcompression and in-situ bending experiments are then used to quantify the effect of doping on mechanical behavior. Finally, our results show that strength, strain-to-failure, failure mode, and thermal stability can be controlled with boundary doping. The proposed methodology described here is rather general and can be applied to other material systems to make bulk nanocrystalline metals with improved mechanical properties.

Chapter 1 : Introduction

1.1 Mechanical behavior of nanocrystalline metals

Nanocrystalline metals, commonly defined as polycrystals with a mean grain size (d) of less than 100 nm, are promising structural materials [1], mainly due to reports of high strength [2,3], fatigue resistance [4,5], and wear resistance [6-8]. The seminal works of Hall [9] and Petch [10] in the 1950's showed that the strength of a crystalline metal increases with the inverse square root of grain size, predicting that GPa-level strength would be achievable for extreme grain refinement (Fig. 1.1). Since that time, however, research has shown that the Hall-Petch relationship breaks down when grain size reaches the nanocrystalline range [11,12]. For grain sizes below ~100 nm, strengthening with grain refinement is still observed but some reports show that the inverse square root dependence on grain size no longer persists. For example, Choi et al. observed what they called a positive deviation from Hall-Petch behavior, where their experimental data from nanocrystalline Al with d = 48-72 nm showed strength that was inversely proportional to grain size [13]. Another major change in the dependence of strength on grain size is found when average crystallite size is reduced below ~10-20 nm. Experimental research often reports a plateau in strength with further grain refinement [14,15], while molecular dynamics simulations more commonly report an "inverse Hall-Petch" trend where reduction in grain size actually decreases strength [16-19]. Recent work from Trelewicz and Schuh [20] consisting of quasi-static and dynamics nanoindentation experiments has shown that this disagreement is likely due to the difference between the strain rates that are commonly applied in experimental and computational techniques. A maximum rate sensitivity of strength was found at a grain size of ~12 nm, meaning that high strain rates such as those used in molecular dynamics simulations would show a

maximum strength at an intermediate grain size and inverse Hall-Petch scaling at smaller grain sizes.

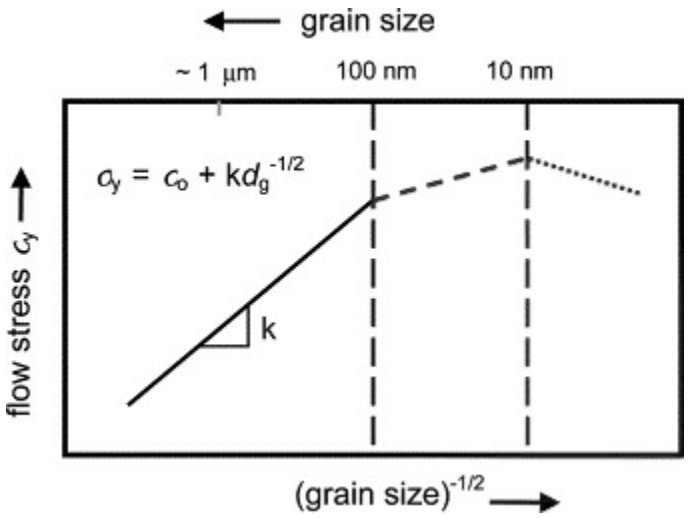

Figure 1.1 The Hall-Petch relationship showing the effect of grain size on flow stress [1].

1.1.1 Grain boundary dominated plasticity and failure

The observation of new structure-property scaling laws in nanocrystalline materials is interesting scientifically because it signals the emergence of new physical mechanisms responsible for plasticity. The change in strengthening slope observed below $d \sim 100$ nm is believed to be related to a shift from plastic deformation that is controlled by intragranular dislocation sources to grain boundary sites acting as sources and sinks for dislocation activity. Molecular dynamic simulations were able to show the nucleation (Fig. 1.2(a)) and absorption of partial dislocations at the grain boundary of nanocrystalline Ni [21]. Van Swygenhoven et al. [22] used molecular dynamics simulations to study the deformation physics of nanocrystalline Al and found that dislocation nucleation and propagation was limited by activity at grain boundary sites. Interestingly, they found that these dislocations often became pinned at grain boundary ledges as they moved through the grain, giving the spacing between boundary pinning points as the characteristic length scale of the mechanism. This interpretation has been supported by Huang et

al. [23], who showed that experimental data could be well-described by a model that invokes Orowan-type pinning of dislocations with the grain size taken as the distance between obstacles. The behavior of nanocrystalline materials with grain sizes blow ~10-20 nm has been attributed to the emergence of grain boundary sliding and rotation as the dominant carriers of plastic deformation. Schiotz et al. [24,25] were the first to report such a mechanism when they detected local sliding events during molecular dynamics simulations of nanocrystalline Cu. Grain boundary sliding was also observed during a molecular dynamics study of nanocrystalline Ni by Van Swygenhoven et al. [26], where more detailed analysis showed that this process takes place by either atomic shuffling or stress-assisted free volume migration.

Recent studies have shown not only that plasticity is grain boundary dependent, but also that failure is directly related to grain boundary structure in nanocrystalline materials. Electron microscopy studies have shown the formation of nano-voids in the grain boundary and triple junctions in front of a moving crack [1,27]. These interfacial voids can join together to make a larger micron size crack and cause intergranular fracture. Molecular dynamic simulations on nanocrystalline materials also support the formation of nano-voids at the grain boundaries [28-30]. Fig 1.2(b) shows the formation of a crack at the grain boundaries of nanocrystalline Ni at 12% strain by using molecular dynamic simulations.

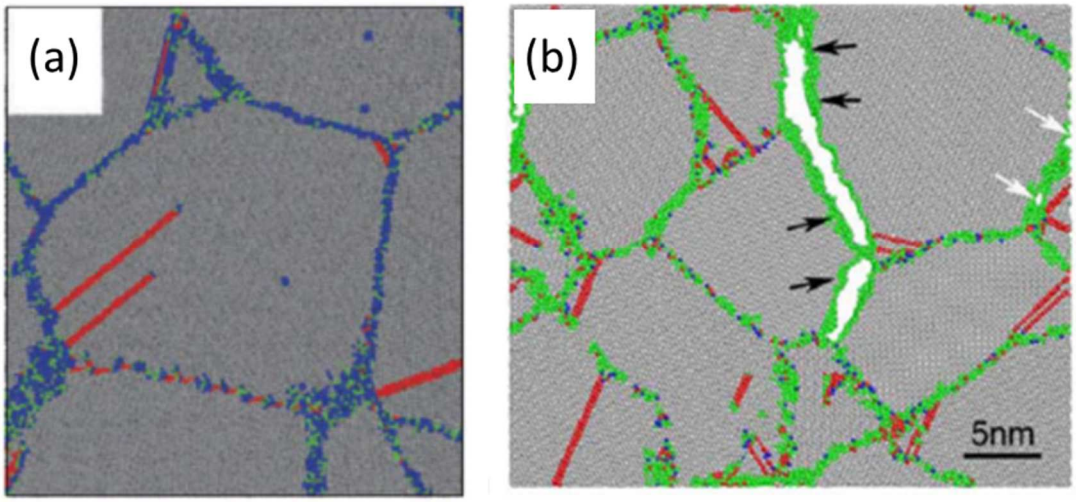

Figure 1.2 (a) Molecular dynamic simulation showing nucleation of partial dislocations at grain boundary of nanocrystalline Ni [21]. (b) Molecular dynamic simulation showing formation of a crack at the grain boundary of nanocrystalline Ni at 12% strain. The loading axis is horizontal [28].

The common feature of the new deformation physics described here is the increased importance of grain boundaries as facilitators for plastic deformation and failure. Since grain boundaries are more abundant and more important in nanocrystalline systems, increased attention has been focused on studying the atomic structure of these interfaces. A number of studies have reported that nanocrystalline metals often contain nonequilibrium grain boundaries, characterized by excess free volume or grain boundary dislocations, in their as-prepared state [31,32]. However, this nonequilibrium structure can be easily relaxed into a more ordered state by applying low temperature heat treatments [32,33], with a more ordered and connected grain boundary structure found after relaxation. Perhaps not surprisingly since boundaries are so important for nanocrystalline plasticity, reports have shown that mechanical strength is highly dependent on this grain boundary structural state. Detor and Schuh [34] showed that grain boundary relaxation resulted in a significant increase in hardness, even though grain size was unchanged. Rupert et al.

[35] further isolated this effect through systematic nanoindentation at different grain sizes, showing that this hardening occurred quickly and was grain size dependent.

From the discussion above, it is clear that overcoming the main challenges in this class of materials such as low fracture toughness and low strain-to-failure [36-38] becomes tightly bonded on the structure of the grain boundaries. The issue of limited ductility in nanocrystalline materials comes from the lack of inefficient accommodation of dislocation plasticity, leading to microcracks, or a lack of strain hardening. In recent years, several methods have been proposed to improve the toughness and ductility of nanocrystalline materials. One common strategy includes dispersing a larger grain size into the structure of a nanocrystalline material, which results in improved the strain hardening ability [39-41]. While this increases ductility, these materials with bimodal grain sizes do so at the expense of strength. Another method for improving ductility is the promotion of mechanically-induced grain growth. Rupert et al. [42] showed that shear strain can be accommodated by the motion of grain boundaries in pure nanocrystalline materials at the expense of grain coarsening, but again this is accompanied by a decrease in strength. A different approach to the issue of limited ductility was to develop ultra-fine-grained materials with a high density of nano-sized twin boundaries [43,44]. Although such materials are promising, they cannot be applied to wide range of materials, since the formation of nanotwinned grains is only possible for materials with low stacking fault energy. This research has been done mainly on Cu for this reason. The challenge still remains for many other nanocrystalline systems, and it is clear that a new approach is required to improve the ductility of nanocrystalline materials.

1.1.2 Emergence of glass-like shear banding

As a result of the novel deformation mechanisms, Schuh and Lund [45] suggested that nanocrystalline systems with $d < 10$ nm should have mechanical properties which resemble those of metallic glasses. This concept was first supported by the observation that nanocrystalline metals exhibit a tension-compression asymmetry of their strength and shear transformation zones operate inside of grain boundary regions during plasticity [46]. Recent molecular dynamics (MD) simulations [47] have uncovered a universal relation between strength and modulus in nanocrystalline alloys that resembles prior observations of metallic glasses [48]. Another connection between the mechanical behavior of metallic glasses and nanocrystalline metals was found when Trelewicz and Schuh [14] explored the plasticity of nanocrystalline Ni-W using nanoindentation and found shear steps in the pileup surrounding the indents for average grain sizes of 6 nm and 3 nm, with more significant steps observed in the finer grained sample (Fig. 1.3). The shear offsets observed in this study were similar to observations from the metallic glass literature, such as the shear banding found after nanoindentation of an Al-based metallic glass by Jiang et al. [49].

When shear banding is observed in metallic glasses, it is often accompanied by structural evolution, most commonly in the form of crystallite formation [50,51]. However, the effect of shear banding on the structure of nanocrystalline materials has not been explored thoroughly, with experimental evidence especially scarce. Wei and coworkers did observe grain coarsening inside of shear bands in ultra-fine grained (typically meaning 100 nm $< d <$ 1000 nm) Fe with d of 110 nm [52], as well as ultra-fine grained W [53] and Ta [54]. However, these materials have average grain sizes that are larger than what would be considered nanocrystalline and were all body centered cubic (BCC) metals, meaning a direct extrapolation to nanocrystalline face centered cubic

(FCC) metals such as Cu, Al, or Ni is not possible. Some insight has been provided by MD simulations, but these studies have been limited to pure, single element metals. For example, Sansoz and Dupant [55] studied nanoindentation of nanocrystalline Al with d = 5 nm and d = 7 nm at absolute zero temperature and reported grain growth due to grain rotation and grain boundary migration inside of shear bands. More recently, Rupert [56] observed the formation of shear bands during simulated tensile testing of a nanocrystalline Ni with d = 3 and 6 nm using MD. These studies show that the grain structure in pure nanocrystalline materials can be considered dynamic under mechanical loading.

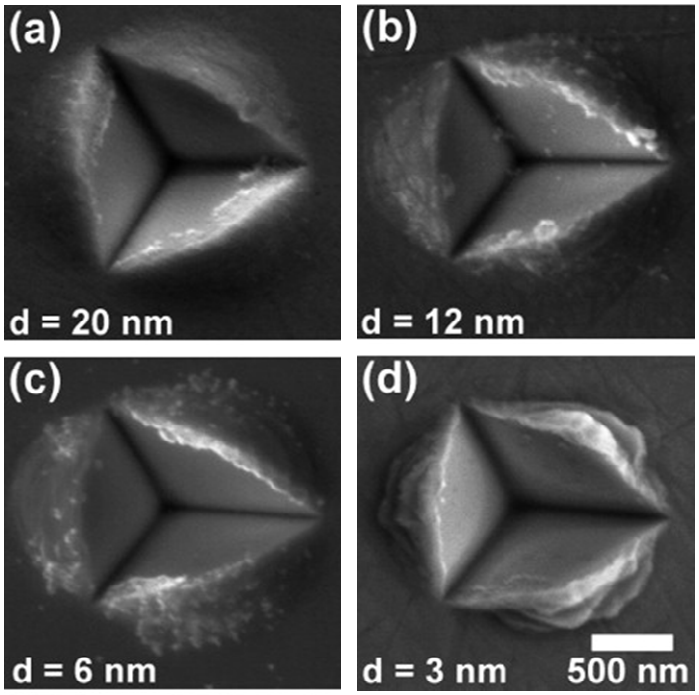

Figure 1.3 Scanning electron micrograph (SEM) of nanoindentation experiment on nanocrystalline Ni-W with different grain sizes [14].

1.1.3 Extrinsic vs intrinsic ductility

As discussed previously, novel deformation physics control deformation in nanocrystalline materials and these properties should be sensitive to grain boundary state. To understand these new behaviors, we need to observe the response of nanocrystalline materials under a simple

applied load, i.e., uniaxial compression or tension. However, the vast majority of studies which probe mechanical behavior systematically as a function of grain size or grain boundary state rely on indentation experiments (e.g., [14,34,35,57-59]). While such techniques allow for large number of tests and only require small volumes of material, they also only give a scalar measurement of strength. As a result, the community has very little reliable information about how the novel deformation mechanisms in nanocrystalline materials impact more complex behavior, like strain hardening and failure. In addition, nanoindentation imposes a complex, three-dimensional stress state which makes it difficult to connect to constitutive theories for yielding and also adds concerns about the effect of a large confining pressure on plasticity. In order to study strain hardening behavior, full plastic flow, and the failure of nanocrystalline materials in a straightforward manner, a simple uniaxial tension or compression test is required. However, such testing has to date been problematic as premature failure can occur for two main reasons: (1) improper specimen geometry, and (2) defects resulting from the fabrication process.

Early attempts at uniaxial testing of nanocrystalline materials largely consisted of creating dog-bone specimens from thin sheets of nanocrystalline metals (e.g. [60-62]). This means that the samples commonly had thicknesses that were orders of magnitude smaller than the in-plane dimensions. Such geometries are problematic, as they introduce a geometric sample size effect, with strain-to-failure decreasing with sample thickness [63]. Brooks et al. [64] explored this effect specifically in nanocrystalline Ni, showing that samples with thicknesses below ~100 μm experienced macroscopically brittle fracture that was not representative of the intrinsic material response. Unfortunately, such thin samples are common within the uniaxial testing literature, where they are often used out of necessity since it is difficult to deposit thicker, high quality nanocrystalline films. Sharon et al. [60] recently reviewed these geometric effects on

nanocrystalline uniaxial testing, showing that they can lead to premature sample necking and that they produce strain-to-failure measurements that are not representative of the material's ability to plastically deform in a stable manner (Fig. 1.4). Zhao et al. [65] showed that by making sample geometries defined by ASTM Standard E8 [66], the strain-to-failure becomes independent of thickness, leading to a recommendation that the comparison of strain-to-failure of a nanocrystalline material with different tensile test specimen geometry should be done cautiously.

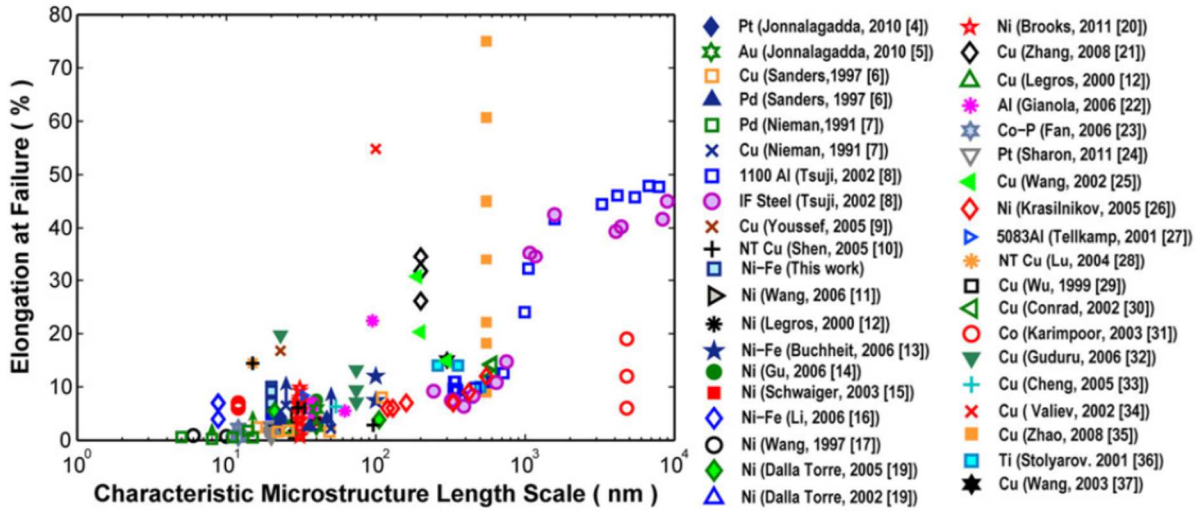

Figure 1.4 The effect of characteristic length scale on elongation to failure of various nanocrystalline metal systems [60].

Another complication that precludes the simple application of traditional uniaxial testing techniques to nanocrystalline materials is the effect of processing defects. Research has shown that nanocrystalline materials are commonly plagued by incomplete consolidation of particles, surface flaws, sulfur-induced grain boundary embrittlement, and hydrogen pitting, all of which can cause premature failure [61,67,68] . For example, nanocrystalline Cu [69] and Ni-Fe [67] showed increased strain-to-failure with improved processing chemistry that reduced particulate contamination and hydrogen pitting. Brooks et al. [64] also explored this issue in detail. Samples

produced by an optimized process were found to experience twice as much plastic strain before failure, while the samples without this optimization always failed at large void-like defects produced when hydrogen gas was trapped in the deposit. Therefore, without having a proper geometry for mechanical testing and samples that are free of processing defects, conventional testing methods cannot provide us with accurate results and an alternative uniaxial testing technique is needed to adequately probe the plastic flow and failure response of nanocrystalline materials.

Recently, microcompression testing has become a promising and reliable technique that can be used to acquire the mechanical properties from a small volume of material [70,71]. Although this testing method is often used to study the effects of external sample size on mechanical behavior (e.g., [72]), such micropillars can actually serve as a bulk mechanical testing technique if the characteristic length scale associated with the microstructure of the material is much smaller than the pillar size (Fig. 1.5). For a material with a grain size in the nanometer range, hundreds of thousands to millions of crystallites will be contained inside of a pillar with a diameter of at least a few microns. For this reason, we suggest that micropillar compression can be used to measure the intrinsic properties of nanocrystalline materials. With microcompression, one can use sample aspect ratios that are small and within the range of ASTM standards while also minimizing the possibility of processing voids and defects being trapped in the small volume of material that is probed. Such a method opens a path for the accurate quantification of plastic flow and failure in nanocrystalline materials under simple loading conditions.

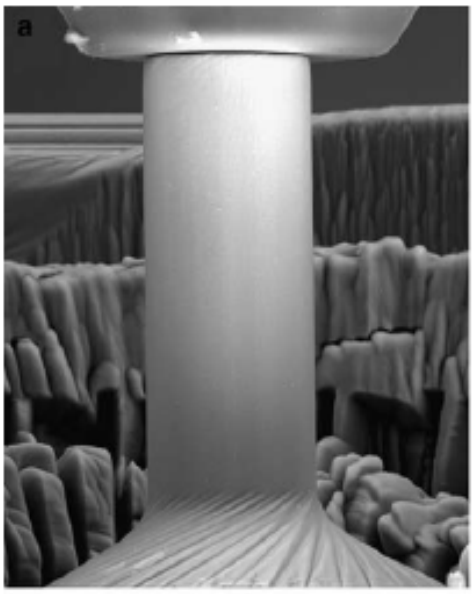

Figure 1.5 SEM image of the a uniaxial microcompression testing setup [73].

1.2 Grain boundary doping: Failure and structural stability

The problem of low ductility and low fracture toughness is directly coupled with many other issues in the design of nanocrystalline metals. For example, nanocrystalline metals suffer from microstructure instability at low temperature and grain growth can hinder their use in real life applications where they lose their original properties over time. Recently, research has shown that addition of alloying elements to the pure nanocrystalline system is advantageous for several reasons. In practice, alloying with a second element is often required, since pure nanocrystalline metals can undergo thermally-driven grain growth even at room temperature in some cases [74]. Grain boundary doping which is segregation of these alloying elements to the grain boundaries can not only reduce the grain boundary energy but also introduce new grain boundary structures. In this section we explore these effect in more detail.

1.2.1 Thermal stability

One of the major roadblocks in widespread implementation of nanocrystalline metals is connected to the thermal stability needed to consolidate them into bulk form [60,75]. The high grain boundary fraction gives a large driving force for coarsening and nanocrystalline materials exhibit limited thermal stability [76], with grain growth even being reported at room temperature for pure nanocrystalline metals [77]. Fig. 1.6 compares the grain growth of pure nanocrystalline Cu with different nanocrystalline Cu alloys. It is clear that the pure nanocrystalline Cu has an extreme tendency to grain growth even at low temperature while alloyed nanocrystalline Cu shows much better thermal stability.

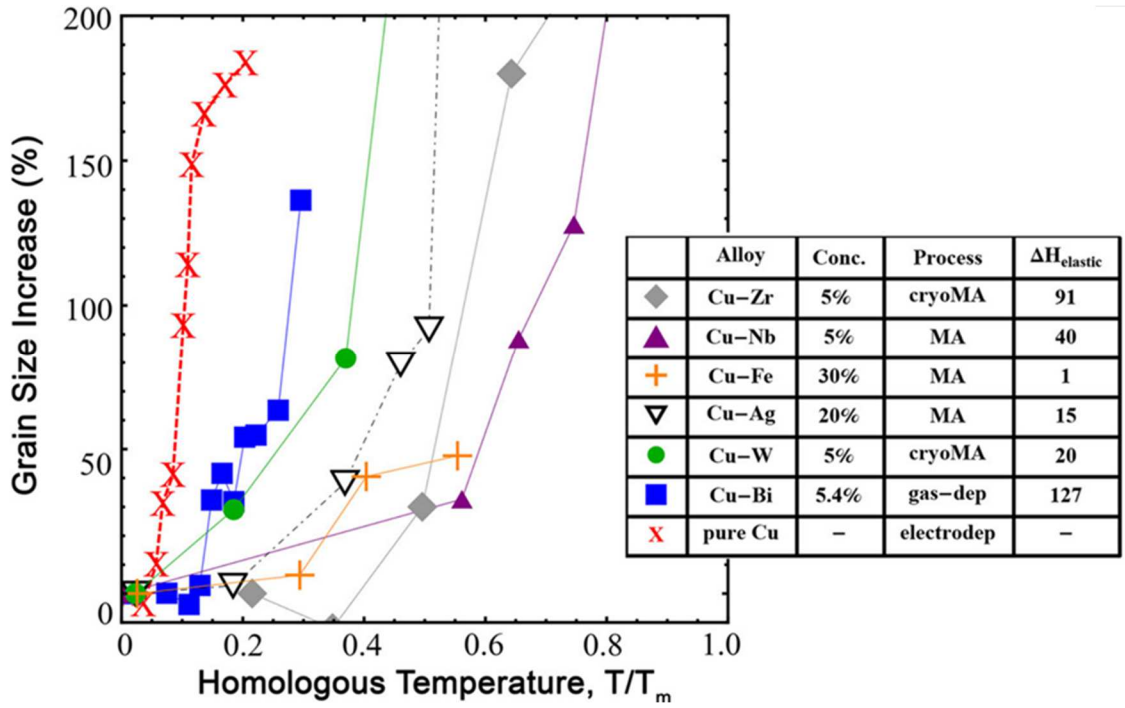

Figure 1.6 the effect of alloying on the grain growth of binary nanocrystalline Cu alloys [78].

The lack of thermal stability can be addressed in two ways: thermodynamic stabilization or kinetic stabilization of the microstructure. The former is achieved by reducing the excess grain

boundary energy [79] while the latter is achieved by reducing the grain boundary mobility [80]. The effect of these two mechanisms can be summarized by Eq.1.1 [78]:

$$v = M \times P = M_0 \exp\left(\frac{-Q_m}{RT}\right) \times \frac{2\gamma}{r} \quad (1.1)$$

where v is the curvature driven velocity of a grain boundary during grain growth, M is the grain boundary mobility, P is the driving force for grain growth, M_0 is a mobility constant, Q_m is an activation energy, γ is grain boundary free energy per unit area, and r is the radius of curvature. To obtain a stable microstructure, either M or P should be reduced, ideally to zero if stability is expected over long time periods. Kinetic approaches often rely on precipitation of second phase particles or solute drag that reduces the grain boundary mobility by applying a pinning pressure on grain boundaries [81]. However, based on Eq.1, the mobility term follows an Arrhenius function and extremely high temperatures can ultimately make kinetic approaches impractical. In thermodynamic approaches, γ should be reduced since the driving force for grain boundary migration is proportional to grain boundary energy. This is often done by doping grain boundaries with a solute that has a large atomic size mismatch with the solvent atoms. Grain boundary free energy is much less temperature dependent, and thermodynamic methods are philosophically more promising since they could stabilize a microstructure indefinitely [15,82,83]. The common theme between both approaches is that alloy systems are required for high stability, meaning that the doping of nanocrystalline materials should be studied in more detail.

Chookajorn et al. [79] showed that reducing grain boundary energy by doping these interfaces can be a powerful design strategy for the creation of thermally-stable nanocrystalline materials, demonstrating this concept by producing a W-20 at.% Ti alloy that retained a 20 nm grain size even after being exposed to 1000 °C for one week. An exemplary material system that uses this concept of grain boundary dopants to its advantage is nanocrystalline Ni-W. Detor and

Schuh [15] created thermally-stable Ni-W alloys with grain sizes ranging from ~140 nm down to ~3 nm, tuned by controlling the W concentration, using electrodeposition. Recent studies have shown that alloying can also change a nanocrystalline materials resistance to mechanically-driven structural evolution. For example, extremely pure nanocrystalline Al was observed to experience dramatic grain coarsening under uniaxial loading [84], but the addition of small amounts of O into such films stabilized the grain structure [85]. Similarly, Lohmiller et al. [86] found that pure Au is prone to stress-induced grain growth, while Au with Cu segregated to the grain boundaries is not.

A number of theoretical models have been developed to predict candidate elemental combinations for thermally-stable nanocrystalline materials, most using readily available thermodynamic parameters [81,87]. For example, Murdoch and Schuh[88] developed a comprehensive model using a Miedema-type [89] approach for the estimation of grain boundary segregation enthalpy, with their model being independent of temperature and grain boundary solute concentration. These authors used this model to find the most thermally-stable binary alloys and confirmed previous experimental observations, such as excellent thermal stability in nanocrystalline W-Ti with a grain size of ~20 nm [79] and a combination of phase separation and grain growth in nanocrystalline Cu-Ag [90]. In a similar manner, to predict the stability of many nanocrystalline systems due to grain boundary segregation, Darling et al. [91] created stability maps showing the minimum solute composition required to reduce excess grain boundary energy to zero at different grain sizes and temperatures. Both of these studies serve to guide researchers in their selection for system candidates when engineering thermally-stable nanocrystalline alloys through grain boundary segregation.

From the discussion here, it is clear that doping can increase the stability of nanocrystalline grain structures, at least to evolution caused by temperature or simple stress states. The stability of nanocrystalline materials is essential for fabrication of bulk sized sample which requires high temperature during consolidation and sintering. Although, with recent advances, this problem is better understood, however not many nanocrystalline metals are shown experimentally to be stable enough to design a true bulk nanocrystalline metals. This topic is still an ongoing research effort.

1.2.2 Grain boundary complexions

Besides having an important role in reducing grain boundary energy, grain boundary doping can drive the formation of new interfacial structures at the grain boundaries and controlling mechanical failure [92]. Initially, Hart [93] suggested that grain boundary segregation can lead to the nucleation of grain boundary phases that could explain embrittlement in steel. Subsequently, Clarke and Thomas [94] were able to directly show evidence of interfacial "phase-like" structures in a MgO-doped Si_3N_4 ceramic using high resolution transmission electron microscopy (TEM). Many studies have since reported on the effects of these grain boundary structures on the overall physical and mechanical properties in metals and ceramics, such as the being cause for solid state activated sintering and abnormal grain growth [95-103].

Recently, Tang et al. [104] introduced the term *complexion* to differentiate grain boundary "phases" from traditional bulk phases. The main reason for this convention is that complexions depend on their abutting grains and cannot exist as separate entities [92]. However, there are some similarities which are useful for materials design. Grain boundary complexions, like bulk phases, can be described with thermodynamic parameters and can transition between complexion types due to changes in variables such as temperature, pressure, local chemistry, or grain boundary

character [92]. Dillon et al. [105] categorized complexions into six types based on the grain boundary thickness and solute adsorption (Fig. 1.7): monolayer and sub-monolayer adsorption (Type I), clean or undoped grain boundaries (Type II), bi-layer absorption (Type III), multi-layer adsorption (Type IV), nanoscale intergranular films (Type V), and wetting films (Type VI). Complexion types I-V are only in equilibrium when sandwiched between abutting crystals, while complexion type VI can be in equilibrium at an interface or by itself as a standalone phase. Complexion types V and VI are often disordered, in which case they can both be broadly classified as amorphous intergranular films (AIFs).

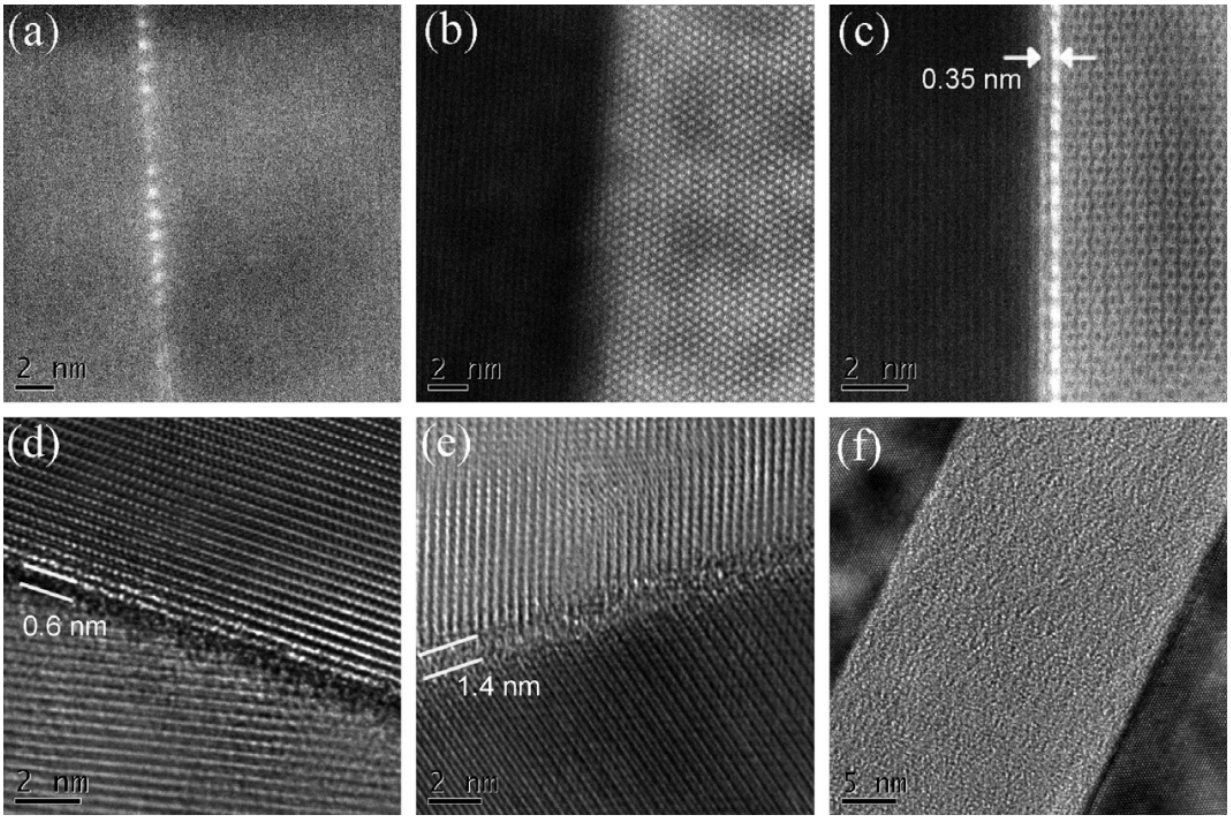

Figure 1.7 High resolution TEM images of Dillon-Harmer complexation type I-VI in Al_2O_3 [105].

One type of complexion that is specifically interesting for this work is the AIF. These intergranular grain boundary films have been observed with high resolution TEM in many different

ceramic systems [106-111]. Similar interfaces have been observed in metallic systems indirectly [112-115] as well as by using high resolution TEM [116]. Luo et al. [117] have shown the possibility of forming an equilibrium, amorphous grain boundary phase in the nickel-doped tungsten alloy. Fig. 1.8 shows high resolution TEM experiments on the 1 at. % W-Ni alloy displaying the formation of a grain boundary complexion by annealing to just below the eutectic temperature.

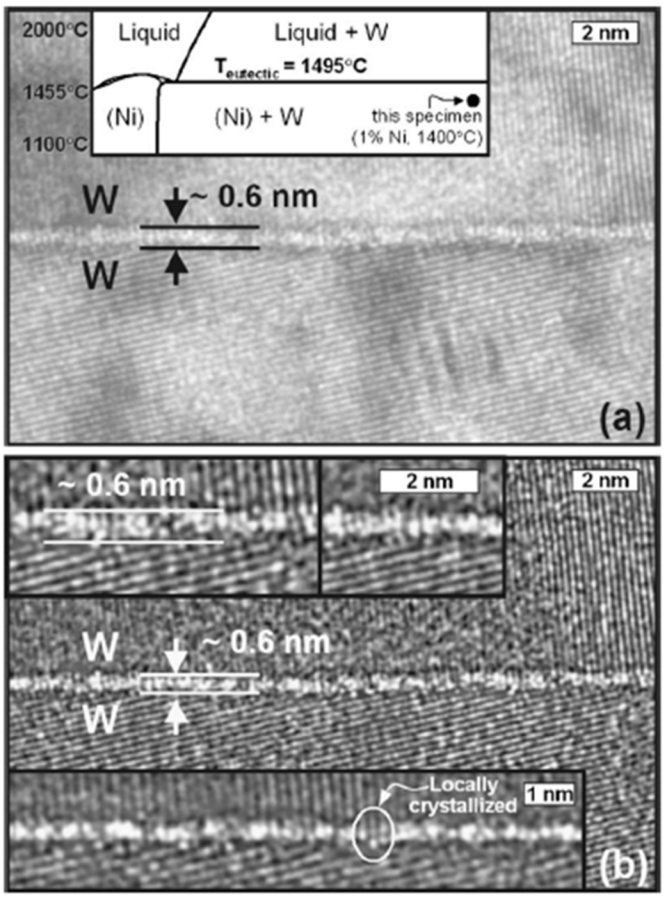

Figure 1.8 High resolution TEM image of an amorphous grain boundary complexion in the W + 1 at. % Ni. (a) Raw data and (b) a digitally enhanced image [117]. The equilibrium phase diagram for W-Ni is included in the inset to (a).

Luo et al. [118] showed the necessity for creation of grain boundary phase diagrams which can help to predict the properties such as subsolidus activated sintering. In recent years, several studies have been done to study the thermodynamic parameters affecting the formation of grain

boundary complexions by changing chemistry and heat treatment [104,119-121]. One such a phase diagram is shown in Figure 1. Fig 1.9. One key characteristic is that higher temperature allows for thicker grain boundary complexions to form, and the thickness of the interfacial complexion is directly related to the annealing temperature [118]. The discussion of the impact of complexions on material properties has been almost exclusively limited to transport properties such as diffusion. One notable exception is the identification of a bilayer complexion in Cu-Bi as the cause of liquid metal embrittlement in that system [112].

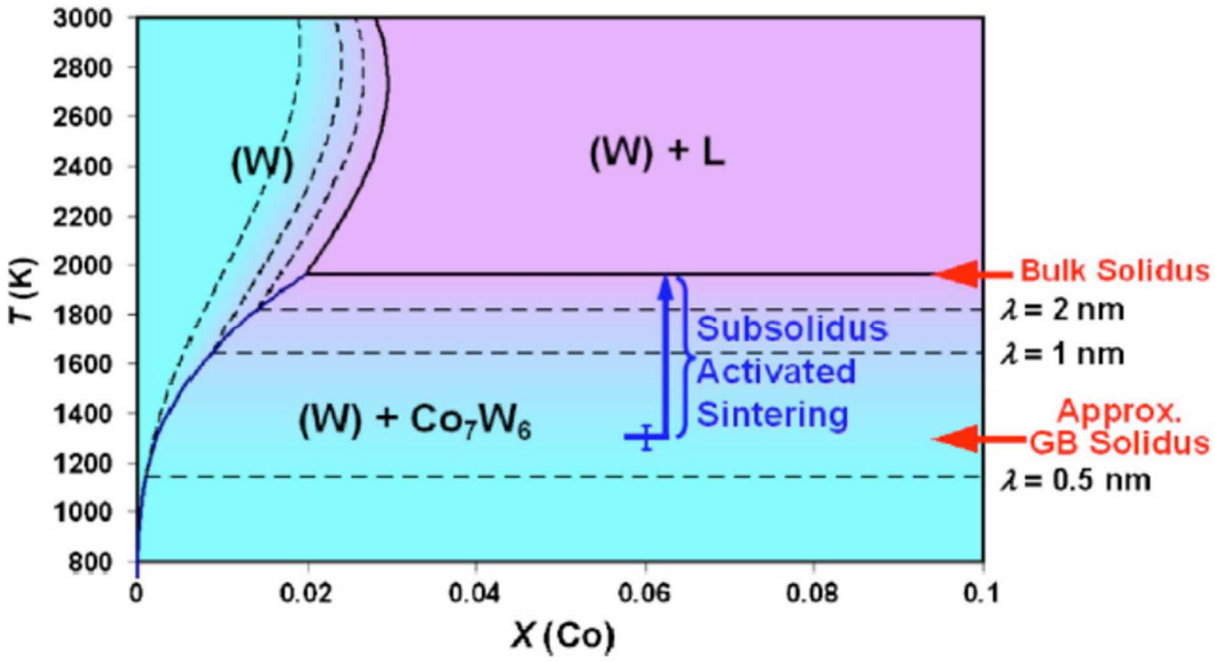

Figure 1.9 Computational binary phase diagram for W-Co binary system showing different stable interfacial phase thicknesses over different compositions [118].

The lack of strain hardening and propensity for early fracture in nanocrystalline metals can also be related to the ability of the grain boundary in absorbing the mobile defects. To accommodate defects, interfaces are required to have excess free volume [30]. In the absence of this free volume, dislocations cannot be absorbed and microcracks can form. By tuning the

chemistry of the grain boundary and adding a stable disordered complexion, it may be possible to increase the ductility of nanocrystalline materials. Molecular dynamic simulations by Pan and Rupert [122,123] on Cu bicrystals doped with Zr showed that complexions in the form of AIFs (complexion types V or VI) can increase the damage tolerance of a grain boundary by absorbing multiple dislocations and acting as an efficient sink for dislocations. These authors also showed that thicker AIFs are capable of absorbing more dislocations and delaying intergranular void formation to higher shear strains [122]. Because nanocrystalline metals with grain size above 10 nm plastically deform through grain boundary dislocation emission and absorption,[59] grain boundary complexions should have a major impact on the ductility and toughness of these materials.

In fact, this hypothesis is supported by the work of Wang et al. [124] on nanocrystalline Cu/Cu-Zr nanolaminates. Although they were not complexions created by thermodynamic driving forces, the thin amorphous layers that were added between nanocrystalline Cu layers were found to increase ductility when compared to a monolithic nanocrystalline Cu film. Fig. 1.10(a) shows a high resolution TEM image of a nanolaminate of crystalline Cu and amorphous Cu/Zr layer which acts as a sink for incoming dislocations. Metallic glasses are expected to have near zero ductility and to be brittle, but, with addition of the metallic glass phase between the layers of nanocrystalline Cu, the strain-to-failure of the material increased noticeably (Fig. 1.10(b)). Although, a metallic glass is brittle in its bulk form, by having a small thickness here, the metallic glass layer cannot form mature, catastrophic shear bands [125,126]. Fig. 1.10(c) shows the formation of forest sessile dislocation after yielding in the Cu and Cr/Zr nanolaminates. After the application of a few percent plastic strain, the density of dislocations decreases, as shown in Fig. 1.10(d). The dislocations get absorbed into the amorphous grain boundary layer. Therefore, by

changing the grain boundary structure through addition of a second alloying element, it should be possible to improve the ductility while avoiding crack nucleation.

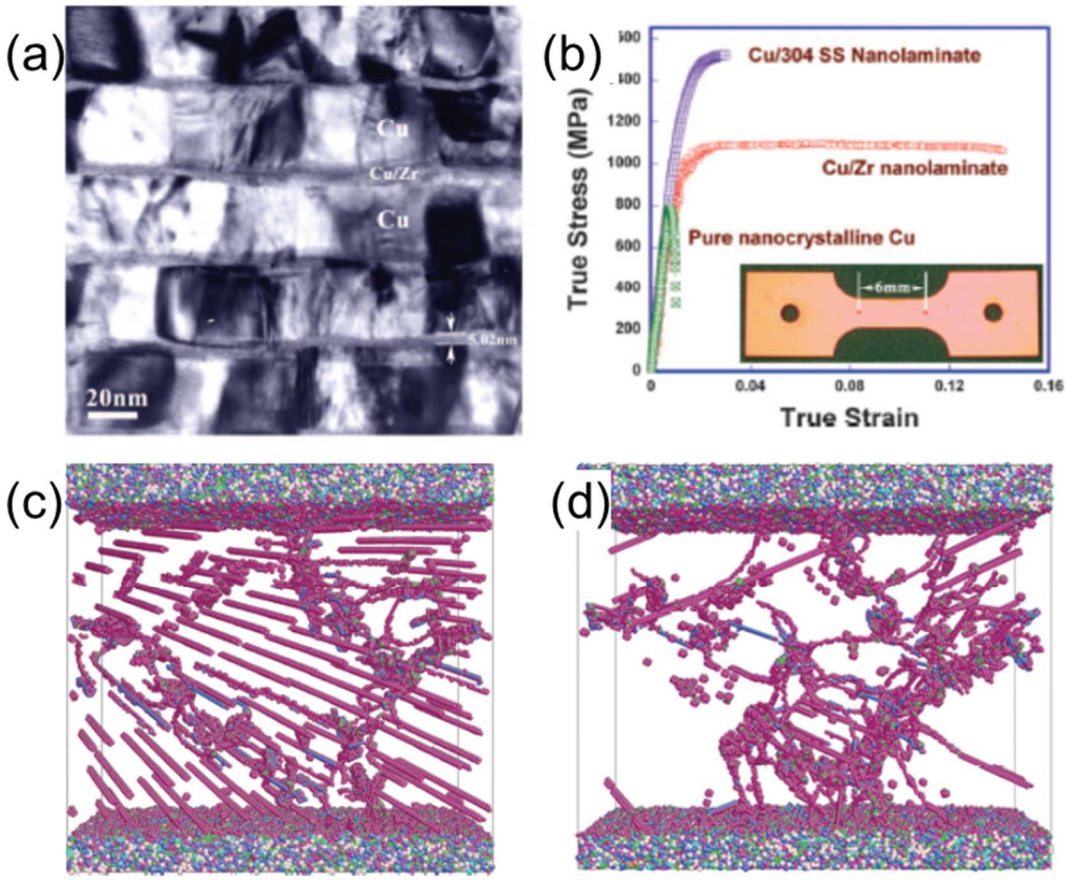

Figure 1.10 (a) High resolution TEM image of nanolaminates of Cu and Cu/Zr. (b) Stress-strain curves of a Cu/Zr nanolaminate, nanocrystalline Cu, and a Cu/Stainless Steel nanolaminate. (c) Formation of sessile dislocations after yielding of Cu/Zr nanolaminates. (d) Decrease of dislocation density by application of more plastic strain to the sample after yielding [124].

1.3 Problem statement and research objective

It is clear that grain boundary structures have important effects on the flow and failure of nanocrystalline metals. Consequently, an obvious solution for ongoing problem of low ductility and thermal instability is to design and study novel grain boundary structures in nanocrystalline metals. However, this idea is recent, and a complete picture of the effect of grain boundaries is

still lacking. Therefore, it is the goal of this thesis to focus on isolating the effect of grain boundary structures on different aspects of physics and mechanics of nanocrystalline metals. The studies done toward this objective in this thesis are categorized in four chapters:

- Chapter 2: Microcompression testing was used to study the effect of grain size and grain boundary relaxation on flow and failure behavior of nanocrystalline Ni-W with grain sizes from 5 to 90 nm. The results of this study guided us in the selection and design of failure resistant nanocrystalline structure.
- Chapter 3: The effect of shear localization on structural stability was studied in nanocrystalline Ni-W with a 5 nm average grain size. The microstructure of the shear bands formed during uniaxial microcompression and nanoindentation experiments were characterized with TEM to understand how extreme deformations influence grain structure.
- Chapter 4: A new technique was developed to introduce grain boundary complexions in a nanocrystalline Cu-Zr to design against failure and thermal instability. The effect of these new grain boundary structures on toughness and strength were explored.
- Chapter 5: Formation of the grain boundary complexions with different annealing conditions was studied. Thermal stability and hardness were analyzed as a result of doping of Cu with Zr.

Chapter 2 : The effect of grain boundary relaxation and volume fraction on failure of nanocrystalline Ni-W under uniaxial compression [1]

2.1 Introduction

In this chapter, we use uniaxial microcompression testing to study the full flow curve and failure behavior of a nanocrystalline alloy, with a specific focus on understanding the importance of grain size and grain boundary relaxation state. Nanocrystalline Ni-W was chosen as a model system, since grain size can be easily manipulated during electrodeposition and this system has been studied extensively with nanoindentation [15,34,127]. To the authors' best knowledge, this is the first study to systematically explore uniaxial flow and failure in specimens with grain sizes from near 100 nm to below 10 nm. By studying this entire range, we are able to probe the effects of the entire gamut of deformation physics that control plastic deformation in nanocrystalline metals, spanning grain boundary dislocation mechanisms as well as grain boundary sliding and rotation. Strength, strain hardening, strain-to-failure, and failure mode are tabulated as a function of grain size and relaxation state. We show that reducing grain size and relaxing grain boundary structure can change the failure mode of a nanocrystalline metal from uniform plastic flow to shear localization. The localized plastic flow that we observe is reminiscent of shear banding in metallic glass, providing clear evidence of a connection between the deformation physics of nanocrystalline and amorphous metals.

[1] "Emergence of localized plasticity and failure through shear banding during microcompression of a nanocrystalline alloy", Khalajhedayati A, Rupert TJ. *Acta Materialia*, (2014) 65:326.

2.2 Materials and Methods

Nanocrystalline Ni-W alloy samples were created using pulsed electrodeposition following the work of Detor and Schuh [15]. In this system, the applied waveform is used to control the W content in the deposited film and, since the W exhibits a subtle tendency to segregate to the grain boundaries, the grain size can be controlled as well. Samples with mean grain sizes of 5, 15, and 90 nm were deposited onto 99% pure Ni substrates. In order to limit the impurities in our films, no organic grain refiner such as saccharine was used during electrodeposition. After deposition, samples were divided into two sets: as-deposited and relaxed. To relax the nonequilibrium grain boundary structure found in electrodeposited films, the specimens were annealed at 300°C for 1 hour and then water quenched, following prior work by Rupert et al. [128]. Such low temperature annealing treatments are aggressive enough to relax the grain boundaries, but gentle enough that grain growth is not induced. In light of recent computational [129] and experimental[130] research connecting grain boundary chemistry to strength, one could also ask if segregation of additional solutes to the grain boundaries occurs during annealing. Fortunately, previous microstructural evolution studies of nanocrystalline Ni-W [34] have shown that grain boundary relaxation always precedes other types of structural evolution (grain growth, precipitation of second phases, short-range ordering, or segregation), making Ni-W an ideal candidate for isolating the effects of nonequilibrium grain boundary structure. All of the samples were polished to submicron level using diamond suspension solutions. The final thicknesses of the films were at least 50 μm after fine polishing.

It is important to reiterate that grain size and composition are not independent in the Ni-W system. Films with higher W content will have finer grain sizes, which can complicate direct comparisons of strength measurements from different grain sizes. Rupert et al. [131] were able to

isolate and quantify the strengthening effect of solid solution W addition to nanocrystalline Ni when grain boundary dislocations control plasticity, but the authors are not aware of any study which has isolated solid solution strengthening when grain boundary sliding dominates. This means that any trends we observed in measure strength cannot be only attributed solely to grain size, nor can the relative contribution of grain size and composition be separated. However, Rupert et al. [131] also found that solid solution addition does not alter the dominant deformation physics. Since we are mainly interested in reporting on flow and failure characteristics in this paper, the three selected grain sizes can still be used to demonstrate mechanical behavior when the different deformation mechanisms are active.

TEM samples were prepared using the Focused Ion Beam (FIB) in-situ lift out technique [132] in a Quanta 3D FEG Dual Beam microscope. Lamellae with 10 μm widths and 5 μm heights were cut from each sample, and then thinned to create an electron-transparent specimen. A voltage of 5 kV was used during the final thinning step to minimize the thickness of the damaged layer created by the FIB. The same instrument was used to take SEM images of the pillar before and after deformation at 5-10 kV. Bright field TEM images were taken using a FEI/Philips CM-20 TEM microscope operating at 200 kV. Mean grain sizes were calculated by manually identifying and tracing individual grains, and then calculating the equivalent circular diameter for each before finding an average value. Fig. 2.1(a)-(c) shows the bright field TEM images of the as-deposited samples, while Fig. 2.1(d) presents cumulative distribution functions of grain size in each sample. Fig. 1 shows equiaxed grains with a narrow grain size distribution. X-ray diffraction (XRD) profiles were obtained using a Rigaku SmartLab X-ray Diffractometer with a Cu Kα radiation source operated at 40 kV and 44 mA. The XRD profiles were used to ensure that all of the

specimens were polycrystalline, fcc solid solutions and to estimate the average grain size using the Scherrer equation [133] .

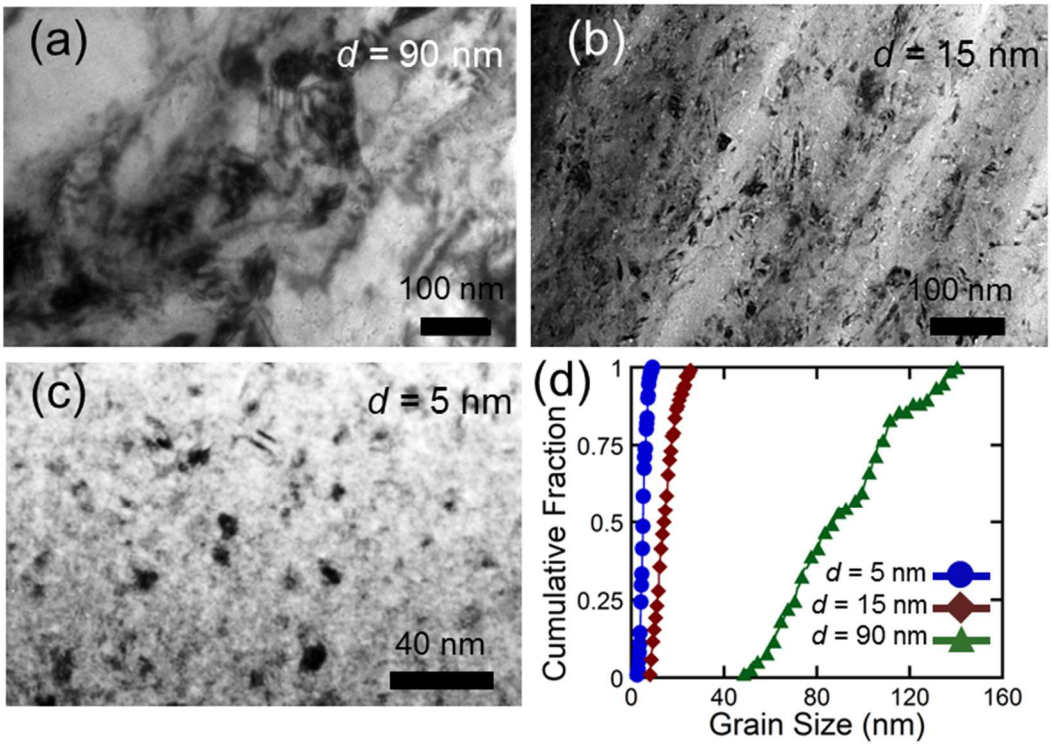

Figure 2.1 Bright field TEM images of nanocrystalline Ni-W samples with average grain sizes of (a) 90 nm, (b) 15 nm, and (c) 5 nm. Grain size measurements from each sample are presented in a cumulative distribution plot in (d).

Micropillars with average diameters of 7 ± 0.1 μm and average heights of 15.7 ± 0.3 μm were fabricated with automated lathe milling using the FIB, following the method of Uchic et al. [70]. The pillar aspect ratio (height/diameter) of 2.2 was chosen to follow microcompression testing guidelines developed by Zhang et al. [39], in order to avoid plastic buckling. The number of grains across the diameter of an average pillar is ~80 for the largest grain size (d = 90 nm) sample, which is more than enough to avoid external size effects on strength[134]. To make sure the indenter head does not hit the surrounding material around the pillar, a crater with a diameter of ~60 μm

was first milled using 7-15 nA around the prospective site. A circular fiducial mark was then milled on the center of the rough pillar with a 100 pA current, and a two-step lathe milling process was utilized to create the final pillar shape. First, a 1 nA current was used to mill the pillar close to its final shape, and then a final current of 100 pA was used to create a higher quality surface on the pillar and to reduce the damage layer from the FIB [135,136]. The lathe milling method allows taper-free pillars to be produced, as shown in Fig. 2.2, so a simple, uniform stress state can be applied to the nanocrystalline specimens.

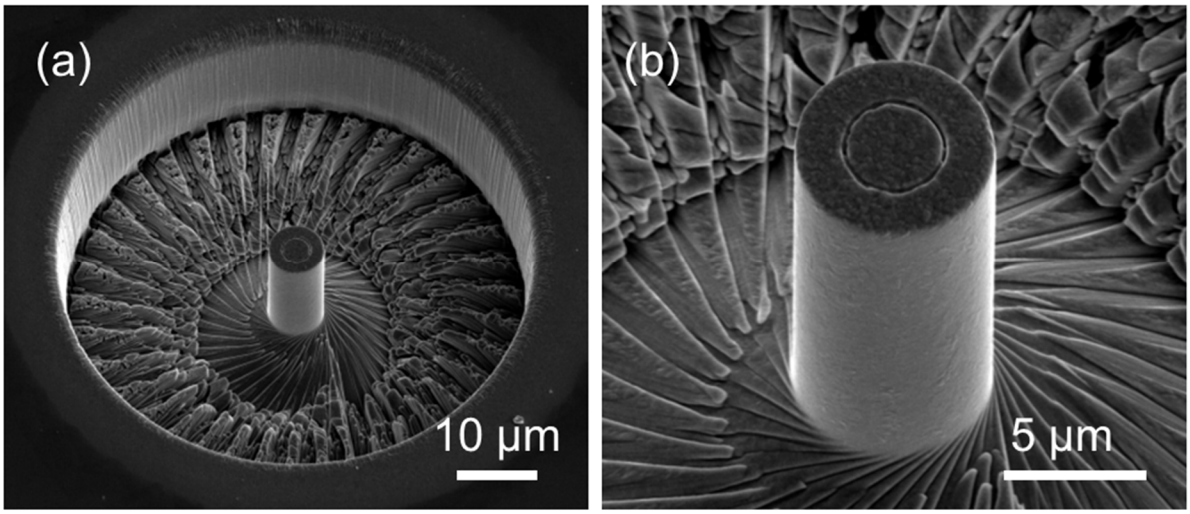

Figure 2.2 (a) An SEM image of a representative pillar that was used for uniaxial microcompression testing. (b) Magnified SEM image of the same pillar, showing the taper-free geometry.

An Agilent G200 nanoindenter was used to perform microcompression testing. The pillars were compressed using a Berkovich indenter tip truncated to have a flat, triangular surface at the end with an average side length of 31 μm. Although the instrument is an inherently force-controlled indenter, a feedback control loop was implemented so that the indenter nominally imposes a constant displacement rate. A constant displacement rate of 5 nm/s was applied, resulting in an engineering strain rate of 3.2×10^{-4} s^{-1} for the samples used here. For each grain

size and grain boundary relaxation state, at least five pillars were tested to ensure that the results were reproducible. When using microcompression testing, one must be careful to correct for the compliance of the base and minimize the misalignment between the indenter head and the pillar's top surface [137-139]. Sneddon's equation of rigid cylindrical flat punch displacement into an elastic half space was used to exclude the base compliance from our data[138]. Misalignment of the indenter decreases the measured modulus of the pillar by introducing a bending component to the deformation [137]. By carefully preparing flat, level samples and by following the best practices to align the pillars with the nanoindenter head [70], we are able to limit the misalignment to less than 1°, as calculated using the method of Schuster et al.[140].

Engineering stress-strain data was converted to true stress-stain data by assuming a uniform plastic deformation and conservation of the volume of pillar. Brandstetter et al. [141] and Vo et al.[142] both showed that the traditional 0.2% offset yield strength is not appropriate for nanocrystalline materials. Therefore, following the work of Brandstetter et al., yield stress was calculated based on a 0.7% yield strain offset. Some pillars were unloaded in order to calculate the modulus of the specimens while others were stopped at different plastic strains to study the deformation behavior in the SEM. To compare the results of microcompression with standard nanoindentation techniques, a Berkovich tip calibrated with standard fused silica was used for the measurement of hardness for each specimen. A constant indentation strain rate of 0.05 s^{-1} and at least 30 indentation experiments were used to find average hardness values.

2.3 Effect of grain size: As-deposited nanocrystalline Ni-W

We begin by exploring how grain size and, therefore, the dominant physical mechanism controlling plasticity affects the uniaxial deformation of nanocrystalline materials. The d = 5 nm

sample is small enough that grain boundary sliding and rotation is expected to completely control plastic deformation. The d = 90 nm is near the upper limit of the nanocrystalline regime and the deformation physics is expected to be dominated by dislocation activity originating at and being absorbed by the grain boundaries. The d = 15 nm is in the critical grain size range mentioned in the introduction where the shift between these two mechanisms occurs, so some combination of grain boundary dislocation plasticity and grain boundary sliding/rotation is expected here. Fig. 2.3 presents true stress-strain curves for as-deposited Ni-W specimens with different grain sizes.

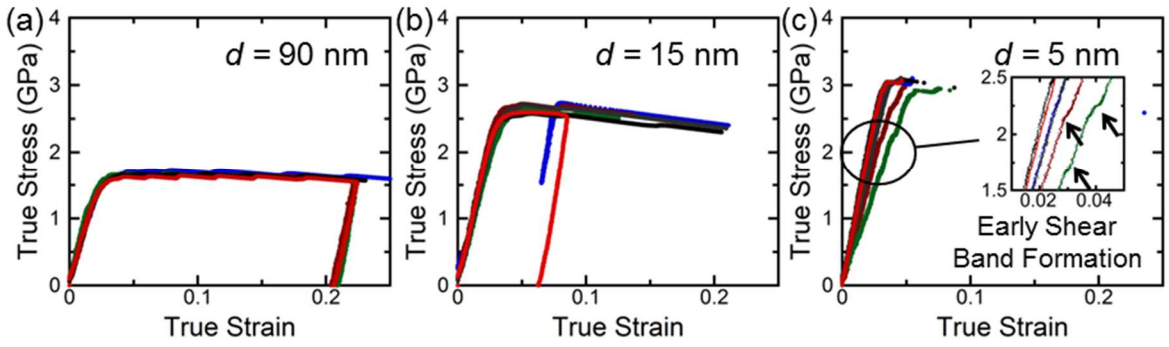

Figure 2.3 True compressive stress-strain curves from as-deposited Ni-W specimens with (a) d = 90 nm (b) d = 15 nm (c) d = 5 nm. At least 5 pillars were tested for each grain size, and some pillars were unloaded to calculate the stiffness of the pillar-substrate system. The inset to (c) shows that premature flow serrations can be found in a few of the curves from the 5 nm grain size samples.

The results for the d = 90 nm pillars, presented in Fig. 2.3(a), are discussed first. There is little variation between individual sample response and an average yield stress of 1.54 GPa is measured. Immediately after yielding, very limited strain hardening is observed over a small range of plastic strain. However, the vast majority of the plastic behavior is characterized by subtle strain softening. The decrease in flow stress with plastic strain is roughly linear, with a measured slope -0.45 GPa. The 90 nm grain size material lies near the upper limit of what is considered nanocrystalline (d < 100 nm), and a similar strain softening behavior has been previously observed in ultra-fine grained Ti [143] and Ni[144]. A possible reason for the observed decrease in strain

hardening ability compared to traditional metals is the reduction of dislocation sources inside the grain, and hence the reduction of hardening mechanisms expected from these activities. Fig. 2.3(a) also shows that the sample with d = 90 nm can sustain large plastic strains without any signs of failure, even after an applied strain of >25%. Fig. 2.4(a) shows an SEM image of a d = 90 nm pillar after 30% compressive strain. Plastic deformation was found to be uniform throughout the sample and no significant bending of the pillar was observed.

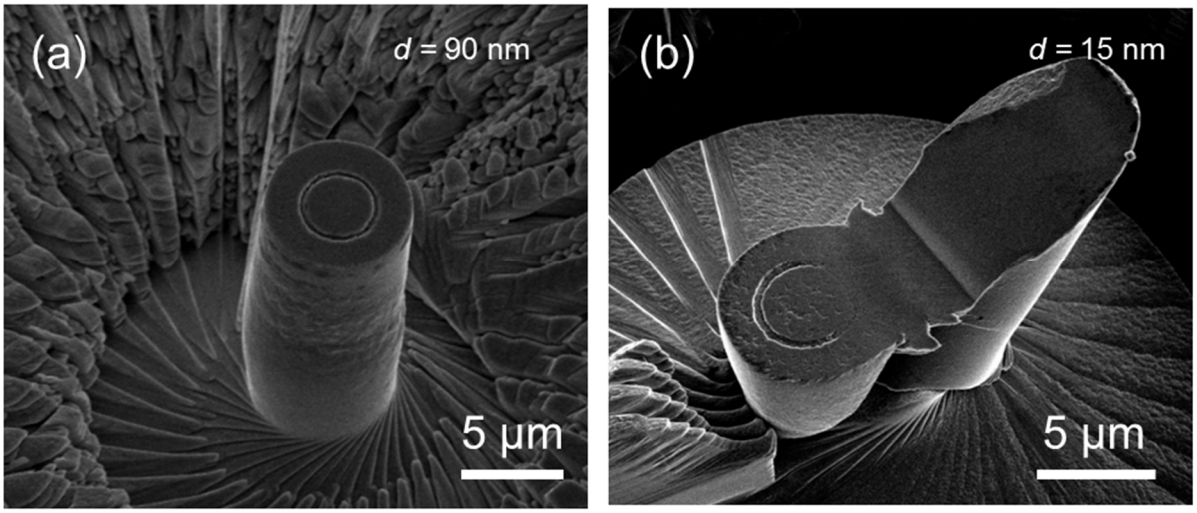

Figure 2.4 SEM images of as-deposited nanocrystalline Ni-W alloy pillars with (a) d = 90 nm and (b) d = 15 nm after uniaxial microcompression. The 90 nm grain size pillar shows a uniform plastic deformation while the 15 nm grain size pillar fails through strain localization.

Fig. 2.3(b) shows the true stress-strain data for the 15 nm grain size material, and several aspects of the stress-strain behavior have changed significantly with grain refinement. First, the average yield stress has significantly increased to 2.57 GPa. Such an increase in strength with grain refinement mimics reports that rely on nanoindentation results [128]. The strain hardening behavior during the initial stages of plastic deformation appears to be similar for the 90 nm and 15 nm grain sizes; a small amount of strain hardening is observed immediately after yielding but this behavior is short-lived. However, the strain softening at larger plastic strains is much more

pronounced and a linear strain softening slope of -1.95 GPa is measured for this grain size. Perhaps the most dramatic and unexpected difference in the mechanical behavior of the d = 15 nm samples is the observation of sudden failure at true strains of ~10-20%. Fig. 2.4(b) shows an SEM image of a d = 15 nm pillar after failure under compression. The pillar fails through the formation of a major shear band, and the top of the pillar shears off at an angle. Since the nanoindenter used in this study is inherently load controlled, this sudden downward movement of the indenter cannot be accommodated quickly enough in the feedback loop, causing a violent downward motion of the indenter tip that then pushes the damaged base off to the side. The grain size of this sample is close to the critical grain size where grain boundary sliding and rotation begin to carry an appreciable fraction of plastic strain [27,145], suggesting a causal link between the emergence of such collective grain boundary mechanisms and strain localization.

Finally, Fig. 2.3(c) presents the true stress-strain curves from the d = 5 nm specimens, showing even more unique mechanical behavior. These specimens demonstrate what appears to be elastic-perfectly plastic response with no discernible strain hardening and they then fail catastrophically after small plastic strains of only a few percent. The yield strength increases to 3.0 GPa, but the strain-to-failure has decreased significantly. No strain hardening or strain softening observed. While there appears to be increased scatter in the loading behavior of these samples, it is important to point out that four curves almost exactly overlap and are difficult to differentiate. The curves from the two samples that appear to be more compliant during loading (green and dark red in Fig. 2.3(c)) actually experience strain jumps that cause an apparent deviation from linear elasticity. These serrations are shown more clearly in the inset to Fig. 2.3(c). The formation and development of shear banding can be seen in SEM images taken after uniaxial compression. Fig. 2.5(a) shows a d = 5 nm pillar where the test was stopped immediately after

the initial deviation from linear elastic loading in the load-displacement curve, showing that several shear bands have formed along the length of the pillar. Fig. 2.5(b) is a pillar from the same grain size sample, but it was allowed to fail completely. Catastrophic failure occurred and secondary shear bands can be seen crossing the main slip steps. The details of the surface relief resulting from the shear banding are seen more clearly in Fig. 2.5(c), which presents an SEM image taken at higher magnification. We hypothesize that the premature flow serrations shown in the inset to Fig. 2.3(c) are shear bands which could not fully cross the sample width and lead to complete failure. As mentioned previously, it is expected that grain boundary sliding and rotation are the main carriers of plastic deformation at d = 5 nm.

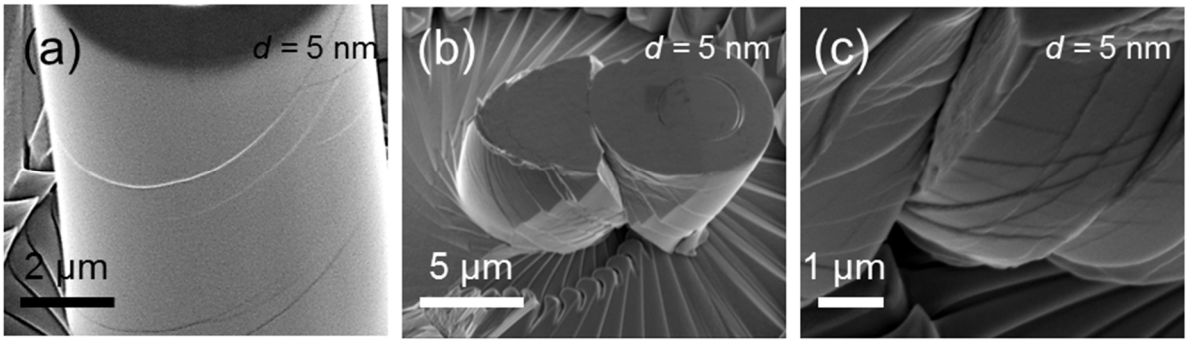

Figure 2.5 (a) SEM image showing the formation of shear bands immediately after initial yield in as-deposited nanocrystalline Ni-W with d = 5 nm. (b) SEM image of the same material after the complete failure showing multiple shear bands and catastrophic sample failure. (c) Magnified image of the same pillar showing intersecting shear bands in more detail.

Further insight into the failure behavior of our d = 5 and d = 15 nm samples can be found by looking more closely at the indenter displacement. Fig. 2.6(a) presents the average displacement rate versus time for representative examples taken from each grain size. Two major types of displacement bursts can be identified. For the two finest grain sizes, the average displacement rate shows a discontinuity corresponding to shear banding and catastrophic failure of the pillar. Since the system is inherently force controlled, the lack of resistance due to sample

failure leads to a rapidly increasing displacement rate. For the largest grain size, small strain bursts are observed, but the average displacement rate settles back to the constant target value. Here, dramatic changes in the slope of the stress-strain response give rise to the temporary strain bursts. For this sample, the change in the instantaneous sample stiffness is simply the result of a shift from elastic loading with a high slope to plastic flow with a much lower tangent modulus. After the yield point, while the indenter tries to keep the displacement rate constant, the feedback loop overcompensates and several strain bursts appear. The responses described above can also be seen in the raw displacement versus time data presented in Fig. 2.6(b). Shear banding leads to a rapid, uncontrollable failure of the pillar and the indenter then slams into the surface, while the behavior of the strain bursts in the d = 90 nm sample are much more controlled.

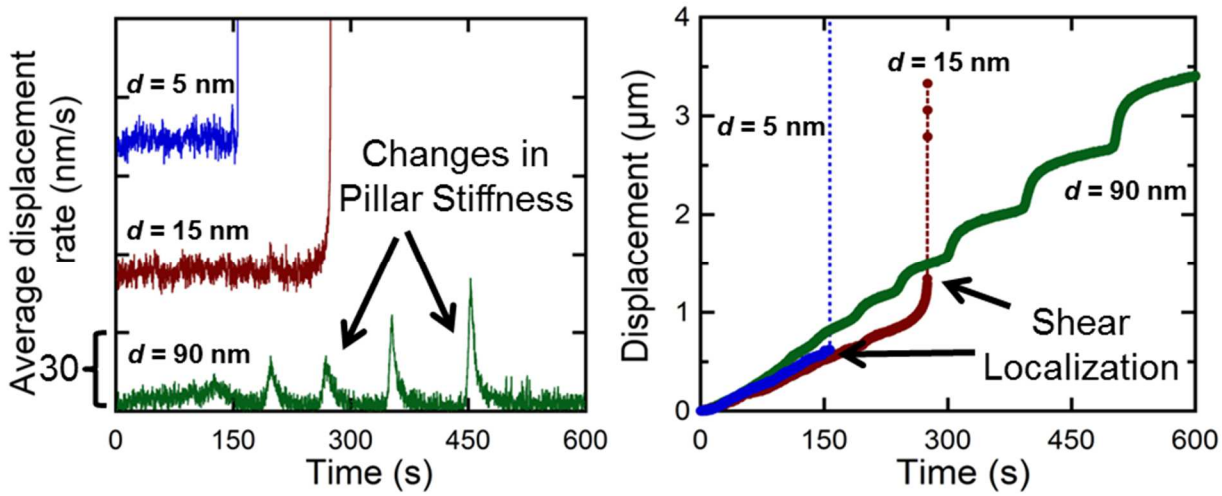

Figure 2.6 (a) Average displacement rate of the indenter head during microcompression testing for a representative pillar from each grain size material. The average displacement rate is 5 nm/s. Sudden strain burst are either due to shear localization or large changes to the stiffness of the pillar-substrate system. (b) The raw displacement versus time data also bears evidence of these strain bursts.

The strain localization described above for our 5 nm grain size is qualitatively similar to observations of shear banding by Trelewicz and Schuh [14] during nanoindentation studies of nanocrystalline Ni-W with d = 3 nm, although here we see more clearly how such shear banding

reduces strain-to-failure. Trelewicz and Schuh observed the formation of shear bands in the pile-up surrounding indentation impressions created with a cube corner indenter tip, suggesting that the finest nanocrystalline metals deform through mechanisms that are similar to those that control metallic glass plasticity. The fundamental unit of plasticity in a metallic glass is a shear transformation zone (STZ), or a small collection of atoms that undergoes an inelastic shear strain. When metallic glasses are deformed at temperatures well below their glass transition temperature, STZ activity leads to free volume accumulation along a distinct path, causing strain localization in the form of shear banding [145]. Schuster et al. [140,146] studied room temperature plastic deformation of a Pd-based metallic glass using a microcompression technique similar to the one used here. These authors observed features of metallic glass plasticity that are similar to the behavior of our d = 5 nm Ni-W sample: (1) serrated flow characterized by displacement bursts, (2) a lack of any appreciable strain hardening, and (3) failure through shear banding.

Insight into the similarity between the shear banding observed in the finest nanocrystalline metals and metallic glasses can be gained by understanding exactly how grain boundary rotation and sliding are accommodated. Lund et al. [46] used molecular statics simulations to study nanocrystalline plasticity and found that these collective motions result from the local rearrangement of small groups of atoms within the grain boundaries, a process similar to the STZs found in metallic glasses. One important difference is that, while any group of atoms can participate in such collective rearrangement in a metallic glass since there is no long range order, only the grain boundary atoms can participate in such motion in a nanocrystalline system. Since the crystalline grain interiors cannot participate in STZ-like motion, localization should still be limited by the connectivity of the interfacial network. However, recent molecular dynamics simulations from Rupert [56] have shown that a grain boundary percolation path of high strain can

be easily formed across a wire diameter if the grain size is small enough. Once this path is formed, strain intensifies in this region with progressive deformation due to the lack of hardening mechanisms.

While a natural comparison between amorphous plasticity and the collective grain boundary plasticity of the very finest nanocrystalline grain sizes can be made, a more complicated process is needed to describe why the 15 nm grain size would experience shear banding and strain localization since grain boundary dislocation plasticity is also important for this material. In fact, while Trelewicz and Schuh [14] saw shear banding during quasi-static nanoindentation of a 3 nm grain size, they did not observe such behavior for larger grain sizes. To the best of our knowledge, the results presented here are the first to show shear banding in a nanocrystalline fcc metal with a grain size as large as 15 nm. With a grain size this large, a shear band is unlikely to form entirely through a grain boundary path, but rather through a combination of boundary and dislocation mechanisms. Hasnaoui et al.[147] provided the first evidence of such a mechanism, when their molecular dynamics simulations of nanocrystalline Ni showed the formation of common shear planes during uniaxial deformation at elevated temperatures. They suggested that this shear plane formation was a cooperative process that included several grains and could involve three types of mechanisms: migration of grain boundaries, coalescence of grains with low angle grain boundaries, and intragranular slip that provides continuation of a shear plane encountering a triple junction. Sansoz and Dupont [148] also observed the initial formation of a shear plane during molecular statics simulations of nanoindentation in nanocrystalline Al. Finally, Rupert [56] used molecular dynamics simulations of nanocrystalline Ni to show more clearly how a localization path formed by grain boundary and dislocation mechanisms can thicken and intensify to form a fully developed shear band. This author observed successive partial dislocation emission, leading

to deformation twins which extended the localization path through the grain interior. Rupert also observed that, while localization paths along grain boundaries form quickly during initial stages of plasticity, grains that must be sheared with grain boundary dislocations can limit shear band formation. This likely explains why the 15 nm grain size sample experiences a moderate level of plastic strain before shear banding. Until dislocation mechanisms can traverse enough grains to create a percolation path across the sample width, catastrophic strain localization cannot commence.

2.4 Effect of grain boundary state: Relaxed nanocrystalline Ni-W

With insight into the importance of grain size, we next move our attention to understanding how grain boundary state, specifically the relaxation of nonequilibrium interfacial structure, affects the mechanical properties of nanocrystalline alloys. XRD and TEM of the annealed samples showed that the low temperature annealing treatment used for relaxation did not change the grain size. We began first by looking at the largest grain size sample. Figure 2.7(a) shows the true compressive stress-strain curves for the d = 90 nm samples. The yield strength of the material has slightly increased to 1.7 GPa, or 0.15 GPa more than the as-deposited case. We again observe two different types of behavior in the true stress-strain curve after the yield point. First, a very limited amount of strain hardening is found immediately after yielding over a range of small plastic strains. This is followed by a region of roughly linear softening behavior, but this behavior has become slightly more pronounced and was measured to have a slope of -0.63 GPa. Hence, even large nanocrystalline grain sizes become more prone to strain softening after grain boundary relaxation. Like its as-deposited counterpart, this material can still withstand large plastic strains of up to 25%

without failing. SEM images of micropillars after deformation (not shown here) demonstrate that the relaxed, d = 90 nm grain size sample still experiences homogeneous plastic flow.

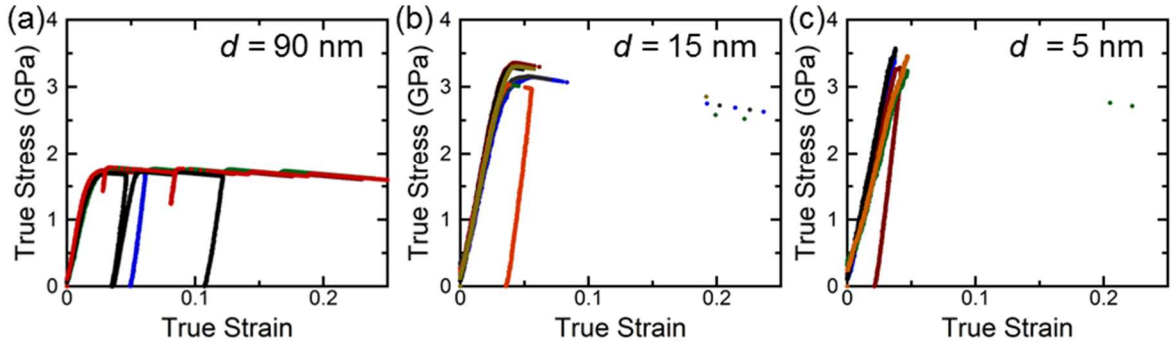

Figure 2.7 True compressive stress-strain curves from relaxed Ni-W samples with (a) d = 90 nm (b) d = 15 nm (c) d = 5 nm. At least 5 pillars were tested for each grain size, and some pillars were unloaded to calculate the stiffness of the pillar-substrate system.

Fig. 2.7(b) shows the true stress-strain behavior of the d = 15 nm relaxed samples. The average yield stress of the material increased to 3.15 GPa, or increased by 0.57 GPa from the as-deposited state. Hence, grain boundary relaxation has a larger strengthening effect as grain size is reduced. Rupert et al. [128] suggested that relaxation reduces the density of grain boundary sources for dislocation emission or nucleation, making it harder to initiate plastic flow. Alternatively, Van Swygenhoven et al. [22]proposed that dislocation pinning at grain boundary sites could determine the strength of nanocrystalline metals, so it is possible that the local structure of the grain boundary influences this process as well. In this case, a more ordered (i.e., relaxed) grain boundary would have fewer high energy sites where local stress variations could aid the applied stress and keep the dislocation moving, again meaning a higher applied stress is needed to initiate macroscopic plasticity in the sample. The maximum flow stress and yield stress values do not differ more than the error in the measured data, indicating that even the limited strain hardening ability seen in the as-deposited sample has vanished. The value of the strain softening slope has decreased to -3.2 GPa for the relaxed d = 15 nm sample. Interestingly, the strain-to-failure of the

relaxed sample decreased significantly compared to the as-deposited sample, with all of the pillars failing between 5% and 8% strain through shear banding. Thus, both d = 90 nm and d = 15 nm samples have a higher tendency to strain soften after relaxation, but the relaxed d = 15 nm sample also experiences catastrophic strain localization at smaller plastic strains when compared to the as-deposited state. Fig. 2.8(a) presents an SEM image of a d = 15 nm relaxed pillar right as it starts to fail, showing the formation of a major shear band.

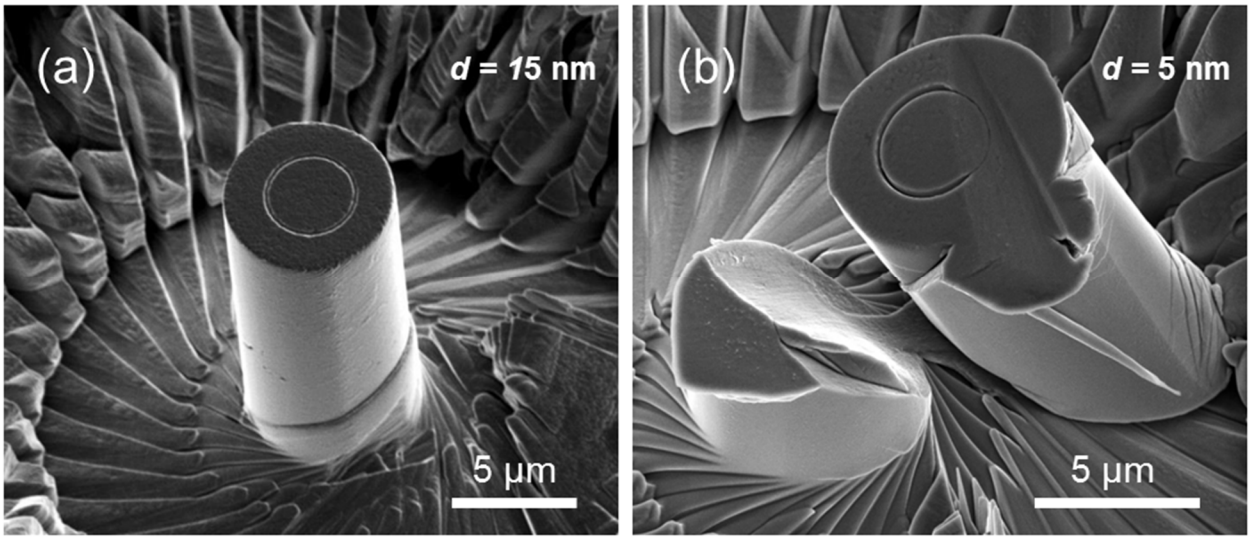

Figure 2.8 SEM images of (a) 15 nm (b) 5 nm relaxed samples after the microcompression test. After the complete failure of the pillar, the indenter head pushes the pillar to the side, and the impression of the indenter tip is visible in (b).

Fig. 2.7(c) shows the true stress-strain behavior of the d = 5 nm relaxed specimens. For this group of specimens, no appreciable plastic strain was observed before catastrophic shear banding occurred. Without measurable plastic strain, we instead report the maximum stress as our yield strength here. The pillars fail as soon as they reach a critical stress of 3.4 GPa, meaning strength has increased by 0.4 GPa over the as-deposited condition. While this is appreciable strengthening, it is less than was observed for the 15 nm grain size, suggesting that relaxation has the strongest effect on strength at an intermediate grain size. Nanoindentation work from Rupert

et al. [35]reported a trend that was qualitatively similar, but found that the largest strengthening was observed at d = 6 nm, near our finest grain size sample here. This apparent discrepancy can be addressed by directly comparing microcompression and nanoindentation measurements for the samples tested in this study, which we will do shortly. Fig. 2.8(b) shows a d = 5 nm relaxed pillar after the completion of the compression test, where it is clear that the pillar failed with a formation of a major shear band. The indenter head continued to travel downward for a few seconds after failure, causing the impression of the tip which is visible in the pillar top.

Fig. 2.9(a) shows our yield stress data plotted as a function of grain size for as-deposited and relaxed Ni-W, while Fig. 2.9(b) presents nanoindentation hardness measurements taken from the same samples. In each case, the strengthening we observed with grain refinement does not follow a strict $d^{-1/2}$ scaling, signifying a deviation from Hall-Petch behavior. While compositional changes should also affect this data, the increase in W content with decreasing grain size would lead to strengthening, so it cannot be to blame for the decreased slope observed in Fig. 2.9. Both sets of measurements show that relaxation of nonequilibrium grain boundaries leads to significant strengthening, but the maximum effect occurs at different grain sizes for each type of measurement. While yield stress demonstrates the largest improvement at d = 15 nm, hardness increases the most with relaxation for the 5 nm grain size. However, we suggest that this is simply an artifact associated with the nanoindentation technique. The stress-strain curves from the relaxed d = 5 nm sample show that this material cannot accommodate appreciable plastic strain before failing catastrophically through shear banding. However, during nanoindentation, either the confining pressure underneath the indenter or the geometry of the indenter tip can suppress such localization, leading to an anomalously large measurement of the sample's strength. This concept can be seen more clearly in Fig. 2.10, where nanoindentation hardness is plotted versus yield stress

measurements. For all of our as-deposited samples and the relaxed samples with larger grain sizes (i.e., the specimens that can sustain at least a few percent plastic strain before failure), there is a linear correlation between hardness and yield stress. This is the conceptual idea behind hardness as a quick and convenient measure of strength: the two quantities should be related in a known manner. However, the relaxed d = 5 nm sample (i.e., where there is no measurable plastic strain before failure) clearly deviates from this behavior, with a strength that is much lower than what would be predicted from its hardness. For materials where strain localization occurs before stable plastic flow can be developed, such as our smallest nanocrystalline grain size in the relaxed state, hardness trends do not necessarily mimic trends in true strength measurements.

An important observation is that relaxation of nanocrystalline grain boundaries makes the 5 and 15 nm grain sizes more susceptible to shear banding, reducing the strain-to-failure in both cases. For d = 5 nm, a comparison with metallic glass physics can again be useful. Both experiments [149] and simulations [150] have shown that metallic glasses with increased short range order deform through larger, more conspicuous shear bands. A highly disordered metallic glass has many sites with elevated local stresses, which can cause small shear bands to nucleate in different regions of the sample and give a macroscopic deformation that is more homogeneous. When there are few local variations in atomic stress due to structural disorder, the operation of an STZ provides the largest local stress fluctuation and strongly biases successive nearby STZ operation, leading to large catastrophic shear bands. If deformation is accommodated entirely through grain boundary processes in the 5 nm grain size sample and these boundaries locally deform in a manner that is similar to a glass, a relaxed, more ordered grain boundary structure would also result in increased strain localization. For the 15 nm grain size, increased strain localization likely results from a superposition of the effect of relaxation on grain boundary

processes and its effect on grain boundary dislocation mechanisms. As mentioned in the Introduction, grain boundaries not only act as sources of dislocations, but also as sinks where the defects are reabsorbed into the opposite boundary. A more ordered grain boundary, with fewer local stress variations and less free volume, should be a less efficient sink for such absorption than the disordered boundary found in the as-deposited materials. Without efficient reabsorption of the first dislocation that traverses the grain, a bias for successive nearby dislocation emission exists within the crystallite, making it easier for the localization path to be created across the grain interior.

The results described here highlight the fact that grain boundary state is very important for nanocrystalline metals. The grain size of a nanocrystalline metal is often thought of as the structural feature which controls mechanical properties, but we show here that the plastic flow and failure of nanocrystalline Ni-W samples with the same grain sizes can be dramatically different depending on their grain boundary relaxation state. A more ordered boundary structure gives nanocrystalline metals increased strength, but also leads to more pronounced strain softening during the later stages of plastic deformation. In addition, for our smallest grain size of 5 nm and 15 nm, relaxation of nonequilibrium grain boundaries reduces strain-to-failure and promotes shear banding. While an ordered boundary structure improves strength, this appears to come at the expense of toughness.

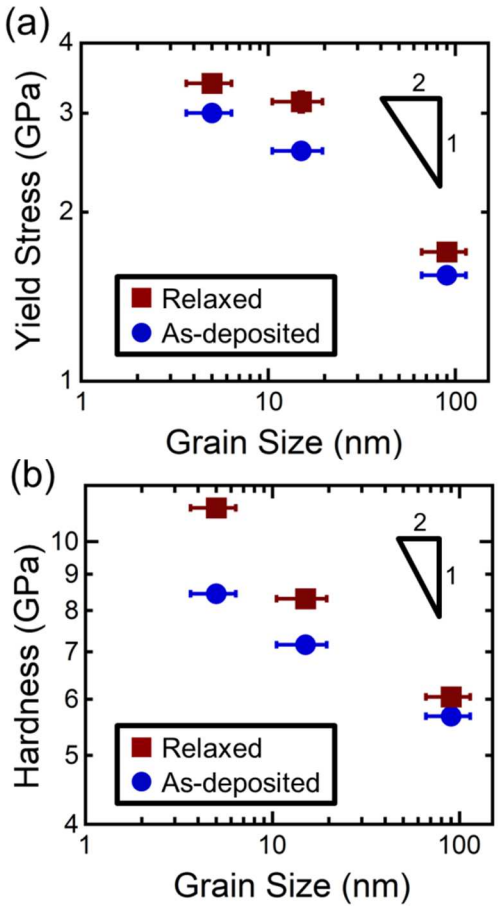

Figure 2.9 Mechanical property measurements for nanocrystalline Ni-W samples, plotted as a function of grain size. Yield stress is shown in (a), while hardness measurements are presented in (b). For these samples, relaxation has a maximum effect on yield stress for d = 15 nm, while hardness shows the largest increase for d = 5 nm.

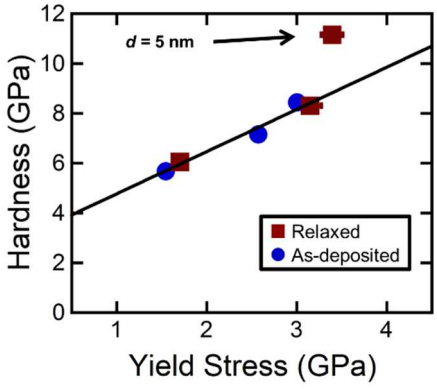

Figure 2.10 Hardness plotted against yield stress for both as-deposited and relaxed nanocrystalline Ni-W samples. The straight line is fitted to the first five data points. The relaxed 5 nm grain size sample does not fall on this line, suggesting that hardness and yield stress cannot be directly related for nanocrystalline samples that fail before developing appreciable plastic strain.

Finally, since grain boundary state has been shown to be important, it is likely necessary to differentiate between nanocrystalline materials created by different processing routes when looking for trends in literature data. Early studies of nanocrystalline materials often accessed a variety of grain sizes by taking a very fine grained sample and annealing it to cause thermal grain growth (see, e.g.,[151,152]). However, such annealing should also relax nonequilibrium grain boundary structure, making it difficult to compare property measurements from, for example, a 40 nm grain size sample that was created by annealing with those from an as-deposited 40 nm sample. Grain boundary state should also be important when comparing deposited nanocrystalline materials with those created by severe plastic deformation. Processing techniques such as ball milling, high pressure torsion (HPT), and equal channel angular pressing (ECAP) create nanostructured metals by adding a great deal of strain energy to the material in order to drive refinement. Materials created by these methods likely have grain boundary structures which are even further from equilibrium than deposited films.

2.5 Conclusions

Microcompression testing has been used to study the effects of grain size and grain boundary relaxation state on plastic flow and failure of nanocrystalline Ni-W. To our knowledge, this is the first study to systematically probe the uniaxial stress-strain response of nanocrystalline metals with microcompression over a range of grain sizes that spans the entire range of possible deformation mechanisms. Such a technique is extremely advantageous for probing nanostructured materials, as it avoids the common geometric and processing artifacts which plague standard uniaxial testing on these materials. The results presented here allow the following conclusions to be drawn:

- Grain refinement from d = 90 nm to d = 5 nm causes yield strength to nearly double, increasing from 1.54 GPa to 3.0 GPa, respectively, although chemistry also plays a role in this strengthening since W content increases from ~3% to ~20%.
- Our largest grain size, d = 90 nm, could be compressed to >25% true strain without failing. Subtle strain softening was observed, but deformation remained homogenous in nature throughout the compression experiments.
- The intermediate grain size of 15 nm, where a combination of dislocation plasticity and grain boundary plasticity controls deformation, was much stronger as a result of its finer grain structure, but experienced pronounced strain softening and then sudden failure through shear banding at applied true strains of 10-20%.
- Our finest grain size, d = 5 nm, exhibits elastic-perfectly plastic deformation with no apparent strain hardening or softening after yield. After plastic strains of only a few percent, strain localization occurs and these specimens fail through shear banding that resembles the behavior of metallic glasses.
- Relaxation of nonequilibrium grain structure strengthens nanocrystalline metals, but makes our two finest grain sizes more susceptible to strain localization. For d = 15 nm, the strain-to-failure is reduced to 5-8%, while the 5 nm grain size sample shows no appreciable plastic strain before shear banding causes failure.
- In samples where strain localization leads to failure, there may not be a direct correlation between nanoindentation hardness and yield stress measurements. For our relaxed d = 5 nm samples, hardness was artificially high due to the suppression of shear banding under the indenter.

Taken as a whole, the results presented here show that catastrophic strain localization is an issue for nanocrystalline metals with small grain sizes. The grain sizes less than 20 nm which are strongest are also the most likely to fail at small applied strains. This strain localization is also a function of grain boundary state, with an ordered interfacial structure promoting shear banding and failure that resembles metallic glass behavior. While a relaxed grain boundary state increases strength, it is detrimental to strain-to-failure.

Chapter 3 : Grain coarsening in a thermally-stable nanoscale grain structures by strain localization[2]

3.1 Introduction

In Chapter 2, shear banding was found in grain sizes as large as 15 nm, suggesting that catastrophic strain localization can be a more common problem for nanocrystalline materials than previously thought. Recent studies showed that plasticity drives grain growth in many nanocrystalline metals, although this is expected to be mitigated in alloys [42]. However, shear banding is an extreme event where local plastic strain reaches very high levels, so it is possible that evolution occurs. Understanding such behavior is important for the study of grain size stability since it can show the limit of grain boundary doping methods. In this chapter, we investigate the microstructure of nanocrystalline Ni-W with d = 5 nm before and after catastrophic shear banding. Ni-W was chosen as a model system for this study because, due to the subtle tendency for segregation of W to the grain boundaries (grain boundary excesses of 4-8 at.% W over the grain interior composition), nanocrystalline coatings that are resistant to thermal grain growth up to ~500 °C (i.e., ~45% of the melting temperature) can be created [34]. This allows us to observe how severe strain localization occurs in an alloy system which is typically stable. A combination of microcompression and nanoindentation were used to induce shear banding, since these two techniques allow us to explore different stress states and plastic strain distributions. During microcompression, nearly all plastic strain is limited to the shear bands, while in nanoindentation there is a combination of shear banding and homogeneous plasticity. We find that intense strain localization inside of shear bands can drive obvious coarsening and texturing, while homogeneous

[2] Disruption of Thermally-Stable Nanoscale Grain Structures by Strain Localization
Khalajhedayati A, Rupert TJ. *Scientific Reports* (2015) 5:10663.

plasticity (or low plastic strain) leaves the grain structure unchanged. These results suggest that even thermally-stable nanocrystalline grain structures can coarsen under mechanical loading, but extreme conditions are required.

3.2 Materials and methods

A Ni-based alloy with 23 at.% W and an average grain size of 5 nm was prepared using the pulsed electrodeposition method of Detor and Schuh [15]. Although the equilibrium Ni-W phase diagram predicts a mixture of FCC Ni(W) solid solution and Ni_4W for this alloy composition, our films were comprised only of FCC Ni(W) solid solution, in line with previous observations of similar nanocrystalline Ni-W alloys [34,127]. Cylindrical micropillars with average diameters of 7 μm and lengths of 16 μm were fabricated using a lathe milling Focused Ion Beam (FIB) technique [153]. An Agilent G200 nanoindenter with a flat triangular tip was used to compress the pillars at a constant displacement rate of 5 nm/s. For our nanoindentation studies, a cube corner tip was used to make the observation of the deformed region around the indent easier, as significant pile-up can occur with this tip geometry [35]. Previous studies [154,155] have shown that shear banding during nanoindentation is strain rate dependent and that a higher strain rate shifts the plasticity toward more homogenous plasticity. For this reason, a relatively low strain rate of 0.05 s^{-1} was chosen to promote shear banding. For nanoindentation, the as-deposited sample was annealed at 300°C for 1 hour to relax the grain boundary structure to a lower energy level [35] since relaxation has been shown to increase the propensity for shear localization. TEM characterization was performed with a Philips-FEI CM-20 operated at 200 kV and equipped with a Gatan digital camera. Site-specific TEM samples were prepared using a FIB in-situ lift out technique [156] in a FEI Quanta 3D field emission gun (FEG) dual beam microscope. The TEM

lamellas were polished with a 5 kV Ga^+ ion beam to minimize ion beam damage to the sample. All SEM imaging was carried out at 5 kV in the same dual beam SEM/FIB.

3.3 Results

3.3.1 Microcompression of nanocrystalline Ni-W with d = 5 nm

Fig. 3.1(a) shows a SEM image of a micropillar of nanocrystalline Ni-W after microcompression testing. The pillar experienced a large strain burst and failed catastrophically. The micropillar has a number of major surface steps corresponding to primary shear bands (red arrow), with a high density of thinner, secondary shear bands that crisscross each other also observed (white arrow). Fig. 3.1(b) shows the corresponding true stress-strain curve for this pillar. Several strain bursts are observed in this curve, with two examples denoted by black arrows. The pillar compresses elastically for the majority of this test, with deviations from this behavior only coming in the form of strain bursts. Such a response is a sign that plasticity is dominated by shear banding for this testing methodology, not homogeneous plastic deformation, as a smooth microplastic region of the stress-strain curve would be found in that case.

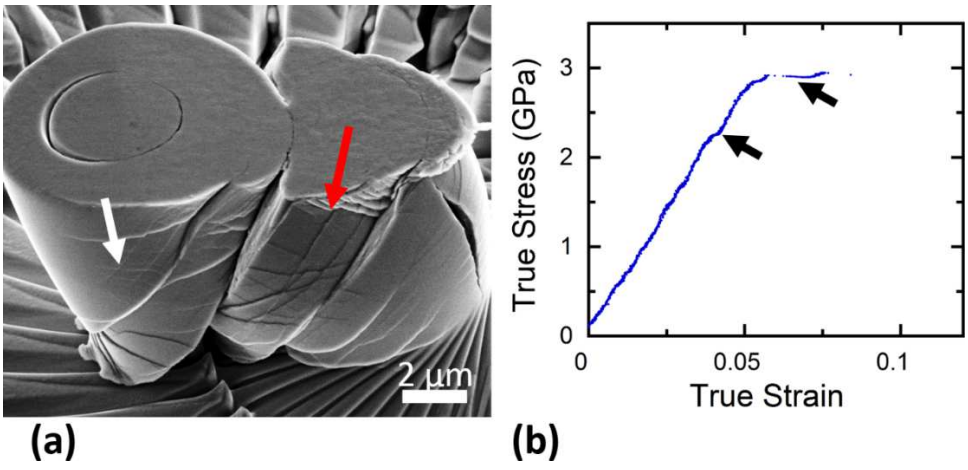

Figure 3.1 Microcompression of nanocrystalline Ni-W with an average grain size of 5 nm: (a) SEM image of a micropillar after deformation, taken at 52° tilt. Several slips steps from primary shear bands are observed on the surface, in addition to smaller, secondary shear bands criss-crossing in between. (b) True stress-strain curve of the corresponding pillar showing several displacement bursts during micorcompression.

Fig. 3.2(a) presents a bright field TEM image of shear bands, one primary and one secondary, inside of the micropillar. Shear bands with thicknesses from 10 to 270 nm were observed, and most of the shear bands are in the lower end of this range. The thickest bands corresponded to locations where large, primary shear bands were found on the surface, with an example found in the center of Fig 3.2(a) and denoted by dashed white lines. A smaller, secondary shear band is found in the lower right of the same Figure outlined by solid white lines. This Figure also shows that grain growth is limited to the shear bands. Fig. 3.2(b) shows a magnified view of the microstructure inside of the major shear band, with the largest grains in this region being ~17 nm in diameter. Fig. 3.2(c) shows the cumulative distribution function of grain size inside and outside the shear bands, as compared to the as-deposited microstructure. The average grain size inside the shear bands has been increased by more than 50%, from 5 nm to about 8 nm, and the distribution of grain sizes has widened. The grain size outside of the shear bands, in the region which only experienced elastic deformation, has not changed and the grain size distribution follows the same pattern as the initial microstructure. An example of the network of shear bands found inside the sample is shown in Fig. 3.2(d). Part of a primary shear band can be seen in the top left of the image, with many secondary shear bands coming out in directions downward and to the right. The crisscross pattern seen on the surface of the pillar in the regions with a high density of secondary shear bands has a similar appearance. All shear bands observed in microcompression samples appeared as long, straight lines. To the best of our knowledge, this is the first time that the microstructure inside of a shear band has been observed experimentally in a nanocrystalline FCC metal.

Fig. 3.3(a) presents a selected area electron diffraction pattern taken from one of the major shear bands. The segmented ring pattern is indicative of a textured microstructure and the specific pattern observed here is a pure shear texture often observed in FCC metals, consisting of {100} {011}, {111} <112>, and {111} <110> components[157]. Similar patterns and textures were found along the entire length of the shear band, confirming that this observation was a general one. A dark field image, taken by putting the smallest objective aperture on one of the segmented rings, is shown in Fig 3.3(b). Grains that are oriented in the same diffraction condition are visible as bright spots in this image, with the high density of bright regions inside the shear band indicating the existence of a preferred orientation. Outside the shear band, the distribution of dark and bright spots is random since there is no texture. Fig. 3.3(c) shows a higher magnification dark field TEM image of the microstructure inside the same shear band, where a cluster of grains with the same orientation can be seen.

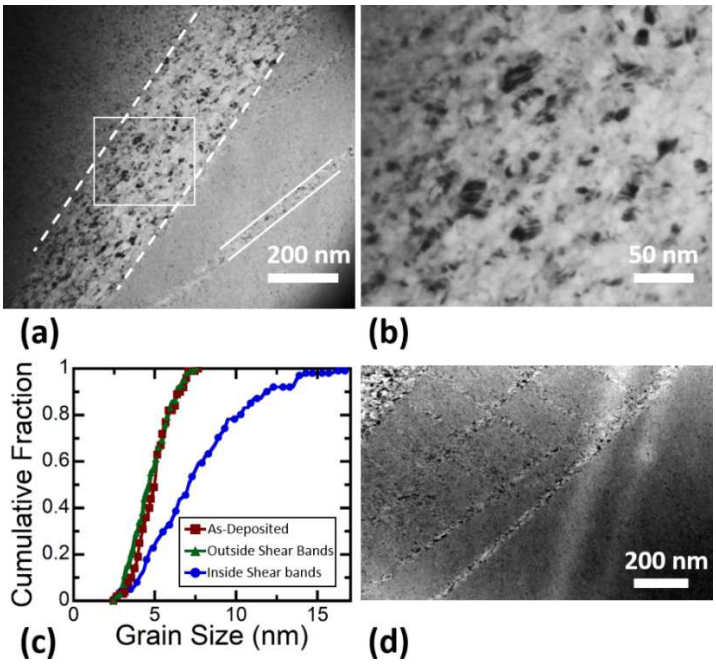

Figure 3.2 Microstructure of the shear bands inside the pillar: (a) TEM image of a primary shear band outlined with dashed white lines and secondary shear band outlined with solid white lines. (b) Magnified view of the area denoted by the white box in (a) showing grain growth inside of the shear band. (c) Cumulative distribution function of grain size from grains inside and outside the shear bands, as well as the as-deposited sample. (d) TEM image showing an example of the shear band network inside of the pillar.

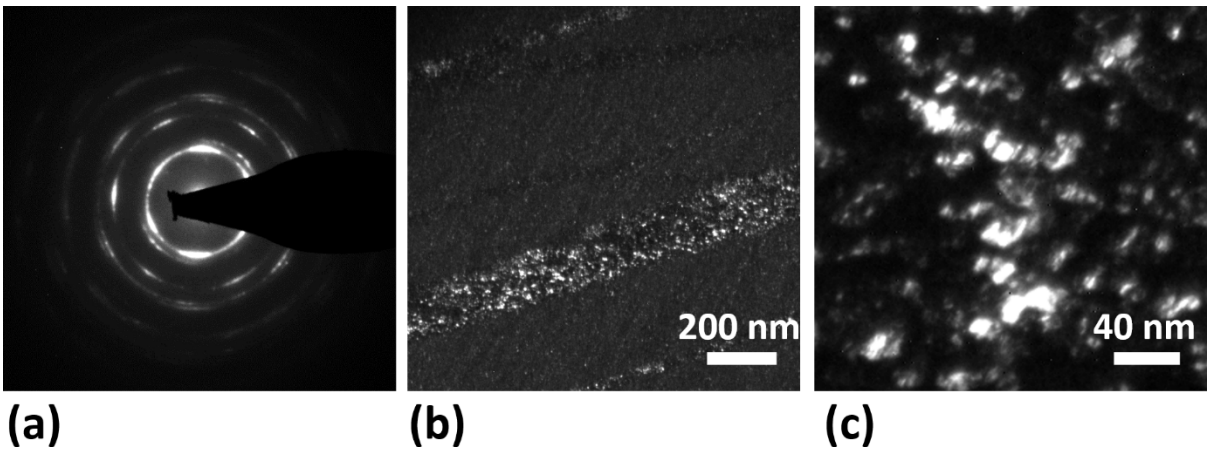

Figure 3.3 Pure shear texture in the shear band: (a) Selected area diffraction pattern taken from a thick shear band. (b) Corresponding dark field TEM image of the shear band, showing many grains with the preferred texture within the shear bands. (c) Magnified view of the microstructure inside the shear band, showing a cluster of grains with similar orientations.

3.3.2 Nanoindentation of nanocrystalline Ni-W with d = 5 nm

Nanoindentation imposes a strong strain gradient and a complex stress field under the indenter tip [158]. Fig. 3.4(a) shows a nanoindentation made with a cube corner tip. The tip geometry literally resembles the corner of a cube and has a very sharp end, therefore it confines the plasticity to a small volume of material under the tip and often induces pile-up formation around the indents. The large shear steps that are observed in the pile-up surrounding the nanoindentation site in this Figure indicate that inhomogeneous plasticity and flow localization occurred [128]. Fig. 3.4(b) shows the corresponding load-displacement curve from this nanoindentation experiment. The nanoindenter is inherently force-controlled, so any shear banding events appear as a burst in displacement [153]. Two such displacement bursts are magnified in Fig. 3.4(b), each with a magnitude of ~10-15 nm.

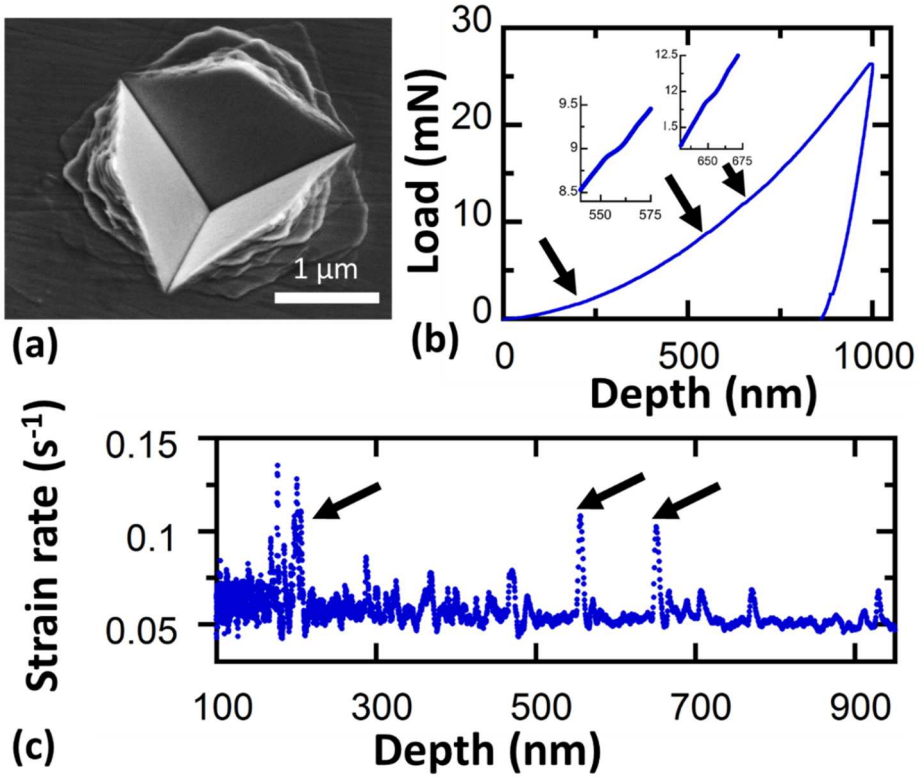

Figure 3.4 Nanoindentation of nanocrystalline Ni-W with average grain size of 5 nm using a cube corner tip: (a) SEM image of one of the indents taken at 30° tilt. (b) Corresponding nanoindentation load-displacement curve, with several strain bursts denoted by black arrows. (c) Average strain rate versus indentation depth for the same loading curve, showing jumps in the instantaneous strain rate during loading which match up with the bursts denoted in (b).

An indentation study by Wright et al. on Zr based metallic glass showed that flow serration during loading is due to formation of shear bands under the indenter tip [159]. Although these serrations clearly exist in our experiment, careful examination shows that the loading curve is mostly smooth and only a few displacement bursts are observed. Another way to visualize the number of the shear band events is to plot the instantaneous strain rate versus indentation depth, as shown in Fig 3.4(c). Since the indentation test was supposed to be at a constant strain rate under perfect conditions (i.e., without any displacement bursts), the strain rate data should follow a straight line. However, the displacement bursts that occur in this experiment lead to local peaks in the instantaneous strain rate. The peaks that are pointed out here correspond to the same

displacement bursts that were highlighted in the load-displacement curve, and less than 10 of these peaks were observed. The deformation is a combination of homogenous plasticity (smooth load-displacement curve) and strain localization (displacement bursts). Schuh and Nieh [154] observed similar combinations of deformation modes in Pd- and Zr-based metallic glasses.

Fig. 3.5(a) shows cross-sectional TEM images of the nanoindentation observed in the previous Figure. The area under the indenter tip denoted by a dashed box is magnified in Fig. 3.5(b). The shear bands have a curved shape and extend deep under the indenter tip, in contrast to the straight shear bands found after microcompression. Measurement of the shear bands after indentation showed that the thickness varies from 8 nm to 32 nm. The area denoted with a solid white box is magnified in Fig. 3.5(c). Grain growth was observed in all the shear bands but, due to limited thickness of the shear bands in nanoindentation, selected area diffraction patterns could not give conclusive results about the texture. Fig. 3.5(c) shows the shear bands that extend to the pile-up surrounding the indentation site. These bands terminate at the surface and result in slip steps there, as previously shown from a different perspective in Fig 3.4(a). Fig. 3.6(a) shows an example of the complex, entangled pattern of curved shear bands formed under the indent. Fig. 3.6(b) presents the cumulative distribution function of grain size for the sample which was indented. The grain size distribution outside of the shear bands remained the same as the as-deposited specimen. However, the grain size inside the shear bands is much larger, with d increasing from 5 nm to 8 nm and a distribution which ranged from 3-17 nm.

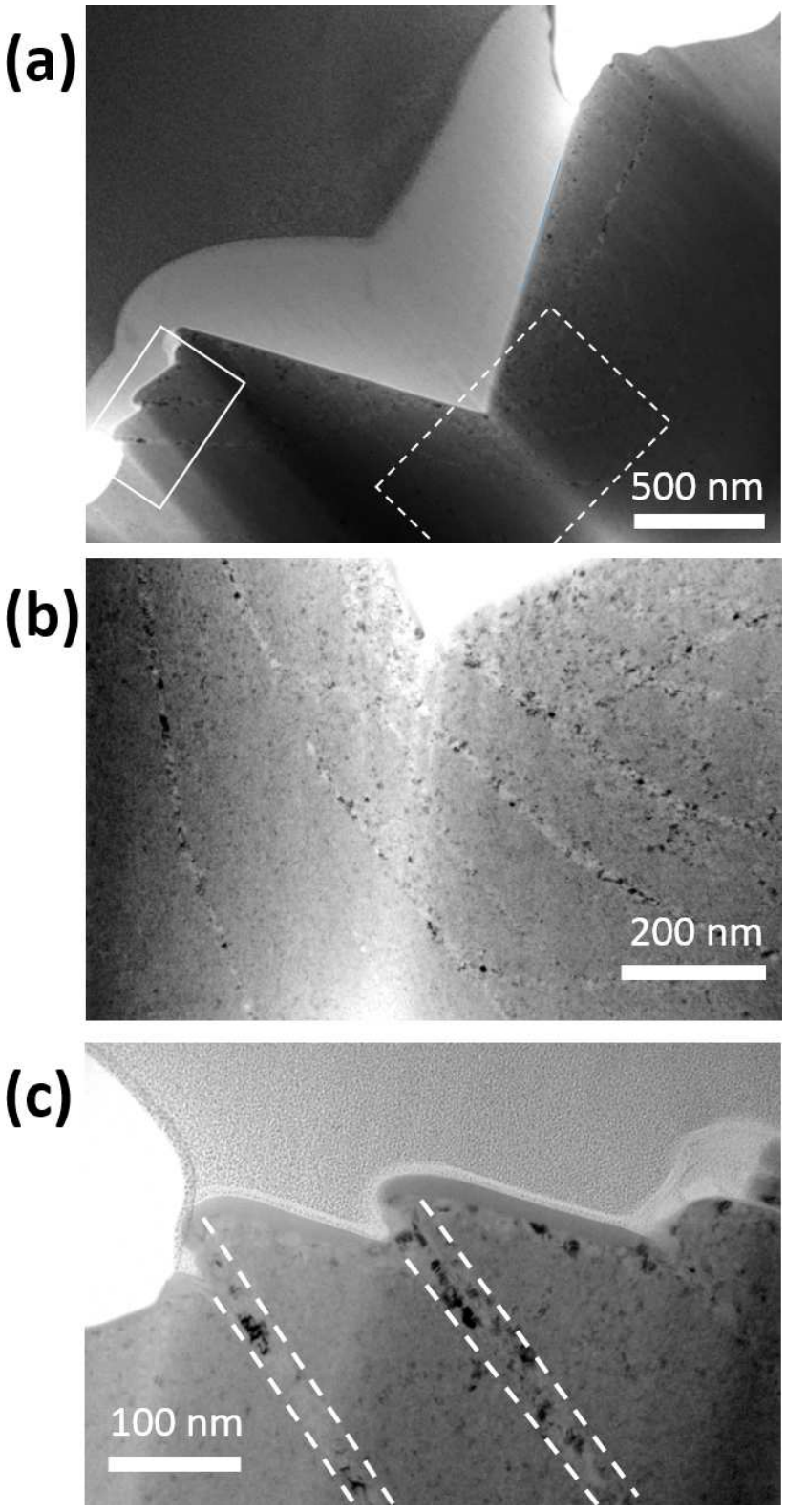

Figure 3.5 TEM images of Ni-W after nanoindentation: (a) TEM image of the entire indentation cross-section. (b) Magnified image of the dashed box showing the shear bands diretly underneath the indenter tip. (c) Magnified image of the solid box, showing shear bands which terminate at the surface and create slip steps.

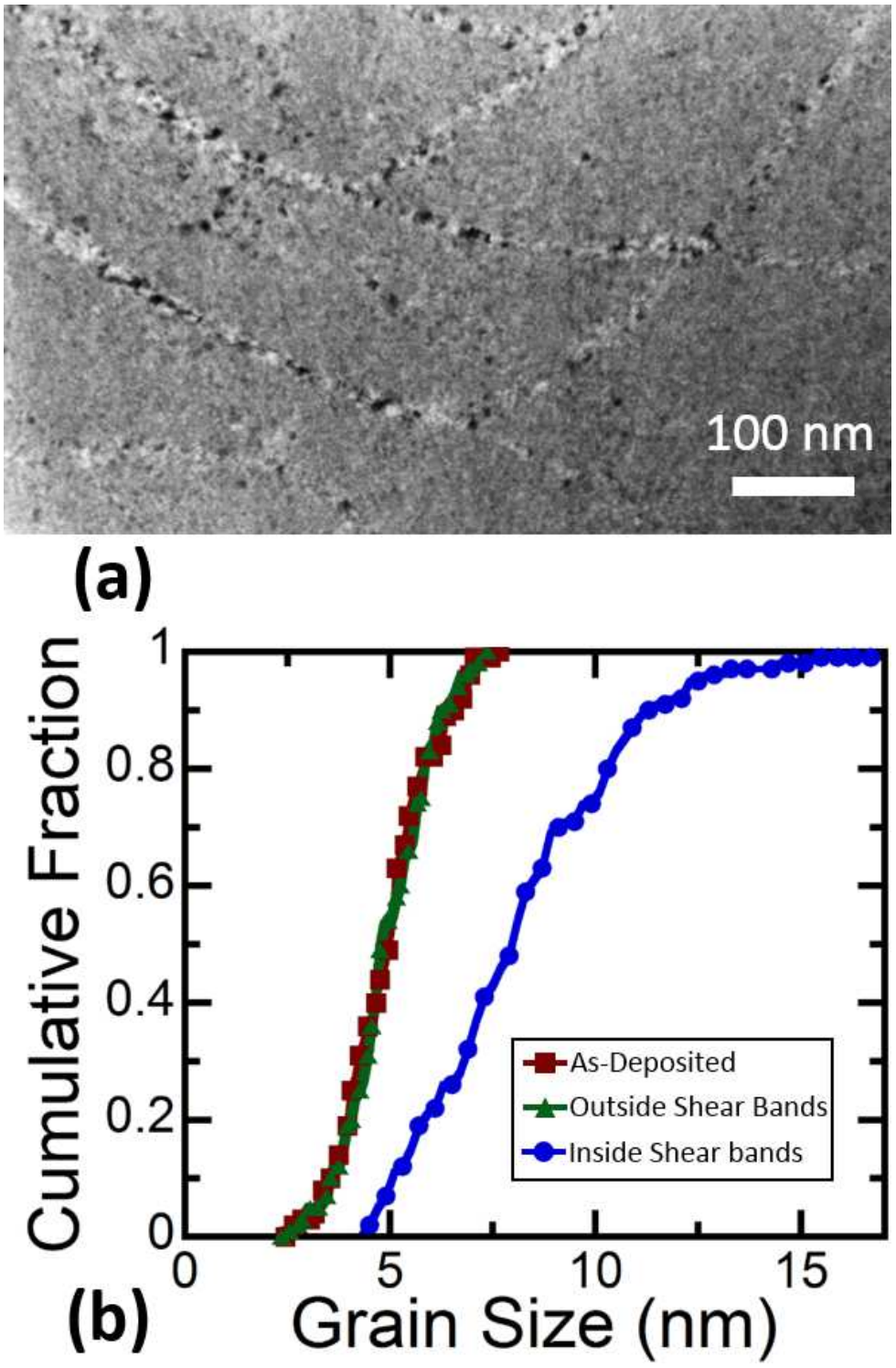

Figure 3.6 Microstructure after nanoindentation: (a) The microstructure of the same indent in the pile-up on the surface of the sample; TEM image of shear bands forming an intersecting network underneath an indent. (b) Cumulative distribution function of grain size Cumulative fraction vs. grain size from grains inside and outside the shear bands, as well as the original as-deposited relaxed microstructure.

3.4 Discussion

The experiments described above show that nanocrystalline alloys with extremely fine grain sizes can experience strain localization in the form of shear banding, mimicking prior observations in metallic glasses. This similarity can be understood by recognizing the features these materials have in common. Both metallic glasses and nanocrystalline metals are extremely strong, which has been shown to be important for strain localization [2,160]. If the ratio of strain hardening rate to the applied stress drops below a critical value, a material can be prone to flow localization [161]. In both nanocrystalline metals and metallic glasses, the applied stresses are extremely high and strain hardening is almost nonexistent, satisfying these conditions. In addition, both classes of materials are unable to store large numbers of dislocations and achieve large uniform elongations. For a metallic glass, dislocations do not exist at all due to the lack of long range crystalline order. For nanocrystalline metals, dislocations can carry some fraction of the overall plastic strain but they are absorbed after traversing grains and leave no residual dislocation density. In addition, the smallest nanocrystalline grains deform through direct rotation or sliding. While the existence of shear banding in both materials and the similarities between their overall mechanical behavior is important, the evolution of grain structure is our main finding in this paper.

Our observations of structural evolution inside of nanocrystalline shear bands show that intense strain localization leads to (1) grain growth and (2) the formation of a shear texture. The first type of evolution can be understood as the material being driven closer to an equilibrium state by high stresses during deformation. Atoms in the grain boundaries are defects and exist in a higher energy state than atoms found in the grain interiors. Grain growth reduces the volume fraction of material located inside of grain boundaries, although the extent of grain growth will be a complex convolution of effects relating to the active deformation mechanisms and the driving

force for growth. For a starting grain size of 5 nm, plasticity should be dominated by grain rotation and sliding, as well as grain boundary migration [16,24,162]. These mechanisms are able to efficiently coarsen grain structures, with grain rotation capable of causing grain coalescence [163,164] and boundary migration directly increasing the size of one grain at the expense of another. Rupert[56] used MD simulations to demonstrate that such mechanisms can cause grain growth during strain localization in polycrystalline nanowires with grain sizes similar to those studied here. However, as grains grow, there will be a gradual shift toward dislocation-based plasticity. Vo et al. [165] found that dislocation-based plasticity become the majority carrier of plastic strain as grains become larger than ~10 nm. Therefore, the grain growth will effectively shut itself off once grains are too large for collective grain boundary mechanisms to dominate plasticity. This idea is supported by our observation that the maximum grain size stayed below 20 nm in both nanoindentation and microcompression experiments. Another contributing factor could be supersaturation of the grain boundaries. Previous work by Detor and Schuh [15] demonstrated that only ~17-18 at.% W is enough to stabilize a d = 8 nm microstructure in nanocrystalline Ni-W, while our alloy here has 23 at.% W for this same grain size after coarsening. Considering that the increase in grain size has decreased the volume fraction of grain boundaries, and our careful examination of SAED patterns of shear bands shows no evidence of any second phase segregation or formation of W particles [127], the concentration of W at the grain boundaries should be even higher than the minimum value needed for thermal stability. With additional grain boundary doping, there will be a further decrease in the grain boundary energy, reducing the driving force for coarsening of the nanocrystalline structure.

Microstructural evolution toward a lower energy state is also observed in metallic glasses, where nanocrystalline structures are sometimes found inside or in the vicinity of shear bands [166].

For example, Jiang et al. [49,167] and Kim et al. [168] saw that small crystallites nucleated in indented regions of Al- and Zr-based bulk metallic glasses, respectively. Zheng et al. [169] also observed shear bands with nanocrystals inside of a MgCuGd metallic glass consolidated with high pressure torsion (HPT), where a material is deformed in a torsional mode while under a confining pressure. During shear banding, the atoms which were originally in an amorphous configuration have the ability to settle into a crystalline state. Most studies suggest that this evolution process is related to the creation of excess free volume, enhanced atomic shuffling, and high local strain rates inside of the shear bands [166,167,170]. However, other authors have found that local temperature rise inside of shear bands can cause crystallization, and this temperature rise is often accompanied by the formation of vein patterns or liquid like droplets [171,172] on the surface of the sheared specimen. Evolution driven by local temperature fluctuations will also result in diffuse shear bands, with gradual structural evolution as one moves away from the band [166]. However, our experimental observations suggest that such local temperature rise is not a contributing factor to the structural evolution in nanocrystalline Ni-W. SEM images of the failure surfaces from the microcompression samples showed no vein patterns and the slip surfaces resembled a clean fracture. In addition, our TEM images showed shear bands with well-defined edges and no gradient in the microstructure was found in the vicinity of the shear bands. As such, it appears that our evolution is purely driven by mechanical stresses.

The observation of texture formation can be explained by a shift to dislocation-based mechanism through a combination of grain growth and high plastic strains. Previous studies [173,174] have shown that plasticity due to grain boundary sliding and grain rotation randomizes texture, similar to observations of superplastic behavior in nanocrystalline metals [175]. However, once grains get larger than ~10 nm [165], plasticity is dominated by dislocation glide, which has

been shown to induce preferred orientation (see, e.g., the formation of simple shear texture in nanocrystalline Ni [176]). The dominant deformation mechanism is also a function of plastic strain, with higher plastic strains increasing the importance of dislocation-based mechanisms [165]. This concept is supported by literature data from processing experiments. For example, Ivanisenko et al.[173] employed HPT on a nanocrystalline Pd and found that extremely high shear strains of 124 can result in grain growth and texture formation. However, Markmann et al. [174] showed that cold rolling of a similar nanocrystalline Pd to much lower plastic strain values does not cause any texture formation. Skrotzki et al. [177] studied the effect of severe plastic deformation on the texture of nanocrystalline Pd-Au more systematically, finding that a random texture was observed at low applied strains. This was then replaced by a "brass-type" shear texture once the applied shear strain exceeded 1.

The effect of the overall stress state can be understood by comparing the results of the microcompression with those of the nanoindentation. While a microcompression experiment applies a simple uniaxial stress to the micropillar, the indentation stress state is much more complicated under the indenter tip, having a combination of hydrostatic and deviatoric stress components. In addition, the stress-strain curve for microcompression shows that the only deviation from elasticity is discrete plastic deformation through shear banding. As mentioned in the Results section, there is a combination of homogeneous plasticity and shear banding in the case of our nanoindentation experiments. We find that the nanoindentation curve is smooth with just less than 10 displacement bursts caused by shear bands, each only ~10-15 nm in length. Additional experiments with even lower strain rates and higher data acquisition rates, which should make it easier to activate and identify shear bands, also showed the same behavior. If shear banding was the only contributor to plastic deformation, subtracting the pop-in displacements from the load-

displacement curve would give a loading curve that is predicted by Hertzian elasticity theory and negligible residual indentation depth after unloading. This is clearly not the case for our experiments on Ni-W, as a large plastic impression is left on the surface even through shear banding should only contribute ~100 nm of plastic depth.

Shear banding in nanoindentation experiments, in contrast to microcompression, cannot be responsible for all of the plastic deformation. Therefore, homogenous plasticity outside of the shear bands must have occurred during nanoindentation. However, by looking at the grain size distribution outside of the shear bands but within the plastic zone of the indentation, we find that homogenous plasticity does not drive structural evolution, as the average grain size and even the details of the grain size distribution are identical to the as-deposited microstructure. This observation contrasts with previous observations of pure nanocrystalline metals, which experience grain growth during the early stages of plasticity in uniaxial tension experiments [84]. Doping of grain boundaries with W makes the microstructure stable against coarsening at small plastic strains, analogous to the increase in thermal stability, but this structural stability can be overcome when intense shear localization occurs. These results suggest that the microstructure of even thermally-stable nanocrystalline FCC alloys should be considered dynamic, if extreme deformation conditions such as catastrophic shear banding can be accessed.

3.5 Conclusion

To summarize, the effects of shear banding on local grain structure were studied in a nanocrystalline Ni-W alloy with an as-deposited grain size of 5 nm. Microcompression experiments as well as nanoindentation tests were used to study the effects of different stress fields and deformation boundary conditions. Evidence of significant grain growth and texturing as a

result of strain localization was found inside of the shear bands. A degree of mechanically-induced grain growth was observed for both testing conditions, suggesting an inherent limit on this coarsening behavior that depends on multiple factors such as the dominant deformation physics and the driving force for grain growth, both of which change with grain size. Our results showed that the nanocrystalline Ni-W can be susceptible to grain growth only when extreme values of shear strain are applied, and suggest that this is a purely stress-driven process and not caused by local heating inside the shear bands.

Chapter 4 : Design of failure resistant nanocrystalline Cu-Zr by complexion engineering

4.1 Introduction

In Chapters 2 and 3, we saw that an ordered and relaxed grain boundary structure has detrimental effect on the failure behavior of nanocrystalline Ni-W. Therefore, a more disordered grain boundary structure should be advantageous for properties such as ductility and toughness. The extreme of grain boundary disordering is an amorphous grain boundary or Dillon-Harmer type V complexion. Therefore, it is expected that amorphous grain boundaries to improve failure resistant properties of nanocrystalline metals. In this chapter, we report on a strategy for combining the concepts of nanostructuring and complexion engineering, to enable a new class of materials: *nanomaterials with tunable grain boundary structure*. To date, complexions have been studied and utilized predominantly in either coarse-grained polycrystalline materials or simple bicrystal samples. We begin by developing a processing route for making such materials, with an eye on techniques that are flexible enough to create a wide variety of chemistries while also scalable so that they can eventually be used to produce bulk quantities of material. Since AIFs are extreme complexions, with unique structure and properties, we focus on inducing and characterizing these features in a nanoscale grain structure. Then, the mechanical properties of the alloy are probed, to demonstrate the clear advantage of this new materials design strategy. Specifically, we find that the ductility and toughness of nanostructured metals can be greatly improved using complexion engineering without sacrificing any strength, breaking the paradigm of a direct strength-ductility trade-off that has dominated prior observations.

4.2 Materials and methods

4.2.1 Materials selection

Cu-based alloys were selected for this investigation, as Cu is a common face-centered cubic material and our findings should be broadly applicable to many other structural metals. In addition, the deformation physics and properties of pure nanocrystalline Cu have been well-studied, giving reference points to compare against [16]. Since doping of the interfacial regions is required to induce complexions, alloying elements which segregate to the grain boundaries are sought. Empirical considerations such as large atomic size mismatch and limited solubility in the bulk can give rough guidelines for dopant selection, while grain boundary segregation enthalpy calculations give a more direct prediction of segregation tendency [88]. Since this study is concerned with mechanical behavior, embrittlement is to be avoided and there is a need to preserve metallic bonding at the interfaces. Non-metals or poor metals such as Bi and Pb are eliminated from consideration. Finally, thermodynamic modeling tools developed by Luo and coworkers [119,178] suggest that AIFs will form if the total energy of an amorphous layer with finite thickness and two new amorphous-crystalline interfaces (i.e., the entire complexion) is lower than the energy associated with the interface between two crystalline phases (i.e., the original grain boundary). This means that alloy combinations that have a low volumetric free energy penalty for a liquid-like structure and can easily form amorphous solids are promising for the formation of AIFs. With all of these considerations in mind, Zr was chosen as our alloying element, since it will segregate to the grain boundaries [88], is a transition metal, and binary Cu-Zr alloys have a high glass-forming ability [179].

4.2.2 Materials processing

Nanocrystalline Cu and Cu-3 atomic % Zr powders were produced from -170+400 mesh Cu powder and -50 mesh Zr powder using mechanical alloying. Cu powders with 99.9% purity and Zr powders with 99.7% purity were obtained from Alfa Aesar and Micron Metals, respectively. Mechanical alloying of the powders was performed with a SPEX 8000M mixer/mill equipped with a hardened steel vial and milling media. A ball-to-powder ratio of 10:1 was chosen, and 1 weight % stearic acid was added as a process control agent to minimize cold welding. The milling was performed inside of a glove box under a 99.999% pure Ar atmosphere, to avoid oxidation of the powders. Both pure and alloyed Cu powders were annealed in vacuum sealed quartz tubes at 950 °C inside a tube furnace for 1 h and quenched rapidly in water (within ~1 s). In addition, a control sample from the Cu-Zr alloy was air-cooled to study the effect of cooling rate on the microstructure. The furnace temperature was stable to within ±1 °C, ensuring that the annealing temperature never approached or exceeded the solidus temperature (972 °C). The phase content of the powder samples was measured using a Rigaku Ultima III X-ray diffractometer equipped with a Cu Kα radiation source operating at 40 kV. The powder samples were mounted in a conductive epoxy and mechanically polished to a mirror finish for further characterization.

4.2.3 Electron microscopy and characterization

TEM samples were prepared from individual powder particles using a FEI Quanta 3D dual beam SEM and focused ion beam (FIB) microscope. The TEM samples were polished with a 5 kV Ga^+ ion beam to remove and minimize any damaged layer from the TEM sample preparation procedure. SEM imaging was performed with the same instrument operating at 5 kV. Ewas done at 20 kV in the same microscope to probe for iron contamination and inhomogeneity in the sample

at the micron scale. TEM bright field images were taken using a FEI/Philips CM-20 TEM operating at 200 kV. The mean grain size for each sample was calculated by manually tracing and measuring the area of at least 100 grains and calculating the equivalent circular diameters. A Fresnel fringe imaging technique was used to identify grain boundary films, as local differences in atomic density or composition lead to such fringes at interfaces in under- or over focused conditions [180]. Once interfacial films were found, high resolution TEM was used for thickness measurement, as direct measurements of thickness using Fresnel fringes have been shown to be unreliable [181]. High resolution, phase contrast TEM images were taken using a FEI Titan TEM operating at 300 kV. Scanning TEM imaging and Energy-dispersive X-ray spectroscopy (EDS) were performed with the same instrument operating at 80 kV.

4.2.4 Mechanical testing: Microcompression and bending

At least five micropillars with diameter and length of 5 ± 0.1 μm and 16 ± 0.2 μm, respectively, were fabricated using FIB lathe milling on individual powder particles following the method of Uchic and Dimiduk [70]. This technique produced taper-free pillars so that a uniform stress state can be induced. The pillar diameters were >100 times the average grain size, ensuring that the measured response would be representative of "bulk" response and not external size effects [182]. The uniaxial microcompression test was performed with an Agilent G200 nanoindenter using a flat triangular diamond tip and a constant displacement rate of 5 nm/s, giving an engineering strain rate of 3.1×10^{-4} s^{-1}. The load-displacement data was converted to engineering stress-strain using the initial length and diameter of the pillars measured with SEM. Yield strengths, σ_y, were calculated based on a 0.7% plastic strain offset, following the work of Brandstetter et al. [141].

Microbeam bending experiments were performed inside the dual beam FIB/SEM microscope using an Omniprobe micro-manipulator. At least three micropillars were tested in bending by pushing the top of the pillars at a speed of 0.1 μm/s. This testing methodology results in uniaxial strain, ε, at the bottom of the pillars, with tension on one side and compression on the other. The basic geometry of the deformed base resembles a simple beam bending problem, where there is a neutral axis with zero strain and the distance from that neutral axis can be combined with the radius of curvature of the beam to calculate axial strain. To measure the bending strain in each pillar, first we fit a circle with radius, R, to the curvature of the neutral axis and then we fit another circle, with another radius, $R+x$, to the outside edge of the micropillar. This process is shown in Fig 4.1. Since the measurements are taken after the loading is removed, relieving any elastic deformation, any strain measured is plastic strain and the plastic strain at failure is calculated as $\varepsilon_{failure} = x / R$.

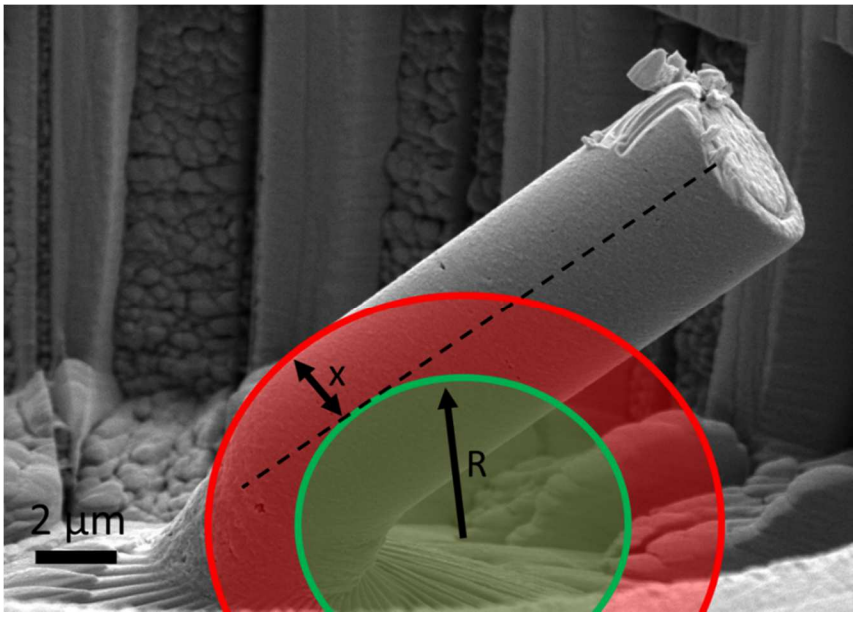

Figure 4.1 Calculation of bending strain after an in-situ bending experiment. The green circle with radius *R* is fitted to the curvature of neutral axis, and the red circle with radius of *R+x* is fitted to the curvature of the edge of the micropillar. The image was taken at a 60° tilt, and the circles are scaled to account for this effect.

4.3 Results and discussion

Mechanical alloying with a high-energy ball mill produces powders with particle sizes of micron-scale diameter, with each particle containing many individual nanometer-scale grains. This technique can make nanostructured powders with a wide variety of chemical compositions and scale-up to bulk parts through powder metallurgy techniques is a possibility [78]. As a control, unalloyed nanocrystalline Cu with d = 30 nm was first produced, as shown in Fig. 4.2(a) and (d). A Cu-3 atomic % Zr alloy was then created, as full segregation of this amount of Zr to the interfaces will put the grain boundary composition into the glass forming range for Cu-Zr metallic glasses [183]. In the as-milled state, the alloy sample also has d = 30 nm (Fig. 4.2(e)). The bottom frame of Fig. 1E presents a compositional line scan through the as-milled Cu-Zr alloy, showing that Zr is found throughout the sample, in both crystal interior and grain boundary regions (Fig. 4.2(b)). Three grain boundaries are labeled in this Figure with black arrows. A small amount of grain boundary segregation is occasionally found even in the as-milled sample, as shown by the slightly elevated Zr concentration at the first boundary noted, but significant amounts of Zr were inside of the grains as well. As Zr has negligible (~0.12 atomic % [184]) solubility in the Cu lattice according to the bulk phase diagram, this structure is a supersaturated solid solution. To induce segregation, the powders were sealed under vacuum in quartz tubes to avoid oxidation and then annealed at 950 °C for 1 h. This temperature is extremely high for Cu and Cu-Zr alloys, being ~90% of the melting temperature of pure Cu and ~98% of the solidus temperature (where the material begins to melt) of Cu-3 atomic % Zr [184]. During annealing, Zr diffuses to the grain boundaries, as shown by the compositional line scan in Fig. 4.2(f), where two obvious examples of grain boundaries are labeled. Grain interiors are depleted of Zr after annealing, while the interfacial regions show intense Zr enrichment (Fig. 4.2(c)). Additional evidence of Zr grain

boundary segregation was found by using high angle annular dark field TEM imaging. Figure 4.3 shows a high angle annular dark field (HAADF) STEM image of the nanocrystalline Cu-3 atomic % Zr annealed at 950°C and rapidly quenched, showing segregation of Zr to the grain boundaries.

The Cu-Zr alloy experiences very little grain growth, only coarsening to an average grain size of 45 nm (Fig. 4.2(f)), due to a reduction in grain boundary energy with Zr segregation[185], while the grain size of a pure Cu sample annealed under the same conditions coarsens to the micron range. Although not the explicit focus of this study, the observed thermal stability at such a high temperature suggests that this material can be consolidated into bulk pieces [78].

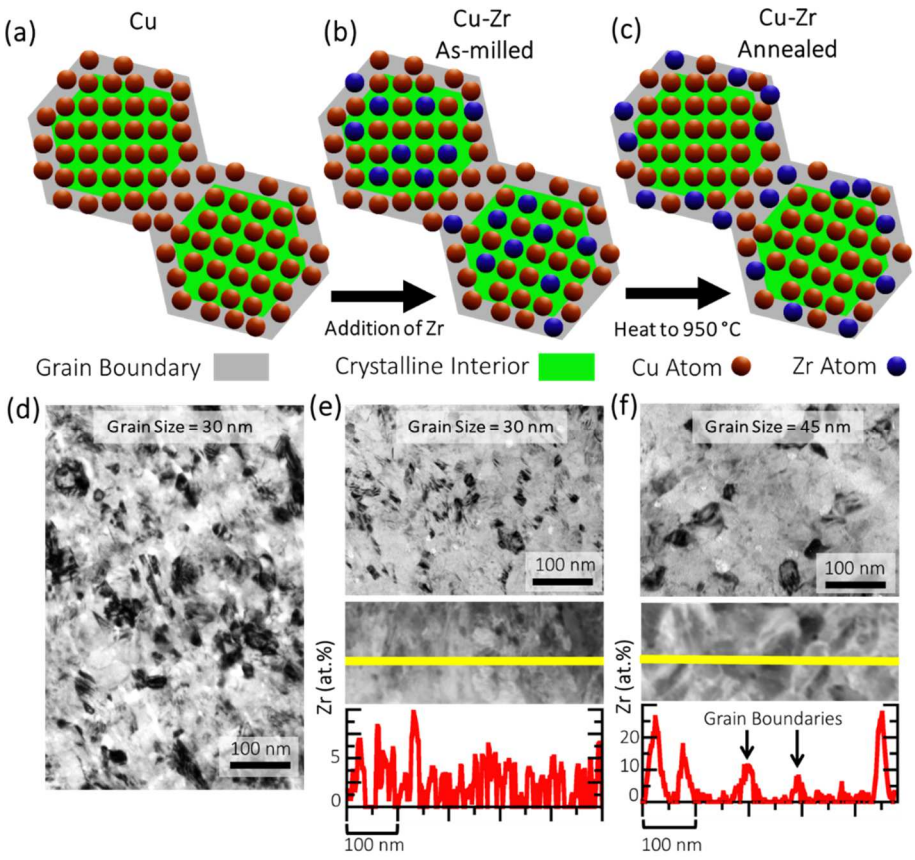

Figure 4.2 Alloy design strategy for adding segregating dopants. Pure Cu (a) can be converted to an alloy by adding Zr during ball milling (b). While the Zr is mixed throughout the grain structure, annealing treatments can then be used to induce preferential Zr segregation to the grain boundaries (c). Both the (d) pure Cu and (e) Cu-Zr as-milled samples have an average grain size of 30 nm. Annealing the Cu-Zr sample at 950 °C for 1 h allows for segregation and only causes coarsening to a grain size of 45 nm (f)

The high temperature annealing treatment used to induce Zr segregation is also useful for promoting AIF formation. Shi and Luo [119] recently developed interfacial thermodynamic models and grain boundary diagrams, showing that higher temperatures usually promote thicker AIFs. A set of annealed Cu-Zr powders were quickly quenched by dropping into a large water bath in less than 1 s, freezing in any structures which are in equilibrium at 950 °C. Fresnel fringe imaging [180] was used to identify interfacial films, followed by high resolution TEM for detailed characterization of grain boundary structure and measurement of AIF thickness. A representative example of an AIF is presented in Fig. 4.4(a). The areas in the bottom left and top right of Fig. 4.4(a) are crystalline, as shown by the presence of lattice fringes in the image as well as sharp spots in the fast Fourier transform patterns, which denote periodic order associated with the lattice. In contrast, the region at the interface, between the two dashed lines, is amorphous and disordered with a thickness of 5.7 nm. The fast Fourier transform pattern shows no sign of long-range crystalline order in this case and is completely featureless.

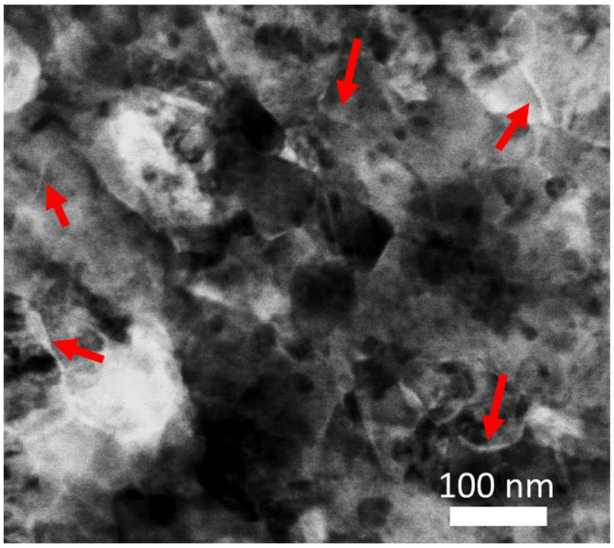

Figure 4.3 HAADF STEM image of nanocrystalline Cu-3 atomic % Zr heat treated to 950 °C and rapidly quenched. Brighter regions have higher concentration of Zr, with a few examples denoted by red arrows showing obvious Zr segregation at the grain boundaries.

To ensure that the observed AIFs were truly complexions, driven by alloy thermodynamics with a combination of grain boundary dopants and elevated temperatures required, and did not form through another process such as solid-state amorphization which is purely driven by local composition, another set of powders was annealed at 950 °C and then slowly cooled back to room temperature over a period of ~5 minutes, or ~300 times longer than the quenched sample. Such a cooling schedule gives a sample with interfaces that are in equilibrium at ambient temperatures. No AIFs were observed in this specimen and all interfaces studied were ordered, with a representative example shown in Fig. 4.4(b). Crystalline order is present all of the way up to the boundary. Although the boundaries were still heavily-doped with Zr, the lack of AIFs proves that the amorphous structure shown in Fig. 4.4(a) is only in equilibrium at high temperature, in line with thermodynamic theories of disordered complexions.

Additional examples of AIFs from the quenched Cu-Zr sample are shown in Fig. 4.4(c) and (d), with thicknesses of 2.2 nm and 1.3 nm, respectively. Twenty-eight AIFs were studied with high resolution TEM, with a distribution of measured AIF thicknesses shown in Fig. 4.4(e). In addition, a number of ordered grain boundaries were observed in this sample as well. As a whole, this means that not all grain boundaries have the same structure in the quenched Cu-Zr alloy, but rather there is a distribution of complexion types. Possible explanations for these variations include differences in grain boundary energy, local segregation state, or slight differences in local cooling rates during quenching. The existence of amorphous structures below the solidus temperature of the alloy suggests that these features are stable AIFs with thicknesses determined by a combination of local grain boundary chemical composition and high temperature (type V), although some of the thicker AIFs could actually be wetting films (type VI). Even though

the annealing temperature was below the solidus temperature for Cu-3 atomic % Zr, it was above the eutectic temperature, the lowest possible melting temperature over all mixing ratios, which occurs at higher Zr concentrations. It is possible that some boundaries have higher levels of Zr segregation and move into a different region of the phase diagram where wetting films can form at 950 °C. However, previous observations of complexions in Al_2O_3 showed that film thickness changes significantly along individual wetting films [186]. In contrast, each individual boundary studied here showed no measureable variation in thickness. In addition, wetting films are often much thicker (at least 10 nm thick) than the films observed here. Although there is some uncertainty about the complexion type of each individual AIF, the existence of many nanometer-thick amorphous interfacial structures is clear.

To demonstrate the potential utility of the material described in this report, a nanostructured metal with disordered amorphous grain boundaries, we turn our attention to mechanical behavior. Nanocrystalline metals have very high strengths, but are generally also very brittle and exhibit little ductility, with elongations or strain-to-failure values of only a few percent typically reported [3,187]. This brittle nature often restricts the usage of nanocrystalline materials in technological applications. The high strength comes from the fact that traditional, intergranular dislocation plasticity mechanisms are shut off at these extremely fine crystallite sizes, requiring dislocations to be nucleated at an interface, propagate across the nanograin, and then be absorbed at the opposite grain boundary. The repeated dislocation absorption required for such a physical mechanism may be the cause of the brittle nature of nanocrystalline metals, as atomistic simulations show that a single absorption event leads to high local stresses at the grain boundary [188] while multiple absorption events result in crack nucleation [189]. Such a hypothesis is supported by in situ TEM deformation studies, which show that nanometer size cracks nucleate at grain boundary sites

during plastic deformation [145]. As a result, damage tolerant grain boundaries should be the key to designing ductile nanocrystalline metals, making control of grain boundary structure a priority.

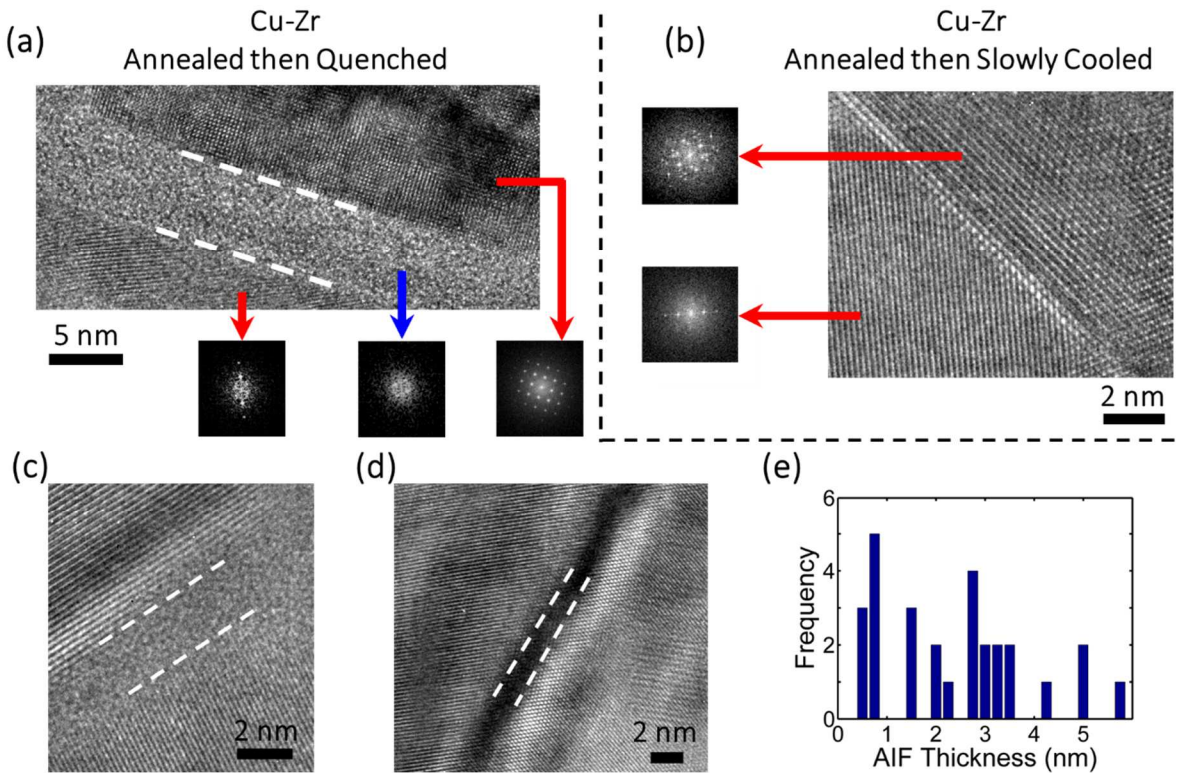

Figure 4.4 High resolution TEM images of grain boundary structure in nanocrystalline Cu-Zr alloys. (a) An AlF with thickness of 5.7 nm was observed at a grain boundary after quickly quenching from 950 °C. In contrast, grain boundaries in a slowly cooled sample, with structures that are in equilibrium near ambient temperatures, are all ordered interfaces (b). Insets are fast Fourier transform patterns, highlighting the disordered nature of the interface in (a). (c and d) present additional examples of amorphous complexions in the quenched sample, while (e) summarizes the measurements from the 28 interfacial films found here.

Small cylindrical specimens were created in the powder particles using a Focused Ion Beam (FIB) microscope, then tested in compression and bending modes, to quantify strength and strain-to-failure, respectively. Representative examples from each test for pure nanocrystalline Cu are shown in Fig. 4.5(a) and (c), demonstrating the typical response of a nanocrystalline metal to which we can then compare our Cu-Zr results. Fig. 4.5(a) shows that pure Cu has a high yield strength of 740 MPa but the pillar cracks and fails, resembling the failure of a brittle ceramic. Fig.

4.5(b) and (c) shows this same brittle response during bending, where a crack forms early during the experiment and there is little plastic strain built up at the base of the pillar, from which strain-to-failure can be estimated as 4.4%. This low value is nearly identical to a previous report for nanocrystalline Cu, produced by a different method and tested in tension, that had a similar grain size and yield strength [190]. Representative examples for each test from our Cu-Zr alloy with AIFs are shown in Fig. 4.5(g) and (i), providing evidence of a strong yet ductile response. Fig. 4.5(g) shows that the Cu-Zr with AIFs is even stronger than the pure Cu, having a yield strength of 1086 MPa, but more importantly the pillar compresses in a stable, homogeneous fashion. Fig. 4.5(h) shows that the pillar is ductile during the bending experiment as well and a strain-to-failure of 56% was measured for these alloys, more than ten times larger than the pure Cu value. A magnified view of the pillar base is presented in Fig. 4.5(i), showing that extensive plasticity has occurred and that, even at this large plastic strain, there are only small, unconnected cracks instead of a crack completely across the surface, suggesting that this strain-to-failure value may even be slightly conservative for this alloy. To highlight the importance of AIFs for the observed behavior, mechanical tests were also performed on the Cu-Zr sample that was slowly cooled in order to have ordered grain boundaries. These results, presented in Fig. 4.5(d) and (f), demonstrate that this alloy is brittle as well, mimicking the pure Cu sample by crumbling in compression and failing at a small strain in bending. Since the only difference between the Cu-Zr samples is the grain boundary structure, with grain size and Zr segregation state identical for both samples, the increased ductility of the Cu-Zr with AIFs can be attributed to the addition of amorphous interfacial films alone. Stress-strain curves for all three samples are presented in Fig 4.6.

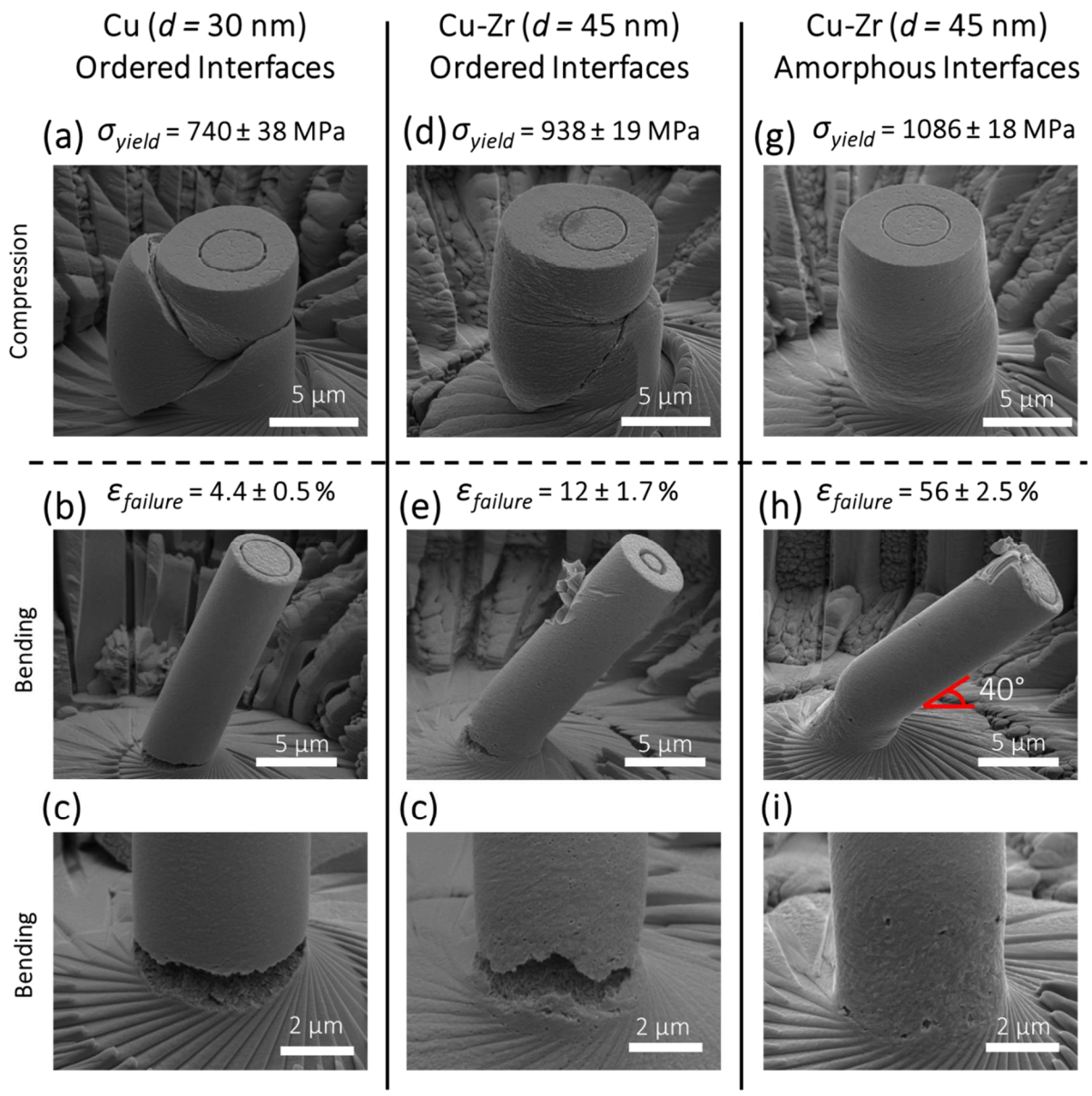

Figure 4.5 Mechanical testing results from nanocrystalline Cu and Cu-Zr samples. Failed micropillars after compression, as well as yield strength measurements, are shown for (a) pure Cu with ordered interfaces, (d) Cu-Zr with ordered interfaces, and (g) Cu-Zr with AIFs. Failed micropillars after bending, as well as elongation-to-failure measurements, are shown for (b and c) pure Cu with ordered interfaces, (e and f) Cu-Zr with ordered interfaces, and (h and i) Cu-Zr with AIFs. A nanocrystalline alloy with AIFs can be both stronger and more ductile than its traditional, pure metal counterpart.

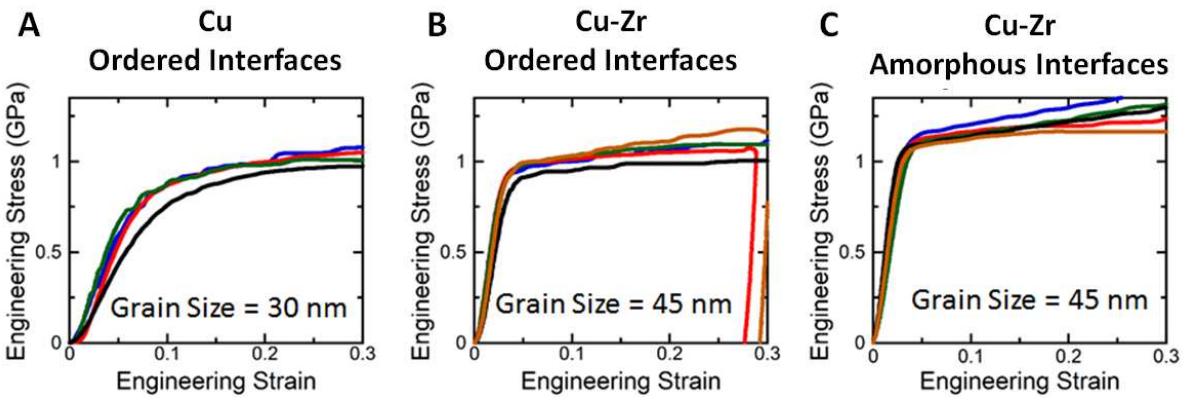

Figure 4.6 Microcompression testing results. Stress-strain curves for (A) pure Cu, (B) Cu-Zr with ordered grain boundaries, and (C) Cu-Zr with AIFs. These experiments provide information about the yield strength of each material.

Our results agrees with the molecular dynamic simulation study by Pan and Rupert who explored the mechanics of this problem systematically in a recent paper, finding that crack nucleation as well as crack growth rate is suppressed as AIF thickness increases [191]. Brandl et al. even showed that an AIF can exert attractive forces on nearby dislocations since it is elastically softer than the crystalline lattice, pulling dislocations towards the interface where they can then be absorbed [192]. Experiments on crystalline-amorphous nanocomposite films support this concept as well, as the addition of a thin amorphous layer was found to improve strain-to-failure when compared to films with only a crystalline phase [124]. Although the nanocomposites outperform the crystalline films, the strain-to-failure values were only ~12% (much lower than the values reported here), likely because the AIFs were only added in one direction of the film. In contrast, our materials have a fully three-dimensional grain boundary network decorated with AIFs. In our case, by adding amorphous interfacial features, it is possible to have the strength characteristic of a nanocrystalline metal without the typical low ductility (Fig. 4.7(a)). In fact, the ductility of a nanocrystalline metal with AIFs (Fig. 4.7(b)) resembles the ductility of a coarse-grained metal (Fig. 4.7(c)).

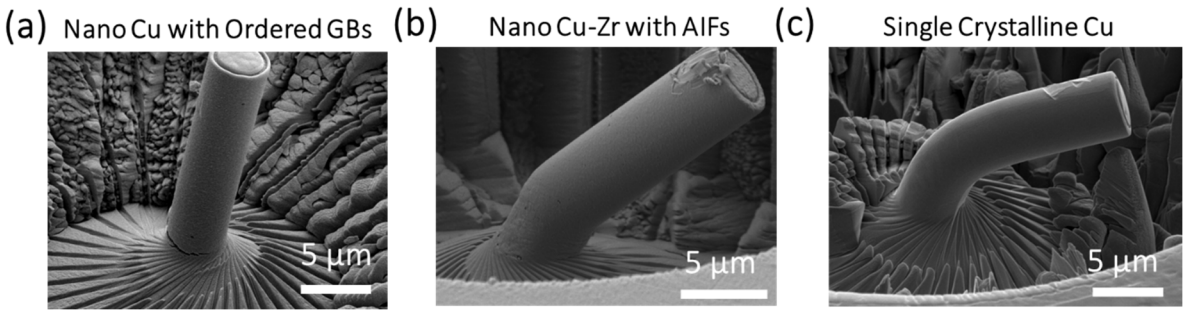

Figure 4.7 Micro beam bending of (a) nanocrystalline Cu (b) nanocrystalline Cu-Zr with AIFs, and (c) coarse-grained Cu.

A compilation of data from the literature for Cu and Cu alloys is presented in Fig 4.8, where elongation-to-failure is plotted as a function of yield strength. The properties of traditional Cu, both microcrystalline and nanocrystalline, fall within the grey envelop, demonstrating a clear trade-off between strength and ductility. Advanced alloys, such as Cu with a bimodal grain structure (micron-scale grains embedded in a matrix of nanocrystalline grains) and nanotwinned Cu, push beyond this and demonstrate improved combinations of these properties. The Cu and Cu-Zr alloys described in this paper are shown as red points on the plot. The pure Cu sample exhibits classical behavior and falls within the grey envelop, with a high strength (740 MPa) but a low elongation-to-failure (4.4%). The almost perfect agreement of these values with the measurements of Wang et al. [190], taken from nanocrystalline Cu with the same grain size produced by surface mechanical attrition, speaks to the robust nature of our measurement techniques. Alternatively, the Cu-Zr with AIFs breaks the traditional paradigm. It is both stronger and more ductile than the pure Cu sample, showing that control of grain boundary structure is a promising pathway for the design of optimized structural materials.

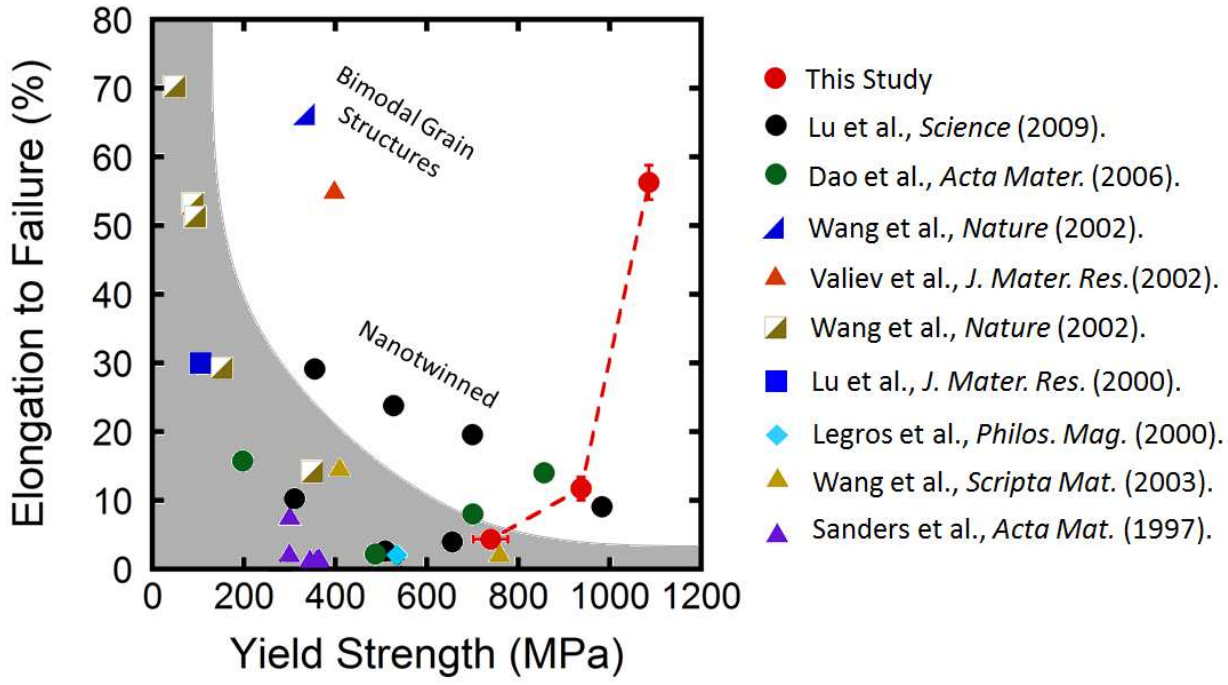

Figure 4.8 Elongation-to-Failure and Yield Strength for Cu and Cu-based alloys. The vast majority of data falls within the grey envelop, with recent advanced alloys pushing outside this limit. Our Cu-Zr alloy breaks the expected trend, with both higher strength and ductility than the pure Cu sample. Literature data is taken from [43,44,152,187,190,193,194].

The observation of high strength with large ductility fits a recent narrative that nanocrystalline materials are intrinsically ductile on the nanoscale [195], but suffer from premature failure due to strain localization or cracking [196]. If this premature failure can be suppressed, then the traditional trade-off between strength and ductility can be avoided. One recently developed path for suppression of this premature failure is to incorporate nanocrystalline metals as the outer layer in a gradient architecture, where grain size changes continuously from nanometers to microns to avoid early plastic necking [175,197]. The results presented here for Cu-Zr alloys created by a unique processing route can be interpreted as another example of this design strategy, with an explicit focus on resisting crack nucleation and growth through the introduction of grain boundary complexions. A strength-ductility synergy is achieved and our materials outperform traditional metals.

4.4 Conclusion

Our study shows that the previously separate techniques of nanostructuring and complexion engineering can be combined in a complementary manner, introducing a new feature into the design toolbox of materials scientists: *grain boundary structure*. Unique Cu-Zr alloys are reported, created through powder metallurgy techniques, with AIFs "frozen" into the interfaces as a result of Zr segregation and rapid quenching from high temperature aging treatments. These new materials demonstrate a combination of strength and ductility that is not found in traditional Cu alloys, behavior that can be attributed directly to the fracture resistance of AIFs. However, it is important to note that mechanical behavior is one of many places where the materials described here may be useful. Even if only focusing on nanocrystalline metals with amorphous complexions, we envision materials that can be rapidly consolidated due to faster diffusion along AIFs or that are more tolerant to radiation damage with AIFs acting as sinks for residual point defects. Amorphous interfaces could also act as fast transport paths for energy or electronic applications. We suggest that the introduction of nanocrystalline materials with designed grain boundary structures will dramatically broaden the suite of material properties that can be achieved.

Chapter 5 : High-temperature stability and grain boundary complexion formation in a nanocrystalline Cu-Zr alloy

5.1 Introduction

We saw in the previous chapter that grain boundary complexions have the potential to dramatically alter the behavior of nanocrystalline materials, and could be formed when high levels of grain boundary doping are present and elevated temperatures are experienced. Consequently, complexions may alter the thermal stability of these materials as well. To date, little attention has been given to grain boundary complexion formation and structural transitions in doped nanocrystalline metals. In this study, we report on the annealing of a nanocrystalline Cu-Zr alloy created by high-energy ball milling, with a focus on studying the segregation of dopants to grain boundaries and the formation of complexions as a function of temperature. Our results indicate thermal stability in nanocrystalline samples annealed at temperatures as high as 98% of the solidus temperature for a period of 1 week. Upon closer inspection, grain boundary complexions were observed, with the level of interfacial disorder and grain boundary thickness increasing as temperature increased.

5.2 Materials and Methods

Nanocrystalline Cu-3 at.% Zr alloy powders were produced using a SPEX 8000M high-energy ball mill. Cu was chosen as the base element since nanocrystalline Cu systems have been studied extensively in the literature.[78] Zr was then picked as the doping element for several reasons. Cu and Zr have a large atomic size mismatch and different crystal structures, so Zr has a high tendency to segregate to the grain boundaries in this mixture. Such behavior is also predicted by the fact that Zr has very limited solid solubility in Cu, only 0.12 at.% at the eutectic temperature.

Furthermore, Cu and Zr have been shown to have good glass forming ability, giving the possibility of AIF formation.[198,199]

A 99.99% pure and -170+400 mesh Cu powder from Alfa Aesar was mixed with a 99.7% pure and -50 mesh Zr powder from Micron Metals in a hardened steel vial. The ball milling machine was placed inside of a glove box in an Ar atmosphere to avoid oxidation. Stearic acid in the amount of 1 wt.% was added to the mixture as a process control agent to prevent cold welding. The powder mixture was milled for 10 h with a ball-to-powder ratio of 10:1. To prepare the samples for heat treatment, each powdered sample was sealed under vacuum in a high purity quartz tube. Annealing treatments were performed with a vertical tube furnace and the samples were quickly quenched by dropping into a water bath in less than 1 s, in order to preserve any high temperature interfacial structures. Samples were annealed at 550 °C, 750 °C, 850 °C, and 950 °C. Three samples were made at each temperature by annealing for 1 h, 24 h (1 day) and 168 h (1 week). All the samples were analyzed with X-ray diffraction (XRD) before and after annealing using a Rigaku Ultima III diffractometer with a D/teX Ultra 250 1D detector for grain size measurement and phase identification. XRD grain size was measured using the (111) peak of Cu and the Scherrer equation.[133] An error bar of ±15% has been added to the measured XRD grain size of each sample to account for uncertainties that results from theoretical assumptions.[200] Each powder sample was then mounted, without compaction, using a cold conductive epoxy system on a standard SEM stub and polished to a mirror surface finish.

TEM samples were made from individual powder particles with a focused ion beam using a FEI dual beam Quanta3D microscope. Each TEM sample was polished with a 5 kV Ga^+ ion beam to reduce the beam damage. Bright field and dark field TEM images, as well as selected area electron diffraction (SAED) patterns, were taken using a Philips CM-20 operating at 200 kV.

Average grain sizes from TEM were found by measuring at least 100 grains and taking the equivalent circular diameter. EDS and scanning TEM imaging were performed using an FEI Titan operating at 80 kV, while high resolution TEM imaging was carried out with the same instrument at 300 kV. Fresnel fringe imaging was employed to find grain boundary films and identify edge-on grain boundaries.[181] Finally, hardness measurements were obtained with an Agilent nanoindenter equipped with a Berkovich tip. A constant loading rate of 1 mN/s and an indentation depth of 400 nm were employed. At least 20 measurements were taken for each sample and annealing condition.

5.3 Microstructure characterization

5.3.1 Grain size and grain boundary segregation

The XRD grain sizes of the annealed samples are shown in Fig. 5.1 as a function of annealing time. The grain size of the as-milled sample (18 nm) is also plotted as a straight orange line for reference in the same Figure, with error bars denoted by orange shading. Small increases in the average grain size are found after annealing the samples for 1 h at 550 °C, 750 °C, and 850 °C, followed by slow but constant growth at longer times. Even after annealing these samples for a period of 1 week, the grain sizes remain below 35 nm. Elemental Cu has a relatively low melting temperature of 1084 °C, but the solidus temperature where Cu-3 at.% Zr begins to melt is even lower at 972 °C. Therefore, annealing temperatures of 550 °C, 750 °C, and 850 °C are high for this alloy, being 66%, 82%, and 90% of the solidus temperature, respectively. Increasing the annealing temperature to 950 °C, or 98% of the solidus temperature, leads to higher levels of grain growth compared to the other annealing conditions. However, the material remains nanocrystalline even after annealing for a period of 1 week, with an average size of ~54 nm.

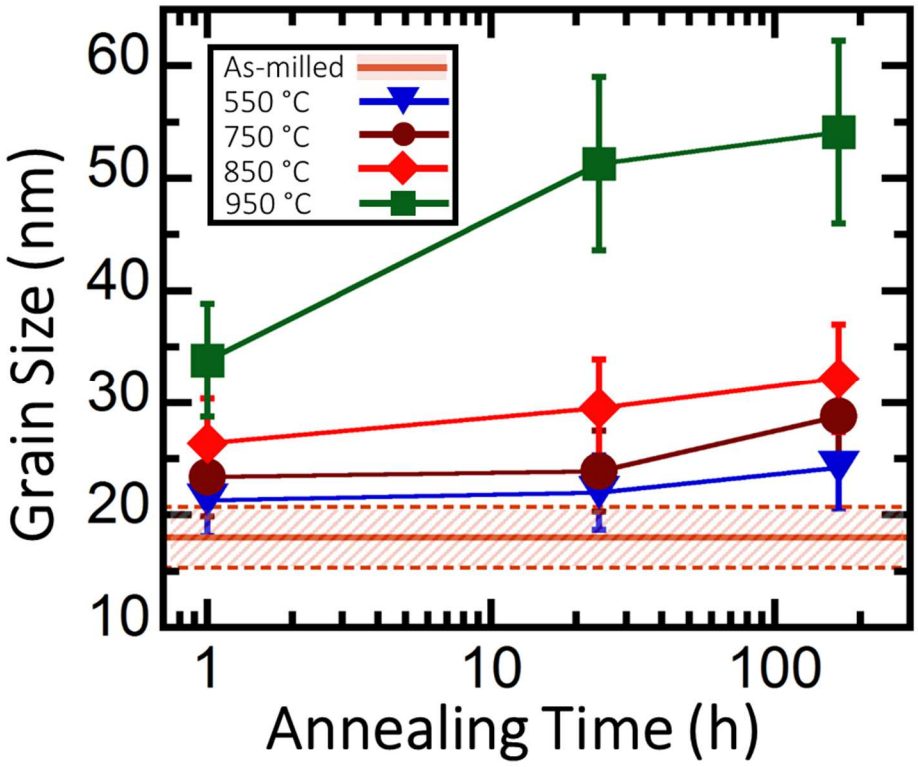

Figure 5.11 XRD grain size for the as-milled Cu-Zr sample as well as samples annealed at different temperatures. A ±15% error bar was applied to all the measured grain sizes to account for measurement inaccuracies due to theoretical and instrumental limitations.

To confirm the trend observed with XRD, TEM analysis was also performed. Fig. 5.2 shows bright field TEM images of the samples annealed for 1 h. All of the samples have equiaxed grain structures and no abnormal grain growth was detected. The insets in the Figure show SAED patterns for each sample. Cu FCC rings are clearly visible with the addition of faint rings of a second phase, most easily seen inside of the (111) Cu diffraction ring. Further analysis showed that ZrC particles are formed during annealing, which will be discussed in more detail in Section 3.3. To compare the XRD and TEM grain sizes, cumulative distribution functions of grain size are plotted in Fig. 5.3. XRD gives a slightly smaller grain size measurement in each case, likely

as a result of neglecting microstrain in the Scherrer equation [133]. However, a similar trend in grain growth is observed by both characterization methods and the samples remain nanocrystalline.

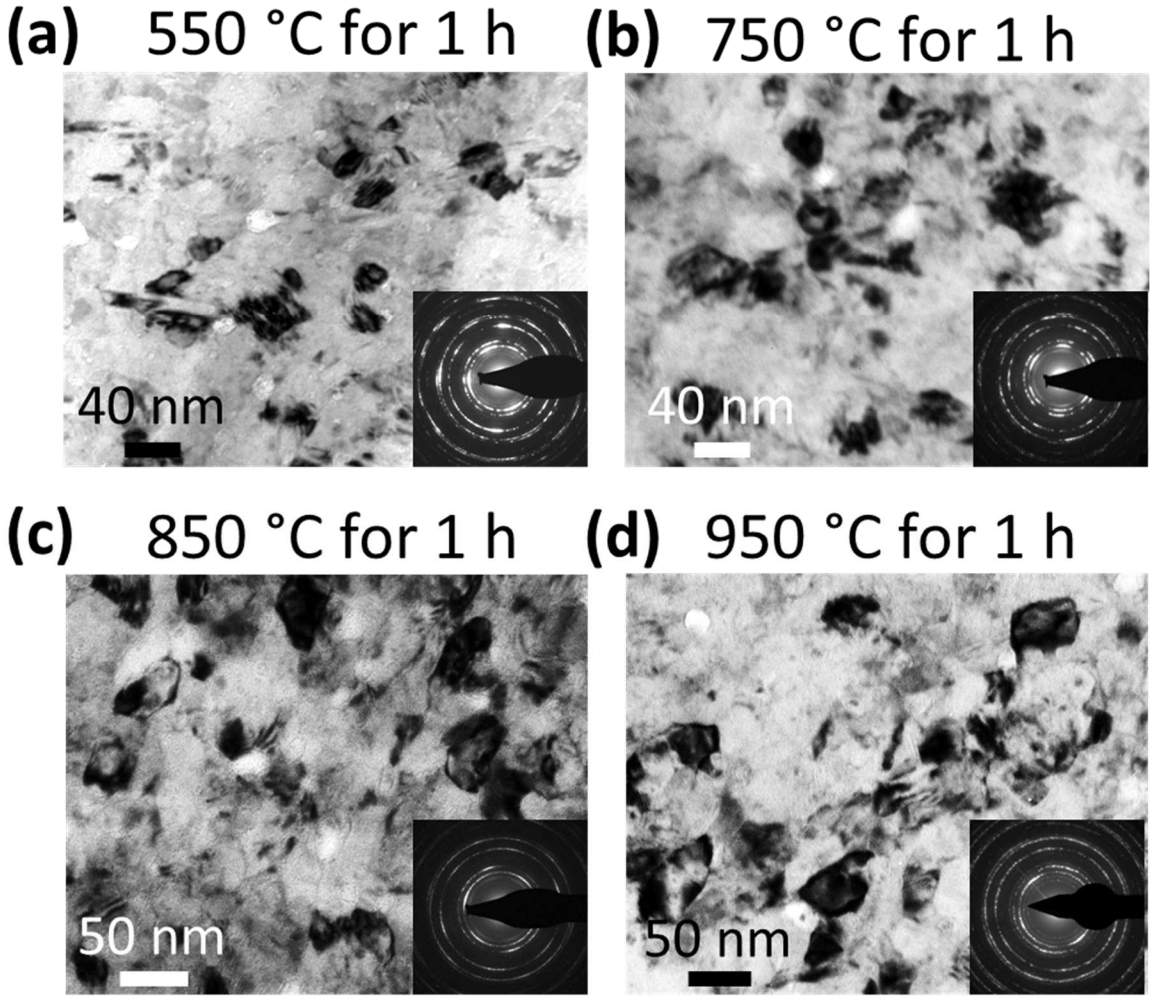

Figure 5.12 Bright field TEM image of Cu-3 at.% Zr annealed at (a) 550 °C, (b) 750 °C, (c) 850 °C, and (d) 950 °C. The inset in each Fig is the SAED pattern for that sample.

To understand the cause of the thermal stability of this alloy, EDS line profile analysis using scanning TEM was conducted to probe the Zr distribution within the microstructure, as shown in Figs. 5.4 and 5.5. Care was taken to make sure the concentration profiles were taken only from the FCC phase and not influenced by any ZrC particles in the microstructure. Interaction of the electron beam with the ZrC particles results in a sharp increase in the Zr concentration to

greater than 40 at.%, which was not observed here. The EDS data presented here should be considered semi-quantitative, not an exact measure of concentration at a point. As opposed to microcrystalline samples, EDS data obtained from nanocrystalline TEM samples may contain information from more than one grain through the thickness of the sample. The beam interaction volume may also lead to some slight spatial averaging on a nanometer scale.

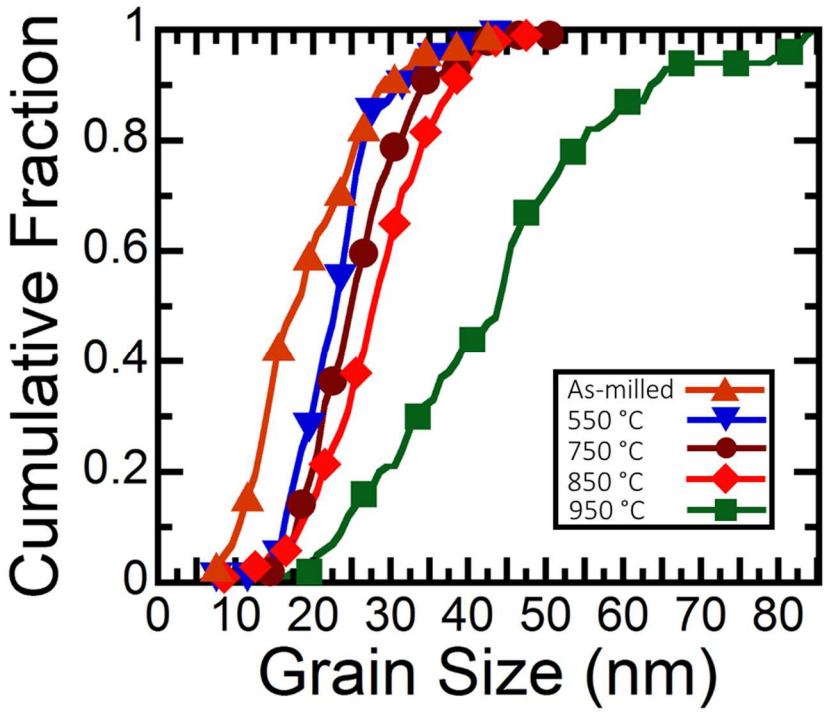

Figure 5.13 Grain size distribution in the as-milled sample as well as samples annealed for 1 h at different temperatures. All the samples show a narrow grain size distribution, with the ratio of the standard deviation to the average being relatively constant.

Fig. 5.4(a) shows a scanning TEM image and line profile scan of the sample annealed at 550 °C for 1 h. The concentration of Zr in this sample reaches maximas of about ~5-6 at.%, and a section of the profile is magnified directly below. The fluctuation of the Zr content in the sample roughly matches the observed grain size, and the locations of two obvious grain boundaries are labeled. The concentration of Zr reaches zero at several points, a sign that some local regions are depleted of Zr, but grain interiors are still doped. A similar behavior is observed when increasing

the annealing temperature to 750 °C, with one noticeable difference being the higher amplitude of Zr peaks to maximas of ~7-8 at.% (Fig. 5.4(b)). In addition, some large areas are fully depleted of Zr, providing evidence of full segregation at the grain boundaries. Previous works on characterization of solute distribution in nanocrystalline W-Ti [79] and Ni-W [201] only showed partial segregation of solutes in those systems, with crystal interiors that were still heavily doped. Here, full segregation of Zr atoms to the grain boundaries of nanocrystalline Cu is observed for annealing temperatures at and above 750 °C.

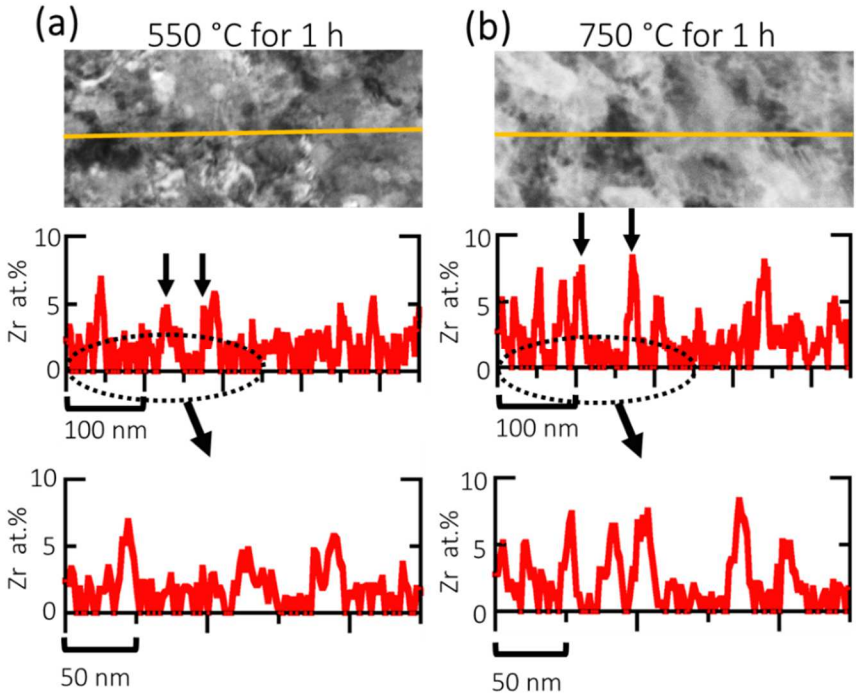

Figure 5.14 Scanning TEM images and EDS line profile scans of the samples annealed for 1 h at (a) 550 °C and (b) 750 °C. A section of each profile from 0-250 nm was magnified and is shown directly below each Fig. The locations of selected grain boundaries are marked with arrows.

Fig. 5.5 shows scanning TEM images and EDS line profile scans of the samples annealed for 1 h at 850 °C and 950 °C. The concentration of segregated Zr at the grain boundaries slightly increased to ~10 at.% in most cases and the spacing between the Zr peaks is also wider, showing the effect of grain growth. The spacing between the maximums in the profile is closely related to

the grain size of the samples. A high concentration of Zr was observed at some grain boundaries, exceeding 20 at.% Zr in rare cases such as the example denoted by an arrow in Fig. 5.5(a). These observations were not common but did occur occasionally, showing that some grain boundaries may have been more heavily doped than average. Again, grain interiors appear to be depleted of Zr.

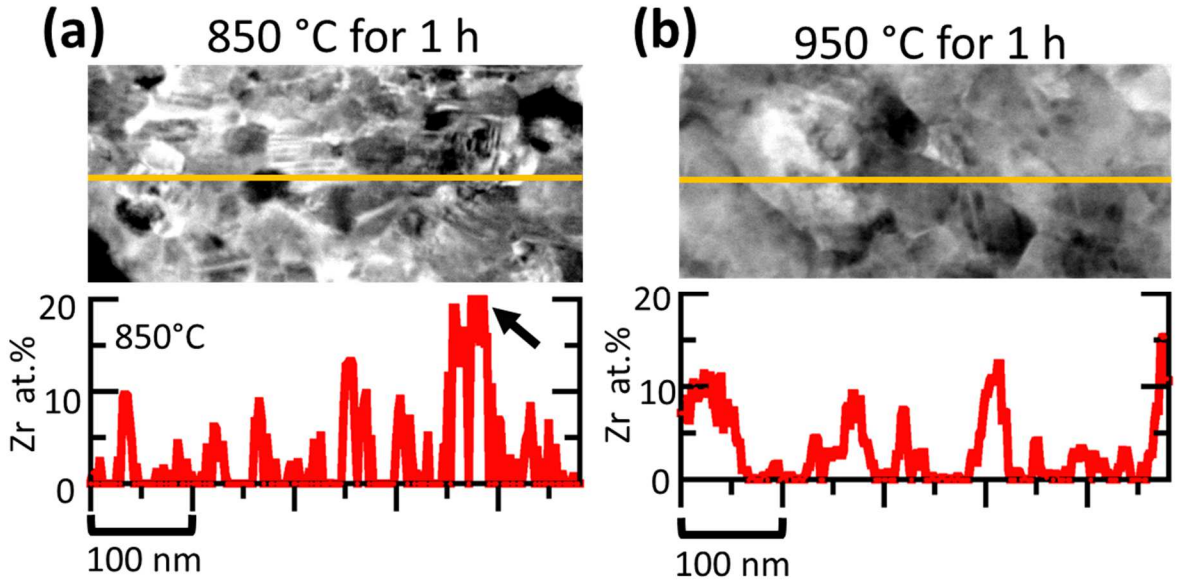

Figure 5.15 Scanning TEM images and EDS line profile scans of the samples annealed for 1 h at (a) 850 °C and (b) 950 °C. An example of unusually high concentration of Zr in part (a) is marked with an arrow.

5.3.2 Grain boundary structure

As discussed in the introduction, a combination of high segregation levels and high temperature can lead to changes in grain boundary structure, namely transitions between different complexion types. Fig. 5.6 shows high resolution TEM images of representative interfacial structures for the samples annealed at 550 °C and 750 °C for 1 h. In both cases, the grain boundaries are atomically sharp, with no obvious phase-like structure at the interface, and show a low-energy configuration which is an ordered and continuous grain boundary structure that may

contain a periodic dislocation array. The structure of the triple junction in Fig. 5.6(b) is another example of ordered interfacial regions in these samples.

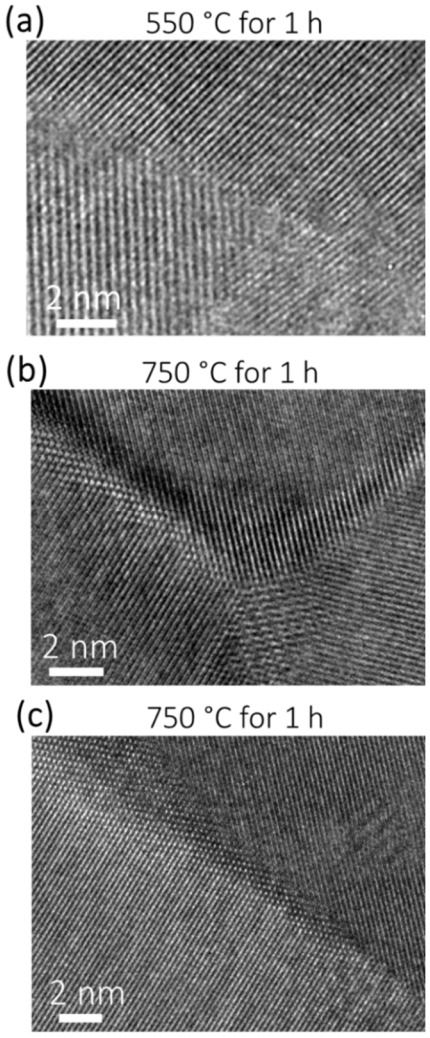

Figure 5.16 High resolution TEM image of interfaces in Cu-3 at.% Zr. (a) A low energy configuration at the grain boundary in the sample annealed for 1 h at 550 °C. (b) A Fourier filtered high resolution TEM image of a fully connected triple junction. (c) A fully connected grain boundary in the sample annealed for 1 h at 750 °C.

Increasing the annealing temperature to 850 °C and 950 °C, distinct grain boundary structures begin to emerge. Fig. 5.7(a) shows a 2.6 nm thick AIF between two grains in the sample annealed at 850 °C. Fig. 5.7(b) shows the existence of another AIF with sub-nanometer thickness (0.8 nm)

within the same sample. The thickness of these films is constant across a given grain boundary, suggesting that they are in equilibrium with the abutting grains.

Fig. 5.7(c) shows a high resolution TEM image of a grain boundary in the sample annealed at 950 °C. A relatively wide AIF with a thickness of 4.1 nm can be seen. Directly below this Figure are the Fast Fourier Transform (FFT) images of the grain boundary and the two abutting grains. The FFT of two grains show periodic spots around the center of the image, as expected from crystalline grains. On the other hand, the FFT of the grain boundary film shows no features, representative of a disordered amorphous layer. Fig. 5.7(d) shows another high resolution TEM of an AIF for the 950 °C sample with a thickness of 2.9 nm. Again, the interface of this film with the abutting grains is sharp and the thickness of this film does not change along the length of the grain boundary. Overall, AIFs in the 950 °C sample with thicknesses ranging from 0.5 nm to 5.7 nm were observed. It is also noteworthy that AIFs were observed more frequently in the sample annealed at 950 °C than the 850 °C sample. However, it is difficult to be quantitative about the fraction in each case because not all grain boundaries in a given area of a TEM sample can be adequately investigated with high resolution TEM, due to limitations on finding edge-on grain boundaries.

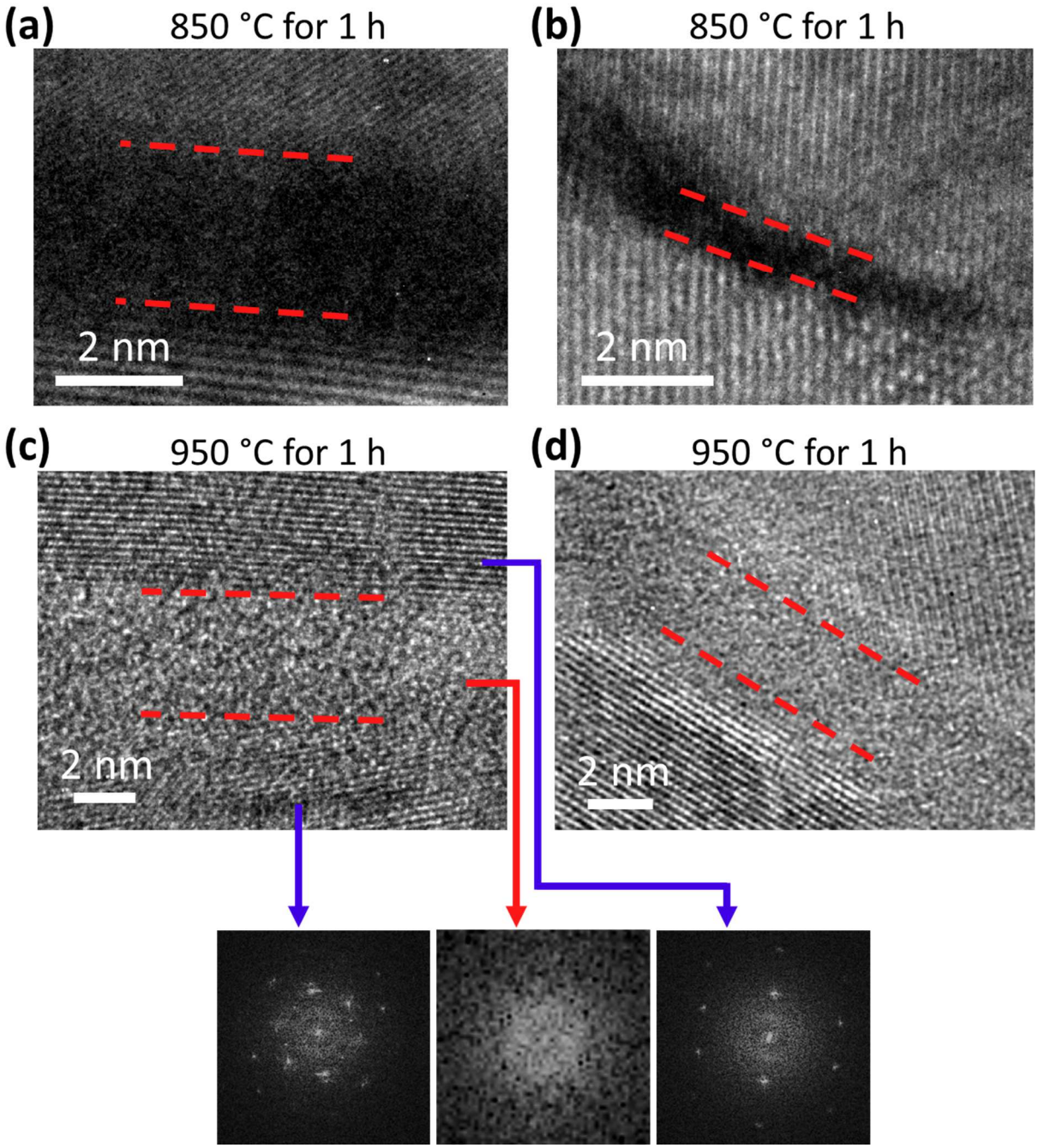

Figure 5.17 High resolution TEM images of AIFs in samples annealed at 850 °C and 950 °C with thicknesses of (a) 2.6 nm, (b) 0.8 nm, (c) 4.1 nm, and (d) 2.9 nm.

5.3.3 Second phase precipitation

Precipitation of ZrC particles was detected after annealing the samples, as was shown in the insets of Fig. 2. Initially, a small volume fraction of ZrH_2 particles is detected from the XRD pattern in the as-milled sample (Fig. 5.8(a)). It is likely that the ZrH_2 precipitates were formed during milling due to reaction of excess Zr with H atoms, likely coming from the stearic acid used as the process control agent. Although stearic acid has a great deal of both H and C, ZrH_2 has a lower enthalpy of formation compared to ZrC and the mobility of H is higher than C in Zr. Annealing at higher temperatures led to formation of ZrC particles, as shown in the XRD pattern (Fig. 5.8(a)) and the SAED pattern (Fig. 5.8(b)) of the sample annealed for 950 °C. This likely occurs because annealing breaks carbon-carbon bonds in stearic acid and freed C atoms, which then react with ZrH_2 at high temperatures to form ZrC [202]. The absence of ZrH_2 and the presence of ZrC was observed for all annealed samples.

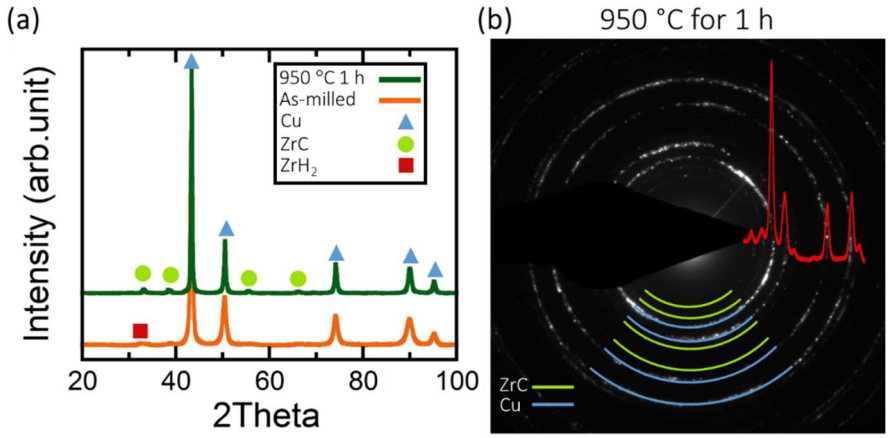

Figure 5.18 (a) XRD pattern of the as-milled and 950 °C sample annealed for 1 h. The positions of Cu, ZrC, and ZrH_2 peaks are marked. (b) TEM SAED pattern of the sample annealed for 1 h at 950 °C with ZrC and Cu rings identified. An average intensity profile is also overlaid on the SAED pattern, using the PASAD script.[203]

Fig. 5.9(a)-(c) shows dark field images of the samples annealed for 1 h at three different temperatures. ZrC particles are homogenously dispersed throughout the microstructure and were

found both in the grain interiors as well as on the grain boundaries. Comparison of Fig. 5.9(a) and (c) demonstrates that ZrC particles grew larger in size after annealing at higher temperatures. Fig. 5.9(d) and e show a zoomed dark field TEM image and a high resolution TEM image, respectively, of a ZrC particle in the 750 °C sample. The high resolution TEM image shows that this ZrC particle is sitting along a grain boundary. To further analyze the ZrC particles, XRD particle size of ZrC is plotted as a function of annealing time in a semi-log plot in Fig. 5.10. The trend in ZrC particle growth is similar to that observed for grain size. Annealing at 850 °C and below for a period of 1 week results in small particles with average particle sizes of ~10 nm or less. By increasing the annealing temperature to 950 °C, ZrC particle size increases, to a maximum of ~25 nm after 1 week. The observed particle growth can be due to diffusion of Zr atoms along the grain boundaries to reach ZrC particles or by coalescence of smaller particles as the grain boundaries migrate.

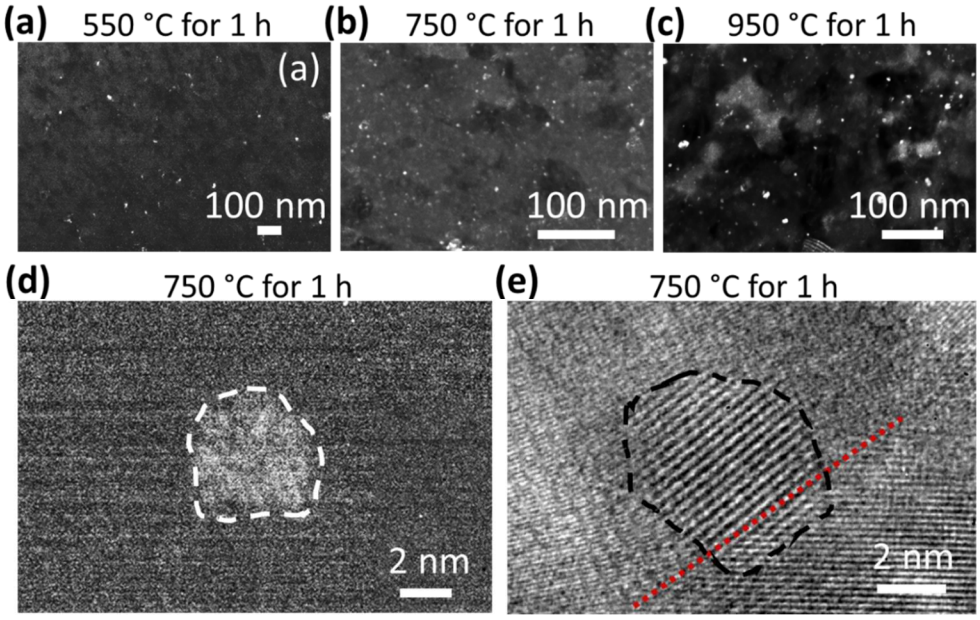

Figure 5.19 Dark field TEM images of ZrC precipitates in the Cu-3 at.% Zr microstructure (a) annealed at 550 °C for 1 h, (b) annealed at 750 °C for 1 h, and (c) annealed at 950 °C for 1 h. (d) A higher resolution dark field TEM image of a ZrC particle. (e) The corresponding high resolution TEM image. The particle is sitting on the grain boundary, which is marked with a red dotted line.

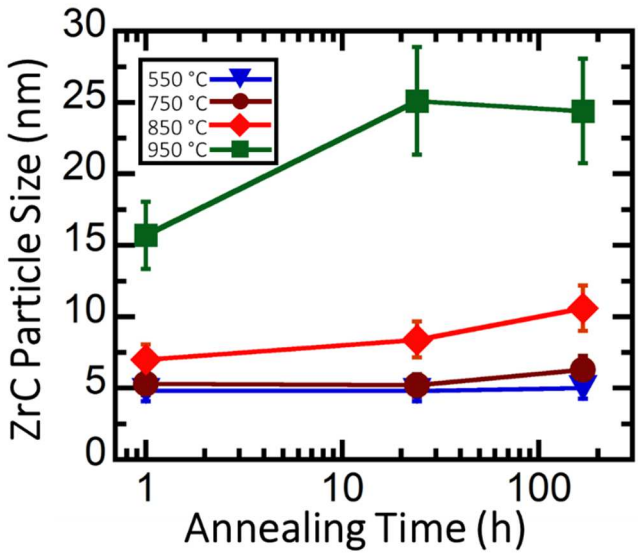

Figure 5.20 ZrC particle size as a function of annealing time. The as-milled sample is not included in the graph since it does not contain ZrC particles.

5.4 Discussion

5.4.1 Grain size stability

The results of the XRD and TEM analysis show significant grain size stabilization in this alloy, even after annealing under extreme conditions. This level of thermal stability is especially notable, because it surpasses the temperatures and times necessary to obtain fully dense nanocrystalline Cu through sintering processes. Sintering of nanocrystalline Cu is often performed in the temperature range of 400-800 °C for a period of 1-24 h, depending on the type of sintering technique [204,205]. Additionally, our results agree with the recent study by Atwater et al. [185], who showed that a nanocrystalline grain size can be retained after annealing at temperatures as high as 800 °C for cryogenically ball milled Cu-Zr without the addition of process agents. These authors attributed their results to the segregation of Zr atoms to the grain boundaries at low temperatures, while also showing that second phase intermetallic particles begin to from at temperatures higher above 800 °C to help stabilize the grain boundaries through Zener pinning.

Since both grain boundary segregation and second phase precipitates are present in our study as well, stability combination of thermodynamic and kinetic stabilization may be responsible for the observed retardation of grain growth.

Based on the study by Darling et al. [91], a true thermodynamic equilibrium for nanocrystalline Cu-Zr with an average grain size of 25 nm at 650 °C is possible but requires a global concentration of 6 at.% Zr, higher than that used here. However, according to the molecular dynamic simulations and thermodynamic studies of Millet et al. [206], if the ratio of atomic radius of a solute to atomic radius of Cu is equal to 1.25, a global dopant concentration of 0.5 at.% is enough to reduce the excess grain boundary energy to zero in a nanocrystalline Cu alloy with a grain size of 20 nm. By considering the atomic radii of Zr (159.7 pm) and Cu (127.6 pm) [207], the ratio of atomic radius of Zr to Cu is 1.25, meaning that a dilute concentration of Zr should be able to stabilize the grain size of nanocrystalline Cu-Zr. Our results showed a significant degree of solute segregation to grain boundaries, so we expect that thermodynamic concerns play a major role in stabilizing our nanocrystalline Cu-3 at.% Zr alloy, in agreement with the prediction of these studies. However, such models tend to ignore kinetic effects, such as those associated with desegregation of solutes from the grain boundary and formation of second phase particles.

While we do not observe desegregation, second phase particles do exist and could have an effect on the thermal stability of Cu-3 at.% Zr as well. The effect of ZrC and ZrO_2 particle pinning on the thermal stability of a ball milled nanocrystalline Cu was studied by Morris and Morris [208]. After adding 10.8 vol.% of second phase particles in that study, annealing treatments of 900 °C for 1 h resulted in a grain size of 73 nm. In another study, the effect of Ta particles on thermal stability of nanocrystalline Cu-10 at.% Ta was confirmed and an average grain size of 111 nm was reported after annealing the microstructure for 4 h at 900 °C [209]. Therefore, it is clear that

addition of second phase particles can hinder grain growth through Zener grain boundary pinning mechanisms. Our peak intensity ratio date from XRD shows that our nanocrystalline Cu-3 at.% Zr alloy could contain 2-4 vol.% of ZrC particles, depending on the annealing temperature and time. An average grain size due to grain boundary pinning by second phase particles can be estimated by a simple Zener equation [210]:

$$D_{Zener} = K_{Zener} \frac{d_p}{f^m} \tag{5.1}$$

where d_p and f are secondary phase particle size and volume fraction respectively, and K_{Zener} and m are constants which can be taken as 0.17 and 1 if the volume fraction of second phase particles is less than 0.05 [210]. By taking $f = 0.02$ and $d_p = 5$ nm for the sample annealed at 550 °C for 1 h, Eq. 5.1 gives $D_{Zener} = 42.5$ nm, which is approximately twice as large as the measured grain size of this sample. This calculation suggests that particle pinning cannot fully account for the observed thermal stability in nanocrystalline Cu- 3 at.% Zr. Consequently, both thermodynamic stabilization through grain boundary segregation and kinetic stabilization through Zener pinning seem to be operating here.

5.4.2 Complexion formation in nanocrystalline Cu-Zr

Our TEM results showed distinct grain boundary structures in nanocrystalline Cu-3 at.% Zr after annealing at different temperatures. As previously shown by Dillon et al [105], each grain boundary state has a unique property set that can cause a dramatic change in the overall material properties, motivating further discussion. At the lowest annealing temperature of 550 °C, ordered grain boundary structures are observed and EDS results show that all of the grain boundaries are doped with Zr. Therefore, the observed grain boundary structures at this temperature are Type I complexions. Type I complexions are more energetically favorable at lower temperatures and

lower dopant compositions, having a high degree of crystalline order at the interface compared to other complexion types [211]. Furthermore, Type I complexions have been shown to lower grain the boundary mobility in MgO-doped Al_2O_3 and cause embrittlement in Bi doped Cu.[105,212] It is important to note that these grain boundary structures represent the thermodynamically stable configurations that form at that annealing temperature, since fast quenching was employed. However, the conventional equilibrium phase diagram (Fig. 5.11) [213] for binary Cu-Zr alloy has no information about complexions and only a mixture of Cu and Cu_9Zr_2 should be thermodynamically-stable at this temperature, although such a mixture is not seen here.

Further increasing the annealing temperature to 750 °C caused an increase in the degree of grain boundary segregation compared to 550 °C, but again Type I complexions were the only grain boundary structures that were identified. The study by Dillon et al. [105] on complexion formation in Al_2O_3 show that type V and VI complexions can start to form at temperatures at and above ~0.71 of melting point of Al_2O_3, which would translate to 615 °C for Cu-3 at. % Zr. The lack of AIFs at 750 °C may suggest that the formation of quasi-liquid films require higher temperatures in metallic alloys. However, our high resolution TEM data cannot completely rule out the possibility of Type III or IV complexions, which have been observed in some other studies [214,215]. In general, complexions types of bilayer and multilayer adsorptions are extremely difficult to observe and to differentiate from one another even in an aberration-corrected scanning TEM. This difficulty arises because accurate imaging of these thin complexions requires a perfect edge-on imaging condition and even a small amount of misalignment can lead to overlapping of lattice fringes from the neighboring grains, effectively covering the thin complexions from view [216].

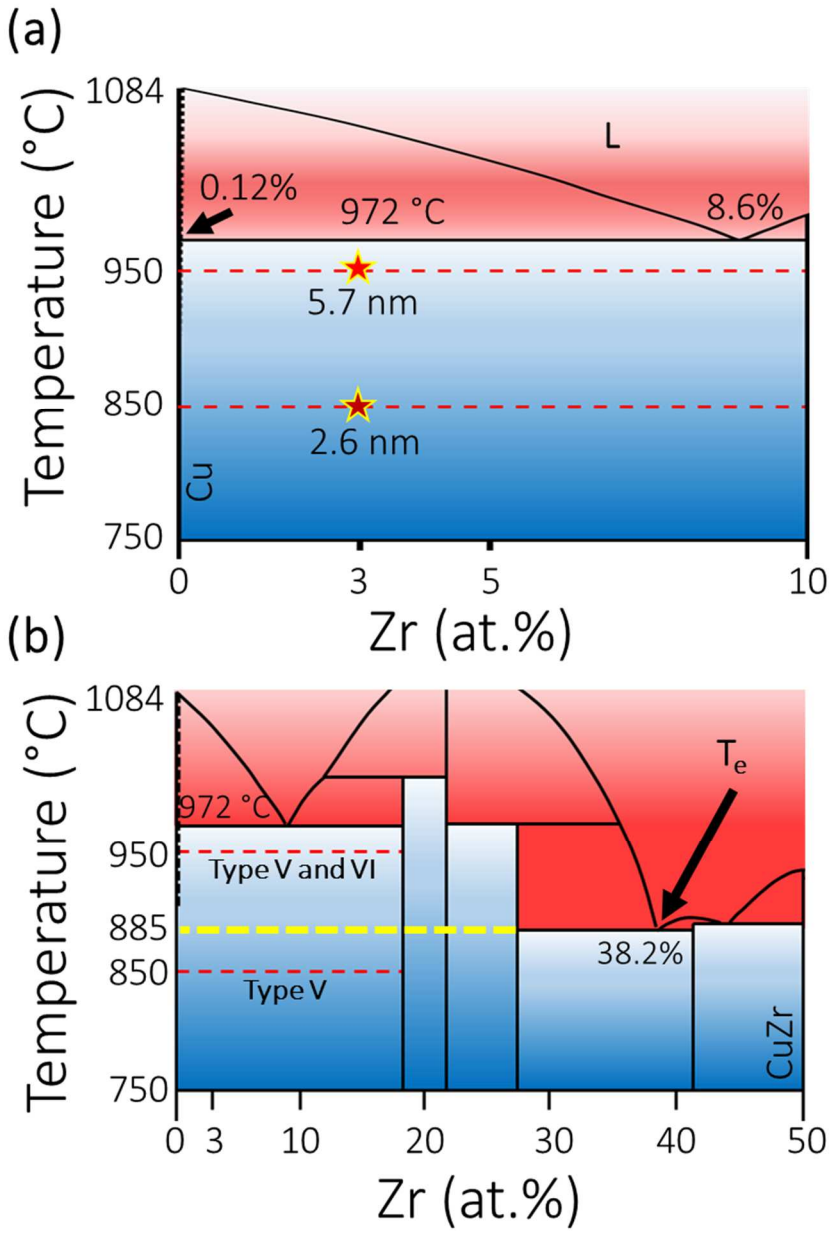

Figure 5.21 (a) A section of Cu-Zr phase diagram, based on Ref [213]. , showing the region of interest in this study. The dotted lines show the annealing temperatures where AIFs were found, with the maximum film thickness labeled. (b) A larger section of the grain boundary phase diagram showing the lowest eutectic temperature and composition. The 850 °C sample is below all the solidus temperatures possible in this phase diagram, so any amorphous films must be complexion Type V. Blue shows region of all solid phase and red color shows the sections of all liquid or two phase solid-plus-liquid regions.

Nanometer thick quasi-liquid intergranular films were observed at 850 °C. These grain boundaries resemble the intergranular grain boundary films which are formed in coarse-grained

polycrystalline ceramics and metals,[217] but have not been found in nanocrystalline metals previously. It should be noted that the annealing temperature here is below the eutectic temperature (Fig. 5.11(b)), and therefore this complexion cannot be a meta-stable bulk liquid phase. Additionally, the thickness of amorphous grain boundaries films was constant along a given interface, confirming the equilibrium state of the amorphous film with the neighboring grains. All of the mentioned conditions match the criteria of a Type V complexion. The maximum thickness of the observed complexion Type V at 850 °C has been marked in Fig. 5.11(a). Recently, Luo and coworkers developed a framework to predict the equilibrium grain boundary film thicknesses at sub-solidus temperatures in binary alloys [218]:

$$\lambda \equiv -\Delta\gamma / \Delta G_{amorph} \tag{5.2}$$

where λ is a thermodynamic parameter proportional but not equal to film thickness, $\Delta\gamma$ is the difference between the excess energy of a clean grain boundary and the crystalline-amorphous interfaces, and ΔG_{amorph} is the volumetric free energy of formation of undercooled liquid. These authors showed that λ is related to temperature, mainly because the free-energy penalty for forming an undercooled liquid decreases with increasing temperature, so increasing annealing temperature should result in a thickening of any amorphous grain boundary films. As a result, annealing at 950 °C leads to the formation of thicker amorphous complexions. The maximum thickness of any amorphous complexion observed at this temperature, 5.7 nm, is marked in the Fig. 5.11(a). It is important to note that we also observed ordered grain boundaries, or complexion Type I, in both the 850 °C and 950 °C samples, so not all boundaries are covered with AIFs and a distribution of complexions types is observed. This distribution is likely related to the fact that grain boundary free energy depends not only on temperature and chemical potential, but also on the starting grain

boundary structure. Interfaces have five degrees of freedom, related to grain misorientation and grain boundary normal, which can also influence the energy and thermodynamics of the interfaces.

While the amorphous films in the sample annealed at 850 °C can only be Type V complexions, it is possible that the AIFs observed in the 950 °C sample are a combination of Type V and Type VI. Although the annealing temperature is below the solidus temperature for the global composition used here, it is above the eutectic temperature, or the lowest temperature for the binary alloy where any liquid phase is in equilibrium (Fig. 5.11(b)), and it is important to recall that some grain boundaries showed levels of Zr segregation to >20 at.%. If the local composition at the grain boundary exceeds 37.5 at.% Zr, it is possible that a wetting film can nucleate at 950 °C. Although it is difficult to definitively classify the amorphous films in this sample, the two competing complexion types has different characteristics. Complexion Type V is in equilibrium, so a uniform thickness should be maintained along the entirety of a given grain boundary. On the other hand, complexion Type VI is a bulk phase, so it can change thickness along the length of an interface based on the available concentration of dopant atoms. All of the amorphous films observed in the 950 °C sample showed no measureable change in thickness here, and the wetting films that have been observed in other materials are often much thicker, often being at least 10 nm thick. It is also worth highlighting that grain boundaries with Zr content above ~10 at.% were rarely observed, meaning it is likely that most if not all of the observed amorphous films were Type V.

Lastly, our grain growth results can be revisited to understand the effect of grain boundary complexion structure on grain size stabilization. To obtain a clear picture, only the highest and lowest annealing temperatures are compared. At 550 °C, grain growth is slow and the error bars on average grain size still overlap between annealed and as-milled after 1 week. Only complexion

Type I was found in this sample, and previous studies in Al_2O_3 showed that this type of complexion has the lowest mobility of all types [105]. In contrast, type V and VI complexion have been shown to dramatically speed up diffusion and cause abnormal grain growth or activated sintering [105,219]. Observation of both a higher grain growth and formation of Type V or VI complexions in the sample annealed at 950 °C shows a correlation between the thermal stability and complexion type. Since grain boundaries can act as short-circuit paths for diffusion, it is also worth noting that the interfaces are thicker when the higher level complexions are formed at 950 °C.

5.4.3 Effect of structural features on hardness

Thermal stability is essential in nanocrystalline metals because it retains the properties that motivated research in nanocrystalline metals in the first place. However, the impact of segregation, complexions, and precipitates on mechanical properties should be considered as well. Nanoindentation hardness data for each sample is plotted as a function of annealing time in Fig. 5.12(a). For comparison, the hardness value of a pure Cu sample with an average grain size of 22 nm, made with the same processing conditions, is also included in the same plot as a blue line with error bars denoted by light blue shading. From the Figure, it is clear that the Cu-Zr alloys exhibit hardness values that are always higher than the as-milled pure Cu, even after annealing at extremely high temperatures for very long times. A maximum hardness, ~4.4 GPa, is reached in the samples annealed at 550 °C for 24 h and 750 °C for 1 h. Since annealed samples have larger grain sizes compared to the pure nanocrystalline Cu sample, the strength of the alloy should have decreased if grain size was the only consideration, following the Hall-Petch relationship:

$$\sigma_{Hall-Petch} = \sigma_o + \frac{k}{\sqrt{d}} \tag{5.3}$$

where σ_o is a frictional stress and k is a constant, taken as 25.5 MPa and 0.11 MN/m$^{3/2}$, respectively, for Cu [220]. However, the opposite is observed, with the larger grain size annealed samples show higher strength. Therefore, other hardening mechanisms must be at work in this alloy, with grain boundary segregation and precipitation hardening being prime candidates [131].

Some studies suggest that Orowan hardening, or the bowing of dislocations between second phase particles, is mainly responsible for the observed increase in hardness of the nanocrystalline metals that contain precipitates [220]. The increased in yield stress due to an Orowan hardening mechanism can be estimated by [221]:

$$\Delta\sigma_{Orowan} = \frac{0.13Gb}{\lambda} ln\left(\frac{d_p}{2b}\right) \tag{5.4}$$

where G and b are the shear modulus and Burgers vector, respectively, of Cu, d_p is the particle size, and λ is the interparticle spacing which is estimated by [221]:

$$\lambda \approx d_p \left[\left(\frac{1}{2f}\right)^{1/3} - 1\right] \tag{5.5}$$

where f is the volume fraction of precipitates. The combined effect of Orowan hardening and Hall-Petch hardening can then be calculated by assuming $H \sim 3\ \sigma_y$:

$$H_{total} = 3\ (\sigma_{Hall-Petch} + \Delta\sigma_{Orowan}) \tag{5.6}$$

Taking $G = 48$ GPa, $b = 0.255$ nm, and assuming a constant volume fraction of $f = 0.04$ for all the annealing conditions, which is the highest value found in any sample and serves to provide an upper bound on Orowan strengthening contributions, the Hall-Petch and Orowan hardness values were calculated and are plotted in a stacked bar chart in Fig. 5.12(b). The combined Hall-Petch and Orowan hardening effects almost fit some of the lower temperature annealing conditions. However, as the annealing temperature increases, the discrepancy between the simple grain size-precipitate model and our experimental results widens, suggesting that additional mechanisms begin to significantly contribute to the hardness. It is also important to remember that we have

used an upper bound for the volume fraction of secondary phase particles for these calculations and may in fact even be overestimating the Orowan contributions in some of the samples. Although the ZrC precipitates can significantly increase strength, their contribution fails to fully explain the increased hardness of these samples.

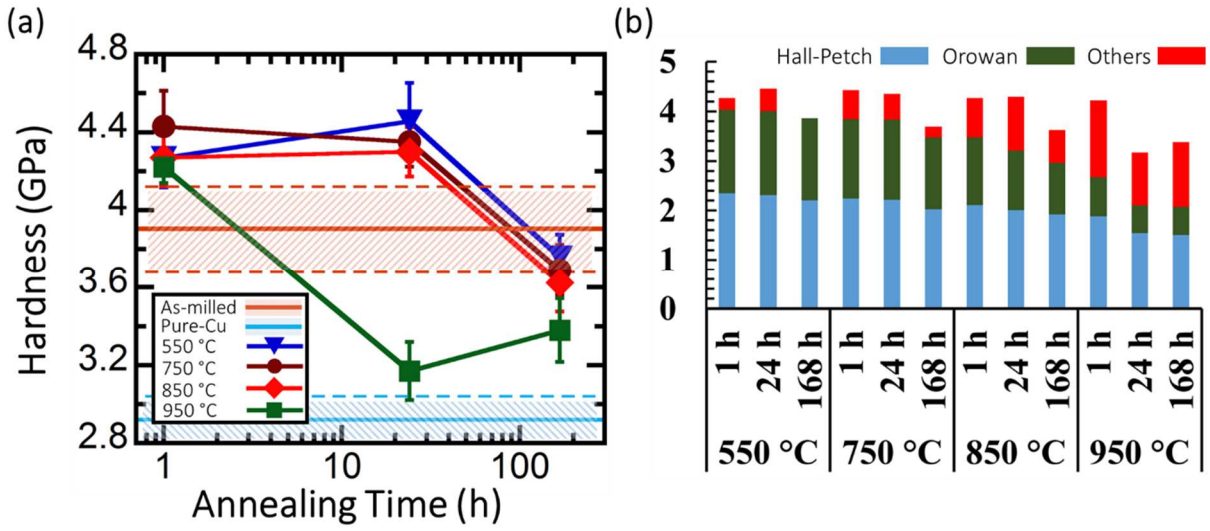

Figure 5.22 (a) Nanoindentation hardness as a function of annealing time for nanocrystalline Cu and Cu-Zr alloys. (b) Stacked bar chart of Hall-Petch, Orowan, and "other" hardening mechanisms for nanocrystalline Cu-3 at.% Zr at different annealing times and temperatures.

Grain boundary segregation has been shown to be another effective mechanism for increasing the strength of nanocrystalline metals. Vo et al. [129] studied doping of grain boundaries in nanocrystalline Cu with an average grain size of 8 nm through a combination of molecular dynamics and Monte Carlo simulations, in order to explore the effect of grain boundary segregation on grain boundary energy and yield strength. These authors observed a 60% increase in the yield stress after doping the material with only 1.2 at.% Nb, while also observing that the grain boundary energy is lowered with doping in a manner that is proportional to all observed strengthening. A similar observation was reported in molecular dynamics simulations of nanocrystalline Cu doped with Sb [18]. The nanoindentation hardness measurements of Ozerinc

et al. [130] on nanocrystalline Cu-based alloys with an average grain size of 17 nm showed that doping grain boundaries with 10 at.% Nb and Fe can add an extra ~3 GPa and ~1 GPa to the hardness, respectively. These observations confirmed the previous molecular dynamic simulation findings that grain boundary segregation can significantly increase strength, showing a direct relationship between a decrease in excess grain boundary energy and an increase in strength. Such a relationship was also observed in nanoindentation studies by Rupert et al. [35], who showed that accessing a lower grain boundary energy configuration with grain boundary relaxation can lead to higher hardness values in nanocrystalline Ni-W.

Consequently, the structure and excess energy of grain boundaries can be very important for determining the strength of nanocrystalline metals. Since the grain boundaries are the main source of dislocations in nanocrystalline metals, any process that facilitates or hinders grain boundary dislocation emission can decrease or increase the strength of the material. Although we dope our boundaries in traditional ways at lower temperatures, the formation of higher type grain boundary complexions should also affect interfacial energy and, therefore, strength. It is important to recall that complexions form at high temperatures because they are energetically favorable over a clean boundary, meaning they will reduce the excess energy of the system. In addition, there may be complex interactions of dislocations at the two newly created interfaces between the AIF and the grains. Brandl et al. [222] studied this situation with molecular dynamic simulations and found that these types of interfaces can attract dislocations during deformation, perhaps acting as sinks. In our study, we find that the "other" contribution to hardness, which is associated with segregation and boundary structure, becomes larger at higher annealing temperatures. Since we observe thicker AIFs as temperature increases, it appears that complexions structure is also important for mechanical strength.

5.5 Conclusion

In this article, the evolution of grain size, grain boundary structure, and hardness of nanocrystalline Cu-3 at.% Zr during thermal annealing was studied. The following conclusions can be made:

- Significant thermal stability was observed, due to a combination of segregation of Zr atoms to grain boundary sites, complexion formation, and the formation of ZrC precipitates. Even annealing the alloy at the extreme condition of 98% of solidus temperature for a period of 1 week only caused coarsening an average grain size of 54 nm.
- A number of complexions states were observed, with higher temperatures promoting increases disorder and thicker grain boundaries. Lower temperatures gave rise only to Type I complexions, or doped yet ordered interfaces. AIFs appeared above 850 °C, with higher temperatures promoting thicker films. While it is clear that the majority of these amorphous films were Type V and in equilibrium with the abutting grains, it is possible that a few were Type VI wetting films. Overall, amorphous complexions with thicknesses ranging from 0.5 to 5.7 nm were observed.
- The hardness of all of the samples remained higher than that of pure nanocrystalline Cu, with a maximum hardness value of 4.4 GPa measured. The combination of Hall-Petch and Orowan strengthening cannot fully explain the observed hardness, meaning that grain boundary segregation and complexion formation also lead to strengthening in this alloy. The influence of grain boundary state on strength becomes more significant at higher temperatures.

An important conclusion of this study is the formation of obvious complexions in a metallic alloy that retains its nanocrystalline grain size. Thick AIFs were found at higher temperatures, giving a unique microstructure without the loss of strength associated with nanocrystalline metals. It was shown that by changing the annealing condition, different types of grain boundary complexions can be formed, providing a new set of tools for engineering the interfaces of nanocrystalline metals.

Chapter 6 : Conclusions

Nanocrystalline metals are the next generation of advanced materials due to their exceptional physical and mechanical properties. Recent advancements in this field show that these metals have the potential to be produced in bulk quantities in the near future. The main challenge in this field is on how to manipulate the grain boundary structure to get the desired properties. The goal of this thesis is to get a better understanding of intercrystalline interfaces and to provide solutions for the ongoing problem of grain growth and plastic instability in this field. The following are the main conclusion of the studies done in this thesis.

In Chapter 2, microcompression experiments were done on electrodeposited nanocrystalline Ni-W with grain sizes from 5 to 90 nm. It was shown that microcompression can be used to successfully probe the mechanical properties of nanocrystalline metals while avoiding common processing issues in large scale mechanical testing in these materials. Shear localization was observed as the grain size decreases and it was most pronounced in the 5 nm grain size sample. Relaxation of the grain boundaries enhanced the shear localization effect and this effect was more pronounced for the smallest grain size. Overall it was shown that the more ordered grain boundary structure could be detrimental in the deformation behavior of nanocrystalline metals.

To understand the effect of shear localization that was observed in the previous chapter, the structure of shear bands in a nanocrystalline Ni-W with 5 nm grain size was studied in Chapter 3. It was observed that grain coarsening occurs inside the shear band although the material has been shown to be thermally stable against grain growth. Additionally, the grain size outside the shear bands were remained unchanged showing that the grain growth were mainly due to high values of localized strain.

To address the issue of shear banding and plastic instability in nanocrystalline metals, grain boundary complexions were introduced in a nanocrystalline Cu-Zr as damage tolerant interfaces in Chapter 4. Our microcompression and microbeam bending experiments provided proof that grain boundary complexions can dramatically improve the mechanical properties of nanocrystalline Cu-Zr. The TEM results showed these grain boundary complexions in the form of AIF that form at high temperatures and are in thermodynamic equilibrium with abutting grains. Without sacrificing the strength of the nanocrystalline Cu-Zr, toughness and ductility was improved significantly. Our result provided a new route to design against failure in nanocrystalline metals in general.

In Chapter 5, we systematically explored the effect of temperature and time on the formation of grain boundary complexions and grain growth. It was observed that grain boundary complexions can form in nanocrystalline Cu-Zr that has a stable microstructure even after annealing for a period of one week and 98% of the eutectic temperature. Nanoindentation measurements showed that even with these extreme annealing condition the grain size and the hardness of these alloys remains higher than a pure nanocrystalline Cu.

In conclusion, the results of this thesis show the importance of grain boundary structure on many aspects of nanocrystalline metals physics and mechanics. We show that the ordered grain boundary structures can induce strain localization while introduction of disordered grain boundary structures can dramatically toughen nanocrystalline metals. We are hopeful that the studies done in this thesis could be used in the design of failure resistant and thermally stable nanocrystalline metals.

Chapter 7 : Future work

While the research in this thesis shed light on the importance of grain boundary structure in nanocrystalline metals, many more unknown question remains to be answered in future studies. Below is a list of suggested future work that could answer some of these questions:

- Chapter 2: While grain boundary relaxation was observed to have an important effect on the mechanical propertied of nanocrystalline Ni-W, the exact nature of grain boundary structure and chemistry remains unknown. High resolution TEM and atom probe tomography should be used to explore the interfaces in this alloy.
- Chapter 3: It was observed that the thickness of the shear bands during microcompression and nanoindentation might be dependent on local strain rates. Molecular dynamic simulation or controlled in-situ TEM nanoindentation studies must be done to study the possible relationship between these two.
- Chapter 4: The grain boundary complexions that were introduced in nanocrystalline Cu should be studied in other materials systems such as Ni, Al etc. Molecular dynamic simulation of 3D nanocrystalline structure with grain boundary complexions can be used to better understand the dislocation-complexion interaction.
- Chapter 5: The thermodynamics of how complexions form in nanocrystalline metals is an open question. Theoretical modeling like the work of Prof. Luo's group [218] can help with better understanding of these interfaces. Additional, special attention should be given to nanocrystalline metals when considering those models since grain boundaries in nanocrystalline metals tend to have a different configuration compared to conventional metals.

References

[1] Kumar KS, Van Swygenhoven H, Suresh S. Acta Mater 2003;51:5743.
[2] Dao M, Lu L, Asaro RJ, et al. Acta Mater 2007;55:4041.
[3] Meyers MA, Mishra A, Benson DJ. Prog. Mater Sci. 2006;51:427.
[4] Padilla HA, Boyce BL. Exp Mech 2010;50:5.
[5] Tang F, Gianola DS, Moody MP, et al. Acta Mater 2012;60:1038.
[6] Gurrappa I, Binder L. Sci. Technol. Adv. Mater. 2008;9.
[7] Rupert TJ, Schuh CA. Acta Mater 2010;58:4137.
[8] Rupert TJ, Cai W, Schuh CA. Wear 2013;298–299:120.
[9] Hall EO. P Phys Soc Lond B 1951;64:747.
[10] Petch NJ. Journal of the Iron and Steel Institute 1953;174:25.
[11] Chokshi AH, Rosen A, Karch J, et al. Scripta Metall 1989;23:1679.
[12] Conrad H, Narayan J. Appl Phys Lett 2002;81:2241.
[13] Choi HJ, Lee SW, Park JS, et al. Mater Trans 2009;50:640.
[14] Trelewicz JR, Schuh CA. Acta Mater 2007;55:5948.
[15] Detor AJ, Schuh CA. Acta Mater 2007;55:371.
[16] Schiotz J, Jacobsen KW. Science 2003;301:1357.
[17] Vo NQ, Averback RS, Bellon P, et al. Phys Rev B 2008;78:4.
[18] Rajgarhia RK, Spearot DE, Saxena A. J Mater Res 2010;25:411.
[19] Yamakov V, Wolf D, Phillpot SR, et al. Phil Mag Lett 2003;83:385.
[20] Trelewicz JR, Schuh CA. Appl Phys Lett 2008;93:171916.
[21] Van Swygenhoven H, Derlet PM, Froseth AG. Nat Mater 2004;3:399.
[22] Van Swygenhoven H, Derlet PM, Froseth AG. Acta Mater 2006;54:1975.
[23] Huang M, Rivera-Diaz-del-Castillo PEJ, Bouaziz O, et al. Scripta Mater 2009;61:1113.
[24] Schiotz J, Di Tolla FD, Jacobsen KW. Nature 1998;391:561.
[25] Schiotz J, Vegge T, Di Tolla FD, et al. Phys Rev B 1999;60:11971.
[26] Van Swygenhoven H, Derlet PM. Phys Rev B 2001;64:224105.
[27] Shen XX, Xu Z, Lian JS, et al. Mat Sci Eng A 2011;528:7878.
[28] Cao AJ, Wei YG. Phys Rev B 2007;76.
[29] Farkas D, Van Swygenhoven H, Derlet PM. Phys Rev B 2002;66.
[30] Latapie A, Farkas D. Phys Rev B 2004;69.
[31] Jang D, Atzmon M. J Appl Phys 2006;99:7.
[32] Huang JY, Zhu YT, Jiang H, et al. Acta Mater 2001;49:1497.
[33] Loffler J, Weissmuller J. Phys Rev B 1995;52:7076.
[34] Detor AJ, Schuh CA. J Mater Res 2007;22:3233.
[35] Rupert TJ, Trelewicz JR, Schuh CA. J Mater Res 2012;27:1285.
[36] Giga A, Kimoto Y, Takigawa Y, et al. Scripta Mater 2006;55:143.
[37] Yang Y, Imasogie B, Fan GJ, et al. Metall and Mat Trans A 2008;39A:1145.
[38] Hanlon T, Tabachnikova ED, Suresh S. Int J Fatigue 2005;27:1147.
[39] Han BQ, Lavernia EJ. Adv Eng Mater 2005;7:457.
[40] Han BQ, Lee Z, Witkin D, et al. Metall and Mat Trans A 2005;36A:957.
[41] Wang YM, Ma E. Acta Mater 2004;52:1699.
[42] Rupert TJ, Gianola DS, Gan Y, et al. Science 2009;326:1686.
[43] Dao M, Lu L, Shen YF, et al. Acta Mater 2006;54:5421.
[44] Lu L, Chen X, Huang X, et al. Science 2009;323:607.

[45] Lund AC, Schuh CA. Acta Mater 2005;53:3193.
[46] Lund AC, Nieh TG, Schuh CA. Phys Rev B 2004;69:012101.
[47] Rupert TJ. Scripta Mater 2014;81:44.
[48] Harmon JS, Demetriou MD, Johnson WL, et al. Phys Rev Lett 2007;99:135502.
[49] Jiang WH, Pinkerton FE, Atzmon M. J Appl Phys 2003;93:9287.
[50] Matthews DTA, Ocelik V, Bronsveld PM, et al. Acta Mater 2008;56:1762.
[51] Hajlaoui K, Yavari AR, Doisneau B, et al. Scripta Mater 2006;54:1829.
[52] Wei Q, Jia D, Ramesh KT, et al. Appl Phys Lett 2002;81:1240.
[53] Wei Q, Zhang HT, Schuster BE, et al. Acta Mater 2006;54:4079.
[54] Ligda JP, Schuster BE, Wei Q. Scripta Mater 2012;67:253.
[55] Sansoz F, Dupont V. Appl Phys Lett 2006;89:111901.
[56] Rupert TJ. J Appl Phys 2013;114:033527.
[57] Shen TD, Schwarz RB, Feng S, et al. Acta Mater 2007;55:5007.
[58] Wu D, Zhang JY, Huang JC, et al. Scripta Mater 2013;68:118.
[59] Chen J, Lu L, Lu K. Scripta Mater 2006;54:1913.
[60] Sharon JA, Padilla HAI, Boyce BL. J Mater Res 2013;28:1539.
[61] Brooks I, Lin P, Palumbo G, et al. Mat Sci Eng A 2008;491:412.
[62] Weertman JR. Mat Sci Eng A 1993;166:161.
[63] Kula EB FN. Materias Research and Standards 1961;1:631.
[64] Brooks I, Palumbo G, Hibbard GD, et al. J Mater Sci 2011;46:7713.
[65] Zhao YH, Zhu YT, Lavernia EJ. Adv Eng Mater 2010;12:769.
[66] ASTM. E8/E8M − 11. Standard Test Methods for Tension Testing of Metallic Materials, 2011.
[67] Li HQ, Ebrahimi F. Acta Mater 2003;51:3905.
[68] Ma E. Scripta Mater 2003;49:663.
[69] Youssef K, Sakaliyska M, Bahmanpour H, et al. Acta Mater 2011;59:5758.
[70] Uchic MD, Dimiduk DA. Mat Sci Eng A 2005;400:268.
[71] Zhang JY, Lei S, Liu Y, et al. Acta Mater 2012;60:1610.
[72] Uchic MD, Dimiduk DM, Florando JN, et al. Science 2004;305:986.
[73] Uchic MD, Dimiduk DM, Wheeler R, et al. Scripta Mater 2006;54:759.
[74] Gertsman VY, Birringer R. Scripta Metall Mater 1994;30:577.
[75] Darling KA, VanLeeuwen BK, Koch CC, et al. Mat Sci Eng A 2010;527:3572.
[76] Andrievski RA. J Mater Sci 2014;49:1449.
[77] Pantleon K, Somers MAJ. Mat Sci Eng A 2010;528:65.
[78] Tschopp MA, Murdoch HA, Kecskes LJ, et al. JOM 2014;66:1000.
[79] Chookajorn T, Murdoch HA, Schuh CA. Science 2012;337:951.
[80] Suryanarayana C, Al-Aqeeli N. Prog. Mater Sci. 2013;58:383.
[81] Koch CC, Scattergood RO, Darling KA, et al. J Mater Sci 2008;43:7264.
[82] Zhou F, Lee J, Lavernia EJ. Scripta Mater 2001;44:2013.
[83] Weissmuller J. Nanostruct Mater 1993;3:261.
[84] Gianola DS, Van Petegem S, Legros M, et al. Acta Mater 2006;54:2253.
[85] Gianola DS, Mendis BG, Cheng XM, et al. Mat Sci Eng A 2008;483-84:637.
[86] Lohmiller J, Kobler A, Spolenak R, et al. Appl Phys Lett 2013;102:241916.
[87] Weissmuller J. J Mater Res 1994;9:4.
[88] Murdoch HA, Schuh CA. J Mater Res 2013;28:2154.

[89] Bakker H. Enthalpies in alloys : Miedema's semi-empirical model. Zurich: Trans Tech Publications, 1998.
[90] Zhu M, Wu ZF, Zeng MQ, et al. J Mater Sci 2008;43:3259.
[91] Darling KA, Tschopp MA, VanLeeuwen BK, et al. Comp Mater Sci 2014;84:255.
[92] Cantwell PR, Tang M, Dillon SJ, et al. Acta Mater 2014;62:1.
[93] Hart EW. Scripta Metall 1968;2:179.
[94] Clarke DR, Thomas G. J Am Ceram Soc 1977;60:491.
[95] Dillon SJ, Harmer MP, Luo J. JOM 2009;61:38.
[96] Lou LKV, Mitchell TE, Heuer AH. J Am Ceram Soc 1978;61:392.
[97] Kogtenkova OA, Protasova SG, Mazilkin AA, et al. J Mater Sci 2012;47:8367.
[98] Jud E, Zhang Z, Sigle W, et al. J Electroceram 2006;16:191.
[99] Bhattacharyya S, Subramaniam A, Koch CT, et al. Mat Sci Eng A 2006;422:92.
[100] Winkelman GB, Dwyer C, Hudson TS, et al. Appl Phys Lett 2005;87.
[101] Choi SY, Yoon DY, Kang SJL. Acta Mater 2004;52:3721.
[102] Ma SL, Asl KM, Tansarawiput C, et al. Scripta Mater 2012;66:203.
[103] Raabe D, Herbig M, Sandlobes S, et al. Curr Opin Solid St M 2014;18:253.
[104] Tang M, Carter WC, Cannon RM. J Mater Sci 2006;41:7691.
[105] Dillon SJ, Tang M, Carter WC, et al. Acta Mater 2007;55:6208.
[106] Shibata N, Pennycook SJ, Gosnell TR, et al. Nature 2004;428:730.
[107] Wirth R. Contrib Mineral Petr 1996;124:44.
[108] Gilbert CJ, Cao JJ, Moberlychan WJ, et al. Acta Mater 1996;44:3199.
[109] Avishai A, Scheu C, Kaplan WD. Acta Mater 2005;53:1559.
[110] Donzel L, Conforto E, Schaller R. Acta Mater 2000;48:777.
[111] Ning XG, Pan J, Hu KY, et al. Philos Mag A 1992;66:811.
[112] Divinski S, Lohmann M, Herzig C, et al. Phys Rev B 2005;71.
[113] Scholhammer J, Baretzky B, Gust W, et al. Interface Sci 2001;9:43.
[114] Molodov DA, Czubayko U, Gottstein G, et al. Phil Mag Lett 1995;72:361.
[115] Rabkin EI, Semenov VN, Shvindlerman LS, et al. Acta Metall Mater 1991;39:627.
[116] Shi XM, Luo J. Appl Phys Lett 2009;94:251908.
[117] Luo J, Gupta VK, Yoon DH, et al. Appl Phys Lett 2005;87.
[118] Luo J, Shi XM. Appl Phys Lett 2008;92.
[119] Shi XM, Luo J. Phys Rev B 2011;84.
[120] Bishop CM, Tang M, Cannon RM, et al. Mat Sci Eng A 2006;422:102.
[121] Tang M, Carter WC, Cannon RM. Phys Rev Lett 2006;97.
[122] Pan ZL, Rupert TJ. Comp Mater Sci 2014;93:206.
[123] Pan ZL, Rupert TJ. Acta Mater 2015;89:205.
[124] Wang YM, Li J, Hamza AV, et al. P Natl Acad Sci USA 2007;104:11155.
[125] Jang DC, Greer JR. Nat Mater 2010;9:215.
[126] Wang YM, Hamza AV, Barbee TW. Appl Phys Lett 2007;91.
[127] Detor AJ, Schuh CA. Acta Mater 2007;55:4221.
[128] Rupert TJ, Trelewicz JR, Schuh CA. J Mater Res 2012;27:1285.
[129] Vo NQ, Schafer J, Averback RS, et al. Scripta Mater 2011;65:660.
[130] Ozerinc S, Tai KP, Vo NQ, et al. Scripta Mater 2012;67:720.
[131] Rupert TJ, Trenkle JC, Schuh CA. Acta Mater 2011;59:1619.
[132] Montoya E, Bals S, Rossell MD, et al. Microsc Res Techniq 2007;70:1060.
[133] Zhang Z, Zhou F, Lavernia EJ. Metall and Mat Trans A 2003;34A:1349.

[134] Jang DC, Greer JR. Scripta Mater 2011;64:77.
[135] Kiener D, Motz C, Rester M, et al. Mat Sci Eng A 2007;459:262.
[136] Mayer J, Giannuzzi LA, Kamino T, et al. Mrs Bull 2007;32:400.
[137] Zhang H, Schuster BE, Wei Q, et al. Scripta Mater 2006;54:181.
[138] Han SM, Phillips MA, Nix WD. Acta Mater 2009;57:4473.
[139] Shade PA, Wheeler R, Choi YS, et al. Acta Mater 2009;57:4580.
[140] Schuster BE, Wei Q, Hufnagel TC, et al. Acta Mater 2008;56:5091.
[141] Brandstetter S, Van Swygenhoven H, Van Petegem S, et al. Adv Mater 2006;18:1545.
[142] Vo NQ, Averback RS, Bellon P, et al. Scripta Mater 2009;61:76.
[143] Jia D, Wang YM, Ramesh KT, et al. Appl Phys Lett 2001;79:611.
[144] Schwaiger R, Weber M, Moser B, et al. J Mater Res 2012;27:266.
[145] Kumar KS, Suresh S, Chisholm MF, et al. Acta Mater 2003;51:387.
[146] Schuster BE, Wei Q, Ervin MH, et al. Scripta Mater 2007;57:517.
[147] Hasnaoui A, Van Swygenhoven H, Derlet PM. Phys Rev B 2002;66:184112.
[148] Sansoz F, Dupont V. Materials Science & Engineering C 2007;27:1509.
[149] Jiang WH, Atzmon M. J Alloy Compd 2011;509:7395.
[150] Shi YF, Falk ML. Acta Mater 2007;55:4317.
[151] Ebrahimi F, Li HQ. J Mater Sci 2007;42:1444.
[152] Sanders PG, Eastman JA, Weertman JR. Acta Mater 1997;45:4019.
[153] Khalajhedayati A, Rupert TJ. Acta Mater 2014;65:326.
[154] Schuh CA, Nieh TG. Acta Mater 2003;51:87.
[155] Jiang WH, Atzmon M. J Mater Res 2003;18:755.
[156] Kuwano S, Fujita T, Pan D, et al. Mater Trans 2008;49:2091.
[157] Liu XC, Zhang HW, Lu K. Science 2013;342:337.
[158] Brandstetter S, Zhang K, Escuadro A, et al. Scripta Mater 2008;58:61.
[159] Wright WJ, Saha R, Nix WD. Mater Trans 2001;42:642.
[160] Schuh CA, Hufnagel TC, Ramamurty U. Acta Mater 2007;55:4067.
[161] Rice JR. The localization of plastic deformation. 14th International Congress on Theoretical and Applied Mechanics, vol. 1. Delft: North-Holland Publishing Company, 1976. p.207.
[162] Weissmuller J, Markmann J. Adv Eng Mater 2005;7:202.
[163] Panzarino JF, Ramos JJ, Rupert TJ. Modelling Simul Mater Sci Eng 2015;23:025005.
[164] Shan ZW, Stach EA, Wiezorek JMK, et al. Science 2004;305:654.
[165] Vo NQ, Averback RS, Bellon P, et al. Phys Rev B 2008;77:134108.
[166] Greer AL, Cheng YQ, Ma E. Mat Sci Eng R 2013;74:71.
[167] Jiang WH, Atzmon M. Acta Mater 2003;51:4095.
[168] Kim JJ, Choi Y, Suresh S, et al. Science 2002;295:654.
[169] Zheng BL, Zhou YZ, Mathaudhu SN, et al. Scripta Mater 2014;86:24.
[170] Ketov SV, Louzguine-Luzgin DV. Sci Rep 2013;3:2798.
[171] Lewandowski JJ, Greer AL. Nat Mater 2006;5:15.
[172] Han Z, Li Y. J Mater Res 2009;24:3620.
[173] Ivanisenko Y, Kurmanaeva L, Weissmueller J, et al. Acta Mater 2009;57:3391.
[174] Markmann J, Bunzel P, Rosner H, et al. Scripta Mater 2003;49:637.
[175] Fang TH, Li WL, Tao NR, et al. Science 2011;331:1587.
[176] Liao XZ, Kilmametov AR, Valiev RZ, et al. Appl Phys Lett 2006;88:021909.
[177] Skrotzki W, Eschke A, Joni B, et al. Acta Mater 2013;61:7271.

[178] Luo J. Journal of the American Ceramic Society 2012;95:2358.
[179] Wang D, Li Y, Sun BB, et al. Appl. Phys. Lett. 2004;84:4029.
[180] Jin Q, Wilkinson DS, Weatherly GC. Journal of the European Ceramic Society 1998;18:2281.
[181] MacLaren I. Ultramicroscopy 2004;99:103.
[182] Gu XW, Loynachan CN, Wu ZX, et al. Nano Lett 2012;12:6385.
[183] Kang D-H, Zhang H, Yoo H, et al. Sci. Rep. 2014;4.
[184] Smithells CJ, Gale WF, Totemeier TC. Smithells Metals Reference Book. Amsterdam; Boston: Elsevier Butterworth-Heinemann, 2004.
[185] Atwater MA, Scattergood RO, Koch CC. Mat Sci Eng A 2013;559:250.
[186] Dillon SJ, Harmer MP. Acta Mater. 2007;55:5247.
[187] Wang Y, Chen M, Zhou F, et al. Nature 2002;419:912.
[188] Bitzek E, Derlet PM, Anderson PM, et al. Acta Mater 2008;56:4846.
[189] Pan Z, Rupert TJ. Computational Materials Science 2014;93:206.
[190] Wang YM, Wang K, Pan D, et al. Scr. Mater. 2003;48:1581.
[191] Pan Z, Rupert TJ. Acta Mater. 2015;89:205.
[192] Brandl C, Germann TC, Misra A. Acta Mater. 2013;61:3600.
[193] Valiev RZ, Alexandrov IV, Zhu YT, et al. J. Mater. Res. 2002;17:5.
[194] Legros M, Elliott BR, Rittner MN, et al. Philosophical Magazine A 2000;80:1017.
[195] Hasnaoui A, Van Swygenhoven H, Derlet PM. Science 2003;300:1550.
[196] Lu K. Science 2014;345:1455.
[197] Wu XL, Jiang P, Chen L, et al. P Natl Acad Sci USA 2014;111:7197.
[198] Wang D, Li Y, Sun BB, et al. Appl Phys Lett 2004;84:4029.
[199] Li Y, Guo Q, Kalb JA, et al. Science 2008;322:1816.
[200] Krill CE, Birringer R. Philos Mag A 1998;77:621.
[201] Detor AJ, Miller MK, Schuh CA. Phil Mag Lett 2007;87:581.
[202] Xiang JY, Liu SC, Hu WT, et al. J Eur Ceram Soc 2011;31:1491.
[203] Gammer C, Mangler C, Rentenberger C, et al. Scripta Mater 2010;63:312.
[204] Khan AS, Farrokh B, Takacs L. J Mater Sci 2008;43:3305.
[205] Khan AS, Zhang HY, Takacs L. Int J Plasticity 2000;16:1459.
[206] Millett PC, Selvam RP, Saxena A. Acta Mater 2007;55:2329.
[207] Pauling L. J Am Chem Soc 1947;69:542.
[208] Morris DG, Morris MA. Acta Metall Mater 1991;39:1763.
[209] Frolov T, Darling KA, Kecskes LJ, et al. Acta Mater 2012;60:2158.
[210] Xu W, Li L, Saber M, et al. Metall and Mat Trans A 2015:1.
[211] Luo J. Appl Phys Lett 2009;95.
[212] Duscher G, Chisholm MF, Alber U, et al. Nat Mater 2004;3:621.
[213] Arias D, Abriata JP. Bulletin of Alloy Phase Diagrams 1990;11:452.
[214] Dillon SJ, Harmer MP. J Am Ceram Soc 2008;91:2304.
[215] Dillon SJ, Harmer MP. J Am Ceram Soc 2008;91:2314.
[216] Harmer MP. Science 2011;332:182.
[217] Luo J. Crit Rev Solid State 2007;32:67.
[218] Luo J. Curr Opin Solid St M 2008;12:81.
[219] Zhou NX, Luo J. Acta Mater 2015;91:202.
[220] Atwater MA, Bahmanpour H, Scattergood RO, et al. J Mater Sci 2013;48:220.
[221] Zhang Z, Chen DL. Scripta Mater 2006;54:1321.

[222] Brandl C, Germann TC, Misra A. Acta Mater 2013;61:3600.